

Figure 4.9: Feynman diagrams for four classes of B decay. Leptonic decays are rare in the Standard Model and have not yet been observed. The internal and external hadronic diagrams add constructively for two-body decay modes with branching ratios of order 2%. The semileptonic decay branching ratio for the neutral B is approximately 24%. Most B decays are considerably more complex, with many gluons connecting internal and external quarks.

The majority of B decays are purely hadronic decays in which leptons appear only due to B daughter decays. Writing amplitudes for these decays can be exceptionally difficult due to the subtleties of QCD. In EvtGen many of these are decayed with PHSP or JETSET models even when particles with nonzero spin are present in the initial or final states. Approximately 24% of neutral B and 8% of charged B decays are semileptonic $B \rightarrow D^{(*)}l\nu_l$ or $B \rightarrow D^{(*)}\pi l\nu_l$ where $D^{(*)}$ denotes a D or some excited state of a D . Semileptonic B decays can be treated in a straightforward

theoretical manner using form factors and decay constants obtained from experiment. The amplitudes can be explicitly written with form factors. Purely leptonic decays of the charged B are rare in the Standard Model since they are CKM suppressed relative to other decays by $|V_{ub}|^2 \approx 10^{-5}$. They are also helicity suppressed. They have yet to be observed. Leptonic decay amplitudes can be written explicitly using meson decay constants.

In semileptonic $B \rightarrow M l \nu_l$ decay, the b quark undergoes a transition $b \rightarrow W q$ (where $q = c, u$), the spectator quark propagates forward, and the W boson then couples to a $l \nu_l$ pair. The spectator quark then forms a meson M with the transition quark q . If the transition quark is $q = u$, the decay width is CKM suppressed relative to $q = c$ by $|V_{ub}/V_{bc}|^2 \approx 0.006$. Thus semileptonic B decays are dominated by $B \rightarrow D^{(*)} l \nu_l$. See Table 4.3 for a complete list of semileptonic B decays simulated in EvtGen.

Final state QCD interactions can greatly complicate the calculation of semileptonic B decay amplitudes. In Heavy Quark Effective Theory (HQET) [46] defined by the limit $m_q/\Lambda_{QCD} \gg 1$, the spectator quark and gluons binding the B are largely undisturbed as the b undergoes its transition. Since $m_b/m_c \approx 1$ in the heavy quark limit, the internal dynamics of the meson M are largely unchanged from those of the B . This picture is especially accurate at high q^2 ($q^\mu \equiv p_B^\mu - p_M^\mu$), when the virtual W is massive, since the recoil momentum of the M is low and gluon exchange is unnecessary for maintaining the spectator quark in the bound state with the transition

quark. Indeed, at low q^2 where the recoil is large and the W is light, the required gluon exchange suppresses the decays.

Approximating $P^{\mu\nu}(q) \approx ig^{\mu\nu}/m_W^2$, the amplitude for semileptonic decay $B \rightarrow Ml\nu_l$ ($M = bq$) is ([47])

$$\mathcal{M}_{B \rightarrow Ml\nu} = -i \frac{G_F}{\sqrt{2}} V_{qb} L^\mu H_\mu \quad (4.23)$$

$$L^\mu = \langle \nu_l | \gamma^\mu (1 - \gamma^5) | l \rangle \quad (4.24)$$

$$H_J^\mu = \langle M_J | \bar{q} \gamma^\mu (1 - \gamma^5) b | B \rangle \quad (4.25)$$

where J is the spin of M .

The hadronic current H_J^μ is written as an expansion in basis vectors with scale dependent coefficients (*form factors*) with q^2 dependence. Denoting by p^μ the B four momentum and by k^μ the M four momentum,

$$H_{J=0}^\mu = (p+k)^\mu - \left(\frac{m_B^2 + m_M^2}{q^2} \right) q^\mu f_+(q^2) + \left(\frac{m_B^2 - m_M^2}{q^2} \right) q^\mu f_0(q^2) \quad (4.26)$$

$$H_{J=1}^\mu = \epsilon^{\mu\star} (m_B + m_M) A_1(q^2) - (p+k)^\mu (\epsilon^\star p) \left(\frac{A_2(q^2)}{m_B + m_M} \right) \quad (4.27)$$

$$-q^\mu (\epsilon^\star p) \frac{2m_M}{q^2} (A_3(q^2) - iA_0(q^2)) + \epsilon_{\mu\nu\rho\sigma} \epsilon^{\nu\star} p^\rho k^\sigma \left(\frac{2V(q^2)}{m_B + m_M} \right) \quad (4.28)$$

$$A_3(q^2) = \left(\frac{m_B + m_M}{2m_M} \right) A_1(q^2) - \left(\frac{m_B - m_M}{2m_M} \right) A_2(q^2) \quad (4.29)$$

Here ϵ is the meson M polarization four vector. The form factors are f_+, f_0 for $J = 0$ and A_0, A_1, A_2, A_3 and V for $J = 1$. In HQET, the form factors can be exactly

calculated in the nonrelativistic limit of zero M recoil. Once these are calculated, they can be extrapolated into the $q^2 > 0$ regime.

EvtGen simulates semileptonic B decay with two amplitude decay models. For $B \rightarrow D^* e \nu_e$ and $B \rightarrow D^* \mu \nu_\mu$, the HQET amplitude model is employed:

$$A_1(q^2) = \frac{h_{A_1}(w)}{R^*} \left(1 - \frac{q^2}{(m_B + m_M)^2} \right) \quad (4.30)$$

$$h_{A_1}(w) = h_{A_1}(1)(1 - \rho_{A_1}^2(w - 1)) \quad (4.31)$$

$$w = \frac{m_B^2 + m_M^2 - q^2}{2m_B m_M} \quad (4.32)$$

$$R^* = \frac{2\sqrt{m_B m_M}}{m_B + m_M} \quad (4.33)$$

and $V = R_1 A_1$, $A_2 = R_2 A_1$, $A_0 = 0$. The free parameter $\rho_{A_1}^2$ evolves the form factors into the relativistic regime, while R_1 and R_2 define V and A_2 relative to A_1 . The default values for the free parameters $\rho_{A_1}^2$, R_1 and R_2 in EvtGen are taken from experimental measurements at CLEO [4].

EvtGen employs the ISGW2 decay model for the decays $B \rightarrow D e \nu_e$ and $B \rightarrow D \mu \nu_\mu$ for all semitauonic decays. Here the form factors f_+ , f_- , A_0 , A_1 , A_2 , V are reduced to a single form factor $\xi(w)$ ($w \equiv v_B \cdot v_M$) using the heavy quark limit [48]. Finite quark mass corrections are neglected. The treatment of semileptonic decay in ISGW2 is similar to the HQET decay model in that it calculates the form factor at zero recoil and extrapolates to $q^2 > 0$. The form factor is not obtained from experimental results in the ISGW2 model as they are in the HQET model.

EvtGen simulates the semileptonic B decays with soft pion emission $B \rightarrow D^{(*)}\pi l \nu_l$ using the GOITY_ROBERTS decay model. This model is based on an effective Lagrangian with chiral and heavy quark symmetries described in [49].

In hadronic B decay, the b quark undergoes a transition $b \rightarrow Wq$ ($q = c, u$). The W boson couples to a quark pair $q'q''$, yielding four quarks ($q, q'q''$, and the spectator quark), each of which may exchange gluons with the others during hadronization. This complicates the amplitude calculation greatly. In the *factorization* approximation, the amplitude is written as a product of two-quark hadronic currents.

But in most hadronic B decays, the factorizable part of the amplitude does not dominate. This is due to the presence of four-quark operators in the effective Hamiltonian [50]

$$H_{eff} = \frac{G_F}{\sqrt{2}} \sum_{i=1,2} \left(V_{cb}c_i(\mu)Q_i^{cb} + V_{ub}c_i(\mu)Q_i^{ub} \right) \quad (4.34)$$

These operators Q_i incorporate the effects of soft gluon exchange. Scale dependent *Wilson* coefficients c_i multiply the four-quark operators and thereby account for the new effective weak vertices due to hard gluon exchange. There has been little theoretical progress in describing n -body hadronic B decays for $n > 2$, and in EvtGen these decays are simulated with the PHSP model. Efforts to use the factorization approximation to model 3-body B decays have met with limited success [46]. See Table 4.3 for a partial list of hadronic B decays in EvtGen.

Branching Ratio	Decay Mode	Decay Model
0.0560	$D^*+ e^- \text{ anti-}\nu_e$	PHOTOS HQET 0.92 1.18 0.72
0.0210	$D+ e^- \text{ anti-}\nu_e$	PHOTOS ISGW2
0.0020	$D_0^*+ e^- \text{ anti-}\nu_e$	PHOTOS ISGW2
0.0010	$D^*+ \pi^0 e^- \text{ anti-}\nu_e$	PHOTOS GOITY_ROBERTS
0.0020	$D^*0 \pi^+ e^- \text{ anti-}\nu_e$	PHOTOS GOITY_ROBERTS
0.0030	$D+ \pi^0 e^- \text{ anti-}\nu_e$	PHOTOS GOITY_ROBERTS
0.0060	$D0 \pi^+ e^- \text{ anti-}\nu_e$	PHOTOS GOITY_ROBERTS
0.0560	$D^*+ \mu^- \text{ anti-}\nu_\mu$	PHOTOS HQET 0.92 1.18 0.72
0.0210	$D+ \mu^- \text{ anti-}\nu_\mu$	PHOTOS ISGW2
0.0020	$D_0^*+ \mu^- \text{ anti-}\nu_\mu$	PHOTOS ISGW2
0.0010	$D^*+ \pi^0 \mu^- \text{ anti-}\nu_\mu$	PHOTOS GOITY_ROBERTS
0.0020	$D^*0 \pi^+ \mu^- \text{ anti-}\nu_\mu$	PHOTOS GOITY_ROBERTS
0.0030	$D+ \pi^0 \mu^- \text{ anti-}\nu_\mu$	PHOTOS GOITY_ROBERTS
0.0060	$D0 \pi^+ \mu^- \text{ anti-}\nu_\mu$	PHOTOS GOITY_ROBERTS
0.0160	$D^*+ \tau^- \text{ anti-}\nu_\tau$	ISGW2
0.0070	$D+ \tau^- \text{ anti-}\nu_\tau$	ISGW2
0.0013	$D_0^*+ \tau^- \text{ anti-}\nu_\tau$	ISGW2
0.0027	$D^*+ \pi^-$	SVS
0.0030	$D+ \pi^-$	PHSP
0.0082	$\rho^- D^+$	SVS
0.0068	$\rho^- D^{*+}$	SVV_HELAMP 0.152 1.47 0.936 0 0.317 0.19
0.0010	$D+ \pi^- \pi^0$	PHSP
0.0070	$D^*+ \pi^- \pi^0$	PHSP
0.00834	$a_1^- D^+$	SVS
0.0011	$D+ \rho^0 \pi^-$	PHSP
0.0011	$D+ \rho^- \pi^0$	PHSP
0.0022	$D+ \pi^+ \pi^- \pi^-$	PHSP
0.0120	$D^*+ a_1^-$	SVV_HELAMP 0.336 0.0 0.88 0.0 0.336 0.0

Table 4.3: Above, a select list of semileptonic \bar{B}^0 decay modes simulated by EvtGen together with their branching ratios and decay models. The three parameters in the HQET decay model are the form factor slope ρ_A^2 and form factor ratios R_1 and R_2 , with values taken from CLEO measurements [4]. Below, a select list of hadronic \bar{B}^0 decay modes simulated by EvtGen together with their branching ratios and decay models. The parameters in the SVV_HELAMP decay models are the magnitude and phase of the amplitudes in the helicity state expansion of the D . Taken from the EvtGen DECAY.DEC file.

Two-body hadronic B decays to two mesons $B \rightarrow Mm$ account for roughly 9% (13%) of all B^0 (B^+) decays. In the factorization approximation as applied to two-body decays, the factorizable part dominates the amplitude and the non-factorizable effects can be incorporated in effective parameters which originate in the factorization scheme. In the *color transparency* argument, it is argued that a colorless quark pair $q'q''$ recoiling at relativistic speed away from the interaction region does not interact significantly with the quarks remaining in the interaction region before hadronization of $q'q''$ into a meson m occurs. This lack of color effectively suppresses hard gluon exchange between the $q'q''$ pair and the valence quarks in the meson M at the interaction region, and validates the factorization approximation for the amplitude as a product of the quark currents.

The factorizable part of the two-body hadronic B decay amplitude is written

$$\mathcal{M}_{B \rightarrow Mm} = \frac{G_F}{\sqrt{2}} V_{qb} V_{q'q''}^* x h^\mu H_\mu \quad (4.35)$$

$$H_J^\mu = \langle M_J | \bar{q} \gamma^\mu (1 - \gamma^5) b | B \rangle \quad (4.36)$$

$$h_J^\mu = \langle m_J | \bar{q}' \gamma^\mu (1 - \gamma^5) q'' | 0 \rangle \quad (4.37)$$

where $q^\mu = p_M^\mu - p_m^\mu$. The hadronic current H_J^μ is decomposed with form factors precisely as it was for semileptonic B decay (Equations 4.26 and 4.27). The hadronic current h_J^μ is $h_{J=0}^\mu = f_m q^\mu$ and $h_{J=1}^\mu = f_m \epsilon^\mu$ where ϵ^μ is the polarization vector of the vector meson m and F_m is the *decay constant* for m which describes the overlap of

the two valence quarks $q'q''$ in m .

The factor x in $\mathcal{M}_{B \rightarrow Mm}$ depends in a process dependent way upon the Wilson coefficients. Class I decays proceed via the external diagram in Figure 4.9c, class II decays proceed via the internal diagram in Figure 4.9d, and class III decays proceed via both the internal and external processes [50]. Defining two new parameters

$$a_1 = c_1(\mu_f) + \xi c_2(\mu_f) \quad (4.38)$$

$$a_2 = c_2(\mu_f) + \xi c_1(\mu_f) \quad (4.39)$$

then $x = a_1$ for class I decays, $x = a_2$ for class II decays and $x = a_1 + ya_2$ for class III decays. The Wilson coefficients are evolved down from $\mu^2 = m_W^2$ (where $c_1 = 1$ and $c_2 = 0$) with the renormalization group equations to a factorization scale μ_f at which the factorization approximation is valid. To incorporate nonfactorizable effects in the amplitude, the parameters c_1, c_2 and ξ are free and are taken as effective parameters taken from experiment.

In EvtGen, two-body B decays are simulated with the PHSP model for $J_M = J_m = 0$, the SVS amplitude model for $J_M = 1$ and $J_m = 0$ or $J_M = 0$ and $J_m = 1$ and the SVV_HELAMP model for $J_M = J_m = 1$. Thus the factorization scheme is only partially employed (in the SVS model) though the form factors in H_J^μ available

Branching Ratio	Decay Mode	Decay Model
0.6830	D0 pi+	VSS
0.3060	D+ pi0	VSS
0.0110	D+ gamma	VSP_PWAVE
0.6190	D0 pi0	VSS
0.3810	D0 gamma	VSP_PWAVE

Table 4.4: The complete list of hadronic D^* decay modes simulated by EvtGen together with their branching ratios and decay models. The branching ratios sum to unity. Taken from the EvtGen DECAY.DEC file.

from semileptonic decay are not exploited. In the SVV_HELAMP amplitude model, the coefficients $H_{\lambda_b \lambda_c}$ in the helicity state expansion of the amplitude for the process $a \rightarrow bc$ [41]

$$\mathcal{M}_{a \rightarrow bc} = \sqrt{\frac{2J_a + 1}{4\pi}} D_{M_a, \lambda_b - \lambda_c}^{J_a}(\phi, \theta, -\phi) H_{\lambda_b \lambda_c} \quad (4.40)$$

are specified directly by the user as input parameters. The default coefficients for $B \rightarrow D^* \rho$ and $B \rightarrow D^* a_1$ are taken from experiment. In other cases they are one.

The D^{*0} (D^{*+}) meson decays via the strong interaction with a mass of 2.007 GeV (2.010 GeV). For all modes not involving direct production of a photon ($D^{*0} \rightarrow D^0 \pi^0$, $D^{*+} \rightarrow D^0 \pi^+$ and $D^{*+} \rightarrow D^+ \pi^0$) EvtGen uses the VSS amplitude model. For modes involving direct production of a photon ($D^{*0} \rightarrow D^0 \gamma$ and $D^{*+} \rightarrow D^+ \gamma$) EvtGen uses the VSP_PWAVE amplitude model to simulate the required $l = 1$ orbital angular momentum final state. See Table 4.4 for a complete list of D^* decays simulated in EvtGen.

The D^0 (D^+) meson decays via the weak interaction with a somewhat shorter lifetime than the B , namely 0.4126 ± 0.0028 ps (1.051 ± 0.013 ps). The D^0 lifetime is shorter than the D^+ because of the two-body hadronic D decays, which dominate D decay (in contrast to B decay), the class III decays undergo destructive interference between internal and external diagrams [47]. The D^0 (D^+) mass is 1.8645 ± 0.0005 GeV (1.8693 ± 0.0005 GeV), allowing decays to strange and up/down mesons as well as electrons and muons. The Feynman diagrams for D decays are the same as for B decay in Figure 4.9 except the transition b quark is replaced by a transition c quark.

Leptonic decays of the D^+ are helicity suppressed, but the CKM suppression is lighter than it is for leptonic B decay since $|V_{cd}|^2 \approx 0.05$. In EvtGen they are simulated with the SLN amplitude model with branching ratios of 0.02% for muonic and 0.24% for tauonic decay. All semileptonic D decays, which account for roughly 22.4% (26.9%) of all D^0 (D^+) decays, are simulated with the ISGW2 model. Semileptonic decays with soft pion emission are handled by the PHSP model.

As with the B , hadronic decays of the D dominate its width. In contrast to the B , most hadronic D decays are resonant two body decays. The $D \rightarrow K\pi$ modes account for 2.9% (5.9%) of all D^0 (D^+) modes and are simulated with the PHSP model. The $D \rightarrow K2\pi$ modes are mostly resonant and account for 19.3% (18.7%) of all D^0 (D^+) decays. In EvtGen they are simulated with the D_DALITZ probability model. The $D \rightarrow K3\pi$ modes account for 32.4% (13.4%) of D^0 (D^+) decays and are handled

by PHSP models (with the exception of the resonant a_1 decay $D^+ \rightarrow K^- \pi^+ \pi^+ \pi^0$, which is simulated with the SVS model). See Table 4.5 for a partial list of hadronic D decays.

4.3. Detector Physics Simulation

The GEANT4 Detector Simulator

The complex task of simulating the progress of particles generated by EvtGen and other generators through the Babar detector is carried out by GEANT4, an object-oriented C++ toolkit developed and maintained by an international collaboration dispersed in numerous high energy physics experiments.

The properties of particles in GEANT4 are defined in an instance of a *particle definition* class. This object includes the mass, charge, spin, parity and all other static properties together with a list of physics processes to which the particle is subject. The properties are specified with units defined in the *unit definition* class instance. Most commonly occurring particles are predefined in GEANT4.

In any GEANT4 application [51], the developer first specifies the means of obtaining a primary event, the detector construction and the list of physics processes to be simulated. Primary event generation is either with simple particle guns or by interface with an external event generator. Detector construction begins by defining *solids* as boxes, cones, tubes, spheres, wedges, tori or any intersection, union or sub-

Branching Ratio	Decay Mode	Decay Model
0.0289	anti-K0 pi+	PHSP
0.0800	a_1+ anti-K0	SVS
0.0508	anti-K'_10 pi+	SVS
0.0115	anti-K*0N pi+	PHSP
0.0210	anti-K*0 rho+	SVV_HELAMP 1.0 0.0 1.0 0.0 1.0 0.0
0.0900	K- pi+ pi+	D_DALITZ
0.0970	anti-K0 pi+ pi0	D_DALITZ
0.0100	anti-K0 eta pi+	PHSP
0.0050	anti-K0 rho0 pi+	PHSP
0.0050	anti-K0 omega pi+	PHSP
0.0110	K- rho+ pi+	PHSP
0.0070	K*- pi+ pi+	PHSP
0.0100	anti-K*0 pi0 pi+	PHSP
0.0100	anti-K*0 eta pi+	PHSP
0.0078	anti-K*0 rho0 pi+	PHSP
0.0050	anti-K*0 omega pi+	PHSP
0.0100	K*- rho+ pi+	PHSP
0.0120	K- pi+ pi+ pi0	PHSP
0.0383	K- pi+	PHSP
0.0212	anti-K0 pi0	PHSP
0.0071	anti-K0 eta	PHSP
0.0172	anti-K0 eta'	PHSP
0.0210	omega anti-K0	SVS
0.0190	anti-K*0 eta	SVS
0.0020	anti-K*0 eta'	SVS
0.0730	a_1+ K-	SVS
0.0610	K*- rho+	SVV_HELAMP 1.0 0.0 1.0 0.0 1.0 0.0
0.0146	anti-K*0 rho0	SVV_HELAMP 1.0 0.0 1.0 0.0 1.0 0.0
0.0110	anti-K*0 omega	SVV_HELAMP 1.0 0.0 1.0 0.0 1.0 0.0
0.1390	K- pi+ pi0	D_DALITZ
0.0085	K*BR pi0	SVS
0.0107	K_1- pi+	SVS
0.0071	anti-K_10 pi0	SVS
0.0540	anti-K0 pi+ pi-	D_DALITZ

Table 4.5: Above, a select list of hadronic D^+ decay modes with one kaon in the final state simulated by EvtGen together with their branching ratios and decay models. Below, a select list of hadronic D^0 decay modes with one kaon in the final state simulated by EvtGen together with their branching ratios and decay models. The branching ratios sum to $< 77.525\%$. Taken from the EvtGen DECAY.DEC file.

traction of these solids. Each solid is associated to a *material* which fills it to define a *logical volume* with macroscopic properties characteristic of the material: density, temperature, physical state, etc. Materials are either generated directly, by defining these properties, or indirectly, by defining constituent *elements* and *isotopes*, each with microscopic properties which determine the material's macroscopic properties. Finally, a *physical volume* is created when a logical volume is placed spatially in a mother volume. The detector is constructed as a union of physical solids. An electric or magnetic field can then be constructed in the detector volume.

After the detector has been constructed, the developer specifies the physics processes to be simulated. Broadly, GEANT4 simulates particle decay, electromagnetic interactions, hadronic interactions and optical photon interactions. Each process is implemented as a concrete instance of a *process* virtual class with methods to generate the interaction length for the process and to carry out the process by altering the spatial and dynamic properties of the particle undergoing the interaction. Provision is made for both discrete processes and continuous processes in the process class.

The simulation of the user defined physics and detector geometry is managed by an instance of a *run manager* class. After initializing a *run* class instance with the geometry and physics, the run manager repeatedly fetches a primary event. For each event, it invokes a *event manager* class instance to manage the *event* class instance. For each particle in the primary event, the event manager passes a *track* to the *tracking manager* to carry out the tracking of the particle through the detector. This is

accomplished by repeatedly calling the *stepping manager* to step the particle through the detector material with all the physics processes to which it is subject, including the motion generated by an external electric or magnetic field. The GEANT4 default method for solving the equations of motion for the particle in an external field is fourth order Runge-Kutta integration. After tracking the particle until it either has range zero (or below a user specified cutoff) or has exited the detector, a *trajectory* is returned to the event manager, which persists it in the event.

Each particle in the primary event is therefore tracked through the detector by the tracking manager. But unless *sensitive detectors* are associated to the logical volumes in the detector, no information about energy deposition in the detector is persisted to the event. Sensitive detectors are augmented with *readout geometries*, which allow the developer to define segmentation (into electronics channels) which is not inherent in the logical volume. After a step, each sensitive detector class instance invokes a method to generate energy deposits in the form of GHits, collections of which are persisted to the event.

The stepping manager is responsible for applying all applicable physics processes to a particle while it is being tracked through the detector. Whether it is an interaction or a decay, a process is characterized by a mean free path λ , which is calculated by GEANT4 either from a particle lifetime or from a cross section together with

information about the transited material. The probability of surviving a distance l before undergoing the process is

$$P(l) = \exp \left[- \int_0^l ds / \lambda(s) \right] \quad (4.41)$$

where $\lambda(s)$ indicates that the mean free path may change along the path. To determine the distance traveled by the particle before interacting (or decaying), a random number R on the unit interval is chosen for $P(l)$ and the distance l is determined. In the limiting case where the mean free path is constant along the path, the distance is $l = -\lambda \ln R$.

Each physics process proposes its free path travel distance to the stepping manager for consideration as the next step length. The stepping manager chooses for the next step length the minimum of the smallest proposed distance and the distance to the nearest volume boundary. The process with the shortest travel distance is carried out and the distance required for the remaining processes decreased by the step size. The trajectory is updated and the mean free paths are updated based on the particle's new position. Unless the process is a decay or the range is zero (or below a user specified cutoff), the next step is carried out in a similar way.

The full range of physics processes simulated by GEANT4 is documented in [52]. The ones most relevant to high energy physics experiments are multiple scattering, ionization, bremsstrahlung, positron annihilation, synchrotron radiation, Cherenkov

radiation, crystal scintillation, elastic and inelastic scattering, the photoelectric effect, conversion, neutron transport, hadron absorption, antihadron annihilation, muon capture, and decay.

Babar Geometry and Tracking in GEANT4

The Babar detector simulation implemented in Bogus is strongly based on the GEANT4 toolkit with a few modifications. Run control is taken away from the GEANT4 run manager. Bogus classes inherit from GEANT4 classes with some modification. Since fourth order Runge-Kutta integration was deemed too slow and imprecise for Babar simulation, Bogus uses a different stepping manager to track particles through the Babar magnetic field. The Bogus stepper uses perfect helix segments for step paths through regions where the field variation is small. Finally, event decay trees are fully simulated by the primary event generator so that GEANT4 decays no particles.²

Detector construction in Bogus is handled exclusively by the volume, material and sensitive detector classes in GEANT4. Each detector subsystem employs a class with a method for both constructing that subsystem and setting the particle range cuts specific to the subsystem. The PEP-II class builds the beampipe, the $B1$ and $Q1$ magnets, the ion pump, the support tube and the beampipe plugs. The SVT class builds the five layers (each of which is a sensitive detector), the space frame, the

²In the simulation production cycle SP3, the K_S decay was mistakenly implemented in both EvtGen and GEANT4. Recipes for eliminating one of the decays from the event were prescribed and subsequent SP cycles fixed the error.

support cones, cooling rings, RF shields, and pin diodes. The DCH class builds each of the forty layers as cylindrical volumes filled with He-Isobutane gas, associating each to a sensitive detector. The DIRC class defines the quartz bars as sensitive detectors and the remaining associated structural supports. The EMC class defines each crystal cell as a logical volume filled with CsI(Th) material and associates it to a sensitive detector. Finally, the IFR class builds the flux return frame as a logical volume filled with Fe material and the RPCs as sensitive detectors. See Table 4.6 for the simplified `Construct` methods used in building the DCH subsystem.

The list of GEANT4 physics processes employed in the Bogus simulation include multiple scattering of all particles, leptonic and hadronic ionization, leptonic bremsstrahlung, leptonic pair production, positron annihilation, the photoelectric effect, and Compton scattering. The performance of the Bogus simulation of these processes in the Babar detector was evaluated in [53], which compared simulation with data for dE/dx in the DCH (ionization), electromagnetic shower shape in the EMC (all γ and e processes) and π^0 mass reconstruction (all γ and e processes). Using radiative Bhabha events, the electron dE/dx distributions shapes agree well. Their normalizations agree to within 15% while their means agree within 1%. Radiative Bhabha events were also used to generate lateral electromagnetic shower shape distributions initiated by electron with energies between 1 and 5 GeV. The shapes

agree well but with a moderate shift of the simulation peak higher than data by approximately 60 MeV. Neutral pion mass reconstruction means agreed within 0.6% while their standard deviations agreed to within 13%.

Babar Detector Response

Each subsystem must simulate the digital response of the subsystem electronics to the information encoded in the GHits deposited in the active detector subsystem regions by GEANT4. In order to accurately simulate data taken from the detector, background digis taken directly from data using a cyclic trigger triggering at 1 Hz are mixed in with the digis generated from the GHits. Finally, the combined set of digis is presented to the L1 Trigger simulation.

The procedure for generating digis from GHits is specific to the subsystem in which the GHit is deposited. For purposes of illustration, we consider only the procedure for the DCH [54]. The GEANT4 model for the DCH defines the material for the inner and outer walls, the endplates and the He-Isobutane filled interior (corrected for the presence of sense and field wires). The sensitive detectors are defined to map to each of the forty cell layers. Thus the GEANT4 simulation does not simulate the individual cell response. Rather, the cell response is accomplished in the conversion from GHits to digis. For each layer with a GHit, a helical trajectory is extrapolated into the layer based on the entry point and entry momentum. The point of closest approach from the helix to each cell (in the range of possible hit cells) is calculated. If

```

void BgsDchFullModel::Construct() {
    // Create envelope volume and place it into babar
    _DchCylinder.Construct( theDchGeom, babar );
    // Set up region and cuts for entire DCH
    G4LogicalVolume* regionVol=_DchCylinder.getDCHALogical();
    cutManager->SetDefaultParticleCut(regionVol,
control->GetDchRangeCut()*mm);
    // Define the layers
    G4LogicalVolume* MotherVol=_DchCylinder.getDCHGlogical();
    for( int lay=1; lay <= theDchGeom->nLayers(); lay++ ) {
        G4VSolid* hype = theDchGeom->getDchDBHype( lay,
nameDaughter );
        G4Material* HeIbu=theBgsEnv->getMaterial("dch-He-Ibu-Wir");
        _loglayer[lay-1] = new G4LogicalVolume(hype, HeIbu,
nameDaughter, 0, 0, 0 );
        _loglayer[lay-1]->SetVisAttributes(new
G4VisAttributes(_DCHLcolor));
        _physlayer[lay-1] = new G4PVPlacement( 0,
G4ThreeVector(), _loglayer[lay-1],
nameDaughter + "_phys", MotherVol, false, lay );
    }
}
}

```

Table 4.6: The Construct method for the BgsDchFullModel class in Bogus. This method defines the geometry for the DCH in GEANT4. The code has been simplified for ease of reading.

the point lies within the cell, the time of flight, charge deposition, and pathlength are recorded for that cell. Inoperative (or *dead*) cells with GHits do not produce digis. Each such hit cell represents a candidate digi. The cell charge is smeared and the hit time is calculated and smeared. Any two digis located in the same cell are merged. A digi is created from a digi candidate if it passes a cell inefficiency simulation designed to incorporate constant inefficiencies as well as charge- and pathlength-dependent inefficiencies. Since a charged cell may induce a charge on a neighboring cell (with probability $\approx 4\%$), *crosstalk* digis are generated and merged with the other digis.

Since data events include digis generated by machine background, the digis produced from Monte Carlo simulation GHits are merged with digis taken directly from 1 Hz data snapshots of the subsystem electronics [55]. This procedure is followed for the SVT, DCH, EMC and DIRC. In the case of the EMC, the digis are first converted to waveforms to represent the analog output of the EMC crystal photodiodes. The Monte Carlo digis are converted to waveforms based on a formula, while the background digis are converted with lookup tables taken directly from data. The waveforms are then synchronized, mixed and converted back to digis.

After background mixing, the digis from the DCH and EMC are passed to the L1 Trigger simulation. Trigger primitives are generated from the digis and, if they generate an L1 Accept, are synchronized to the L1 Accept time. At this stage the Monte Carlo simulated data is passed on to the L3 Trigger and reconstruction software precisely as if it had been data taken directly from the detector.

Chapter 5

$B^0 \rightarrow \tau^+ \tau^-$ SELECTION

This chapter describes the selection criteria for isolating signal events from background events in the Babar detector. It begins with a description of the simulation and data samples used in the analysis. It then describes the criteria used for identifying particle candidates and the technique for reconstructing one of the two B mesons produced in a given event at Babar using those candidate particles. Next, the requirements placed on the other B meson in order to select signal characteristics and reject background characteristics are outlined. The structure and training of a neural network to identify and exploit minute distinguishing correlations among observable parameters are then described. Finally, the chapter describes the performance of the neural network in a control sample of data selected to control for the K_L and lost particle backgrounds. No data with the full selection is shown in order to remain blind, but the control sample establishes the legitimacy of the signal selection procedure.

5.1. Data and Simulation Samples

We analyzed Runs 1 through 4 data (startup to 2004 summer shutdown) which yielded 210.35 fb^{-1} of integrated luminosity. See Table 5.1 for the luminosities and

Data Sample	$\sigma_{B^0\bar{B}^0}/nb$	\mathcal{L}/fb^{-1}	$B^0\bar{B}^0$ Events
Run 1	0.5443	19.442	1.0582×10^7
Run 2	0.5512	60.153	3.3158×10^7
Run 3	0.5486	30.992	1.7001×10^7
Run 4	0.5519	99.763	5.5054×10^7
Runs 1-4	0.5505	210.350	1.15795×10^8

Table 5.1: Data samples used in this analysis. Runs 1-4 correspond to data taken from startup in 1999 to summer shutdown in 2004. The effective cross section is obtained from the B count to luminosity ratio.

B counting. The generic simulation samples B0B0bar (hereafter referred to as the *generic neutral B*), BpBm, ccbar, uds and e+e- -> tau+tau- were analyzed to obtain the expected background. See Table 5.2 for signal and background Monte Carlo simulation sample sizes, cross sections and luminosities.

Two modes were simulated for study of the signal $B^0 \rightarrow \tau^+\tau^-$. In the mode B0->tau+tau- +CC (FSR), one B is required to decay to the the signal tau pair and the other is required to decay generically (hereafter referred to as the *signal generic*). The signal decay proceeds with the scalar to two lepton (SLL) generator model and uses PHOTOS for final state radiation. In the mode Weighted B0/Bobar -> tau+tau- vs D(star)X cocktail (hereafter the *signal cocktail*), one B is required to decay to the the signal tau pair and the other is required to decay to one of the high purity modes reconstructed on the tag side in this analysis. All modes are weighted by branching ratio. See Table 5.4 for the prescribed tag B cocktail decay modes.

The dominant expected background contribution to this analysis originates in generic $e^+e^- \rightarrow B^0\bar{B}^0$ events in which one neutral B has been successfully reconstructed and the remaining B mimics the characteristics of the signal $B^0 \rightarrow \tau^+\tau^-$. Therefore, to better train a neural network designed to separate background from signal, we analyzed the mode Weighted B0 -> DX and DstarX cocktail (hereafter the *background cocktail*) in which one B is forced to decay to a mode reconstructed with high purity on the tag side in this analysis. See Table 5.4 for the prescribed tag B decay modes, which are the same for the signal cocktail.

We have employed the prescriptions for remedying known problems in the Monte Carlo samples. Since the Monte Carlo simulation overestimates the efficiencies for particle identification, neutrals reconstruction and track reconstruction, we implement the corrections based on data control samples prescribed by the particle identification, neutrals and tracking working groups.

Comparing the data and simulation reconstruction efficiencies for the various particle candidate selectors, the particle identification working group at Babar [56] found that the simulation overestimates the identification efficiency. The discrepancies vary based on the magnitude and direction of the candidate momentum. The data efficiencies obtained from control samples are provided by the particle identification working group. For the electron and muon selectors employed in this analysis for $B^0 \rightarrow \tau^+\tau^-$, custom tables have been generated by the particle identification working group which only include candidate leptons from the control samples which pass the loose charged

kaon veto. These custom particle identification killing tables have been employed to remove electrons and muons from the candidate lists used in this analysis. The generic tables recommended by the particle identification working group have been employed to remove charged kaons from the candidate lists. Based on the magnitude and polar angle of the candidate's momentum, a probability of reconstruction in a given list is identified from control sample studies. If a random number on the unit interval lies above that probability, the candidate is removed from the selection list.

Comparing the photon energy resolution in $e^+e^- \rightarrow \tau^+\tau^-$ (one-prong on one-prong) simulation and data control samples, the neutrals working group [57] found that the simulation both underestimates the photon energy and overestimates the energy resolution. The summer 2004 scale factors c_{sc} are of order 10^{-3} and the smear factors c_{sm} are of order 10^{-2} . The correction factors are energy dependent and change from run to run. They are provided in table form by the neutrals working group. We first smear the photon energy E resolution obtained in the EMC by resampling the energy from a Gaussian with mean E and width Ec_{sm} , and then scale the resampled energy up by the factor $1 + c_{sc}$.

Finally, the 2004 tracking efficiency task force at Babar [58] recommends tracking reconstruction efficiency corrections. They found that the simulation overestimates the track reconstruction efficiency in $e^+e^- \rightarrow \tau^+\tau^-$ control samples. The correction factors depend on the event track multiplicity, magnitude and direction of the track momenta. Alternatively, the tracking efficiency task force recommends an averaged

Simulation Sample	SP Cycle	σ/nb	\mathcal{L}/fb^{-1}	Events
Signal Generic	SP5	1.63×10^{-8}	1.21×10^7	5.79×10^5
Signal Generic	SP6	1.63×10^{-8}	3.50×10^7	5.70×10^5
Signal Cocktail	SP5	1.70×10^{-10}	4.64×10^9	7.89×10^5
Signal Cocktail	SP6	1.70×10^{-10}	4.26×10^9	7.41×10^5
B0B0bar Cocktail	SP5	5.40×10^{-3}	1.81×10^3	9.75×10^6
B0B0bar Generic	SP5	0.525	400.7	2.103×10^8
B0B0bar Generic	SP6	0.525	640.2	3.361×10^8
BpBm Generic	SP5	0.525	396.2	2.080×10^8
BpBm Generic	SP6	0.525	266.9	1.401×10^8
ccbar Generic	SP5	1.30	110.8	1.441×10^8
ccbar Generic	SP6	1.30	8.692	1.130×10^7
uds Generic	SP5	2.09	117.4	2.453×10^8
uds Generic	SP6	2.09	11.48	2.400×10^7
e+e- -> tau+tau-	SP5	0.94	203.9	1.917×10^8
e+e- -> tau+tau-	SP6	0.94	231.0	2.171×10^8

Table 5.2: Signal and generic background Monte Carlo simulation samples from the BSemiExcl skim used in this analysis. Cross sections are obtained from [3]. The Standard Model expectation $\mathcal{B}^{SM}(B^0 \rightarrow \tau^+ \tau^-) = 3.1 \times 10^{-8}$ is assumed.

flat 0.8% efficiency reduction for reconstruction of loose tracks (GoodTracksLoose)

in the simulation. We chose the flat correction.

5.2. Particle Candidate Selection

Particle candidates are selected from among the lists of tracks and clusters using *selectors*. Selectors are algorithms designed to select candidates with varying criteria from very loose to very tight depending on the desired true selection and corresponding fake rejection rates. The track selector uses information from the DCH and SVT to categorize the candidate tracks. The parameters used are track momentum p , the number of DCH hits associated with the track N_{hit} , the χ^2 of the track fit χ_{trk}^2 and

the z component of the distance of closest approach to the nominal beamspot z_0 . The parameter cut values for `GoodTracksVeryLoose` and `GoodTracksLoose` are found in Table 5.3.

Photons are selected from among the cluster candidates which are required to have at least one seed EMC crystal hit with a minimum energy deposit of 0.01 GeV for isolated crystal hits (or 0.03 GeV for contiguous hits). The photon candidates are selected using information from the EMC for selection and the DCH for veto. The parameters used to select the track candidates are the raw energy deposited in the EMC cluster E_{EMC} , the number of hit crystals in the EMC cluster N_{xll} and a lateral EMC shower shape variable LAT defined by

$$LAT = \frac{\sum_{i=3}^n E_i r_i^2}{E_1 r_0^2 + E_2 r_0^2 + \sum_{i=3}^n E_i r_i^2} \quad (5.1)$$

where n is the number of crystals ranked by energy, r_0 is the distance between crystal centers (5 cm) and r_i is the distance between the cluster centroid and cluster i . Criteria for the lists `GoodPhotonLoose` and for comparison `GoodPhotonDefault` are found in Table 5.3.

The electron selector employed in this analysis is described in [59]. It identifies electrons with the characteristic parameters obtained from the EMC, the DCH and the DIRC. The parameters used are the ionizing energy loss measured in the DCH dE/dx , the difference in ϕ between the EMC shower centroid projected to the face

Parameter	GoodTracksVeryLoose	GoodTracksLoose
p	$< 10\text{GeV}$	$< 10\text{GeV}$
p_t	≥ 0	$\geq 0.1\text{GeV}$
N_{hit}	≥ 4	≥ 12
χ_{trk}^2	≥ 0	≥ 0
z_0	$[-10, 10]\text{cm}$	$[-10, 10]\text{cm}$
Parameter	GoodPhotonLoose	GoodPhotonDefault
E_{EMC}	$\geq 0.03\text{GeV}$	$\geq 0.1\text{GeV}$
N_{xtl}	≥ 1	≥ 1
LAT	≤ 0.8	≤ 0.8
Parameter	eMicroLoose	eMicroTight
dE/dx	$[500, 1000]$	$[500, 1000]$
$\Delta\phi$	—	—
E/p	$[0.65, 5.0]$	$[0.75, 1.3]$
LAT	$[-10, , 10]$	$[0, 0.6]$
$ A_{42} $	$[-10, 10]$	$[-10, 10]$
N_{xtl}	3	3
θ_C	—	—
Parameter	muMicroLoose	muMicroTight
E_{EMC}	$[0.0, 0.5]$	$[0.05, 0.4]$
N_{lyr}	≥ 1	≥ 1
λ	≥ 2	≥ 2.2
$\Delta\lambda$	≤ 2	≤ 1
χ_{trk}^2	≤ 7	≤ 5
χ_{cls}^2	≤ 4	≤ 3
\bar{m}	≤ 10	≤ 8
σ_m	≤ 6	≤ 4
$continuity$	≥ 0.2	≥ 0.3
Parameter	KlongEmcLoose	KlongEmcTight
E_{EMC}	$[0.1, 2.0]\text{GeV}$	$[0.2, 2.0]\text{GeV}$
$\cos\theta_{cls}$	—	$[-1.0, 0.035]$
$P(\chi_{trk}^2)$	—	< 0.001
$R[A_{20}]$	—	$= 4$ if $E_{EMC} < 0.5$
$R[NN(A_{20}, A_{42})]$	—	$= 4$ if $E_{EMC} > 0.5$
A_{20}	—	< 0.8 if $M_{\pi^0} \in [0.1, 0.15]$
$M_{\pi_{mrq}^0}$	—	< 0.11
Parameter	KsLoose	KsDefault
$Q_{\pi\pi}$	0	0
vertexing	no	yes
$M_{\pi\pi}$	$[0.3, 0.7]\text{GeV}$	$[0.347, 0.647]\text{GeV}$

Table 5.3: Cuts used by the selectors employed in this analysis. For comparison, the cuts used by the selector with different criteria are also listed.

and the associated track impact point $\Delta\phi$, the ratio of EMC energy to the momentum of the associated track at its origin E/p , LAT , the Cherenkov angle measured in the DIRC θ_C and the modulus of the shower's Zernike moment of order (4,2) $|A_{42}|$, N_{xtl} . The Zernike moment of order (m,n) is defined by

$$A_{mn} = \frac{m+1}{\pi} \int \int dxdy \rho_E(x,y) V_{mn}^*(x,y) \quad (5.2)$$

where the integration is over the unit disk, $\rho_E(x,y)$ is the energy density of the shower and $V_{mn}(x,y)$ is the Zernike polynomial. The specific parameter values required for `eMicroTight` and, for comparison, `eMicroLoose`, are in Table 5.3.

Muons are identified with the selector described in [60]. This selector identifies muons with the characteristic parameters obtained primarily from the IFR and secondarily from the EMC and DCH. The parameters used by the selector are the number of IFR layers hit N_{lyr} , the energy deposited by the associated track in the EMC E_{EMC} , the number of iron interaction lengths traversed λ , the difference between the expected and measured λ $\Delta\lambda$, the χ^2 of the IFR cluster hits and the extrapolated DCH track χ_{trk}^2 , the χ^2 of the IFR cluster hits and their polynomial fit χ_{cls}^2 , the mean number of IFR strips hit per layer \bar{m} , the standard deviation of the number of IFR strips hit per layer σ_m and the fraction of layers hit between first and last hit layer *continuity*. The specific cut values required for `muMicroTight` and, for comparison, `muMicroLoose`, are in Table 5.3.

Charged kaons are identified with a selector using information from the DIRC, the DCH and the SVT. This selector uses a neural network with a $4 - 10 - 1$ topology to produce a single output from four inputs. The four inputs are the momentum of the candidate p , the ratio of SVT parameter kaon likelihood to the sum of this kaon and the similar pion likelihood, the ratio of DCH parameter kaon likelihood to the sum of this kaon and the similar pion likelihood and the ratio of DIRC parameter kaon likelihood to the sum of this kaon and the similar pion likelihood. These ratios R_{sys} are of the form

$$R_{sys} = \frac{L_K^{sys}}{L_K^{sys} + L_\pi^{sys}} \quad (5.3)$$

where sys indicates the DCH, the SVT and the DIRC. The momentum and Cherenkov angle θ_C dominate the input parameters. For the `KMicroLoose` list, the neural network output cut value is 0.5, and for `KMicroTight` the cut is raised to 0.62 [61].

K_L candidates are identified with information from the EMC using candidates from the cluster list. Cuts are applied to reject both those candidates with associated tracks and those with associated photons from neutral pions. The specific cuts for `KlongEmcLoose` and `KlongEmcTight` are in Table 5.3. The discriminating parameters are E_{EMC} , the cosine of the angle of the EMC cluster with respect to the beam axis $\cos \theta_{cls}$, $P(\chi_{trk}^2)$, the photon rejection level ($R \equiv \epsilon_K/\epsilon_\gamma$) determined by the Zernike moment of order (2,0) $R[A_{20}]$, the invariant mass of the candidate and

any other `CalorClusterNeutral` candidate M_{π^0} and if the candidate is a double bump EMC cluster, the invariant mass of the two bumps $M_{\pi_{mg}^0}$.

Candidate neutral pions are formed from photon candidate pairs taken from the `GoodPhotonsLoose` list and are required to have raw invariant mass in $[0.090, 0.170]$ GeV and energy $E_{\pi^0} > 0.2$ GeV. In the `pi0DefaultMass` list, candidates undergo a mass constrained fit [62].

Candidate K_S are generated with daughter pions taken from the `ChargedTracks` list. The tracks are vertexed and the momenta are recalculated at the vertex. The parameters are the charge of the pion pair $Q_{\pi\pi}$ and the invariant mass of the pion pair $M_{\pi\pi}$. See Table 5.3 for `KsDefault` and `KsLoose` parameter ranges.

Hereafter, a `GoodTracksVeryLoose` candidate will be referred to as a *very loose track*, a `GoodTrackLoose` candidate will be referred to as a *loose track*, a `GoodPhotonLoose` candidate will be referred to as a *loose photon*, a `pi0DefaultMass` candidate will be referred to as a *default neutral pion*, a `eMicroTight` candidate will be referred to as a *tight electron*, a `muMicroTight` candidate will be referred to as a *tight muon*, a `KMicroLoose` candidate will be referred to as a *loose charged kaon*, a `KsDefault` candidate will be referred to as a *default K_S* , and a `KlongEmcTight` candidate will be referred to as a *tight K_L* .

5.3. Tag B Selection

Tag B Reconstruction

For a tag B reconstructed with energy E_B and momentum p_B (in the center-of-mass frame), the definitions for energy-substituted mass and energy difference are employed throughout:

$$m_{ES} = \sqrt{E_{beam}^2 - p_B^2} \quad (5.4)$$

$$\Delta E = E_B - E_{beam} \quad (5.5)$$

where E_{beam} is the calibrated center-of-mass beam energy. Since each B must possess half of the total beam energy in the center-of-mass frame, m_{ES} provides considerably improved resolution on the reconstructed B mass. A correctly reconstructed B will nevertheless have a ΔE near zero.

The tag B reconstruction proceeds by reconstructing a seed $D^{(*)}$ and then adding additional pions and kaons until the system is in a $m_{ES}, \Delta E$ signal region. The reconstructed B^0 composition is $D^{(*)}n\pi mKrK_Sq\pi^0$ with $n+m+r+q < 6$. See Table 5.4 for a list of modes reconstructed. In total, three hundred modes are reconstructed, though many of these modes yield very few signal events relative to the number of background events.

Particle	Prescribed Cocktail Decay
B^0	$D^{(*)}x$
D^{*-}	$D^0\pi^-, D^-\pi^0$
D^-	$K^+\pi^-\pi^-, K_s\pi^-$
D^0	$K^-\pi^+, K^-\pi^+\pi^0, K_s\pi^-\pi^+, a_1^-K^+, K_1^+\pi^-$
x	$K^{*0}\pi^-\pi^+, K^+\pi^-\rho^0, K^+\pi^-\pi^+\pi^-, K^{*0}\rho^0$
	$\pi, \rho, a_1(\rightarrow \rho^0\pi)$
Particle	Reconstructed Decay
B^0	$D^{(*)}X$
D^{*-}	$D^0\pi^-$
D^-	$K_s\pi^-, K^+\pi^-\pi^-, K_S\pi^-\pi^0, K^+\pi^-\pi^-\pi^0, K_S3\pi, K^+K^-\pi^-$
D^0	$K^-\pi^+, K^-\pi^+\pi^0, K^-\pi^+\pi^-\pi^+, K_s\pi^-\pi^+$
X	$\pi, K, \pi\pi^0, K\pi^0, \pi K_S, K K_S, \pi 2\pi^0, K 2\pi^0, 3\pi, K 2\pi, 2K\pi, 3\pi\pi^0, K 2\pi\pi^0$ $2K\pi\pi^0, \pi\pi^0 K_S, K\pi^0 K_S, K 2\pi^0 K_S, 2K_S X, 3\pi 2\pi^0, K 2\pi 2\pi^0, 2K\pi 2\pi^0$ $5\pi, K 4\pi, 2K 3\pi, 5\pi\pi^0, K 4\pi\pi^0, 2K 3\pi\pi^0, 3\pi K_S, K 2\pi K_S, 3\pi K_S\pi^0$

Table 5.4: At top, the prescribed signal and background cocktail tag B decays $B^0 \rightarrow D^{(*)}x$. At bottom, the decay modes reconstructed.

For each distinct mode reconstructed, the ratio of peaking to non-peaking events in the signal region defined by $m_{ES} \in [5.27, 5.29]$ GeV (the *purity*) is determined from a m_{ES} fit to data. After ranking by purity, the modes are combined with all other modes of equal or lower purity and refit, thus defining the integrated purity for the mode in question. From among the many reconstructed candidates in a single event, the B^0 candidate whose mode is reconstructed with the highest integrated purity is selected as the tag B . If the candidate is a charged B the event is rejected.

The semiexclusive tag B reconstruction modes with purity in the intervals $[0.1, 0.5]$, $[0.5, 0.8]$ and $[0.8, 1.0]$ are categorized as the *dirty*, *clean* and *neat* modes respectively. Modes with tag B purity 10% or less (those which are not clean enough even for the dirty category) are rejected. Below 10% purity, the tag B reconstruction modes rarely

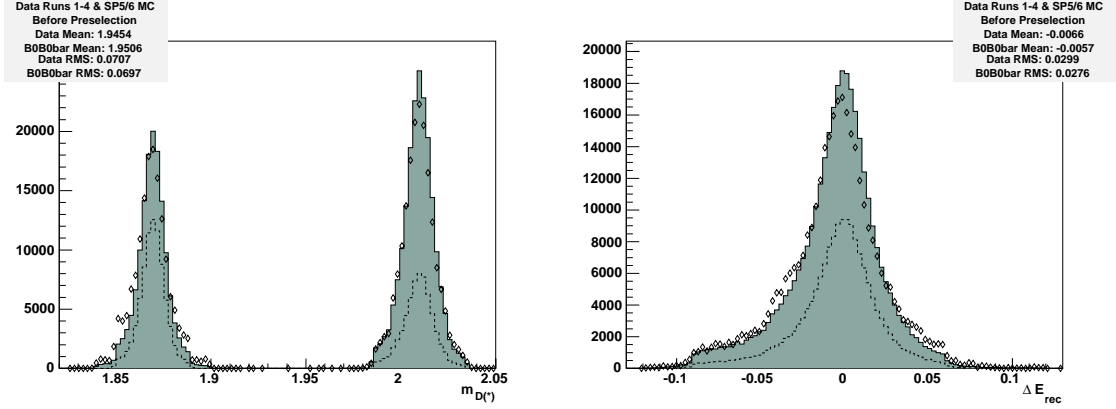


Figure 5.1: At left, the reconstructed mass of the seed D or D^* used in reconstructing the tag B . At right, the ΔE of the tag B . Only the *peaking components* of data (dots), generic neutral B (solid) and the signal cocktail (dashed) are plotted.

have well-defined m_{ES} peaking regions. By eye they are nearly indistinguishable from an Argus function [63]. We therefore impose two quality requirements on the tag B : i) tag B energy-substituted mass $m_{ES} \in [5.2, 5.3]$ GeV and ii) tag B reconstruction mode purity greater than 10%. We require that $m_{ES} \in [5.2, 5.3]$ GeV in order to reject events in which the tag reconstruction has clearly failed to reconstruct a true B with the nominal B mass.

Fitting Procedure and Comparison Plots

The combinatorial and continuum background are subtracted by fitting the m_{ES} distribution. Peaking events lying in the signal region defined by $m_{ES} \in [5.27, 5.29]$ GeV are considered tag B signal.

The m_{ES} fits are maximum likelihood fits performed with the ROOT v3.10/01 [64] interface to the MINUIT v94.1 [65] package. Two probability density functions are

used in constructing the overall fitting function, a single Argus function and a Crystal Ball function:

$$A(m) = m\sqrt{1 - (m/m_c)^2} \exp \left[a \left(1 - (m/m_c)^2 \right) \right] \quad (5.6)$$

$$X(m) = \begin{cases} (1 + \alpha(m - m_0)/\sigma - \alpha^2)^{-n} \exp \left[-\frac{1}{2}\alpha^2 \right] & (m - m_0)/\sigma < \alpha \\ \exp \left[-(m - m_0)^2/2\sigma^2 \right] & (m - m_0)/\sigma \geq \alpha \end{cases} \quad (5.7)$$

The Argus function $A(m; a, m_c)$ models the continuum and combinatorial background. In all cases the Argus cutoff m_c is fixed at half the nominal center-of-mass beam energy ($m_c = 5.29$ GeV). The Crystal Ball function $X(m; \sigma, m_0, \alpha, n)$ models the signal peak with a Gaussian above a cutoff defined by α and a tail with a power n for modeling radiative losses from neutral pion decays. The parameters which are free in the fitting procedure are therefore the Argus shape parameter a , the Gaussian's mean m_0 and width σ , the tail cutoff α , the tail power n and the coefficients c_a and c_x of each of these functions in the overall fitting function

$$F(m; a, m_c, \sigma, m_0, \alpha, n) = c_a A(m; a, m_c) + c_x X(m; \sigma, m_0, \alpha, n) \quad (5.8)$$

In some cases, the tail power n in data samples does not yield a local maximum likelihood for a physical range of values and the fit returns unreliable errors. In this case the tail power in data is fixed to the fitted tail power obtained from the generic neutral B sample.

In order to compare data with Monte Carlo simulation in the parameters used in the analysis chain described in this note, each parameter range is subdivided and m_{ES} fits are performed on the events which lie within that subrange. For purposes of plotting, the ranges of the parameters of the analysis chain are divided into subranges, each of which corresponds to one bin in the parameter plot. With these *bin-by-bin* fits, we are able to compare only the central peaking components between data and Monte Carlo simulation. The aim is to obtain simulation efficiency of peaking components on a bin-by-bin basis, then to multiply this single bin efficiency by the total data tag yield. The signal region purity p is determined by the ratio of the area in the Crystal Ball to the area of the overall fitting function on the interval $[5.27, 5.29]$ GeV:

$$p = \frac{\int_{5.27}^{5.29} dm c_x X(m; \sigma, m_0, \alpha, n)}{\int_{5.27}^{5.29} dm F(m; a, m_c, \sigma_i, m_i)} \quad (5.9)$$

The peak yield is then taken to be pN , the purity times the total number of events N in the signal region $m_{ES} \in [5.27, 5.29]$ GeV. All generic neutral B Monte Carlo simulation histograms are normalized to the data tag yield after preselection (described in the following section), except for those to which the analysis is still blind, in which case the histograms are unnormalized. Signal samples are normalized to half the generic neutral B normalization. See Figure 5.1 for distributions of the tag B ΔE and reconstructed seed $D^{(*)}$ mass after background subtraction using the m_{ES} fits.

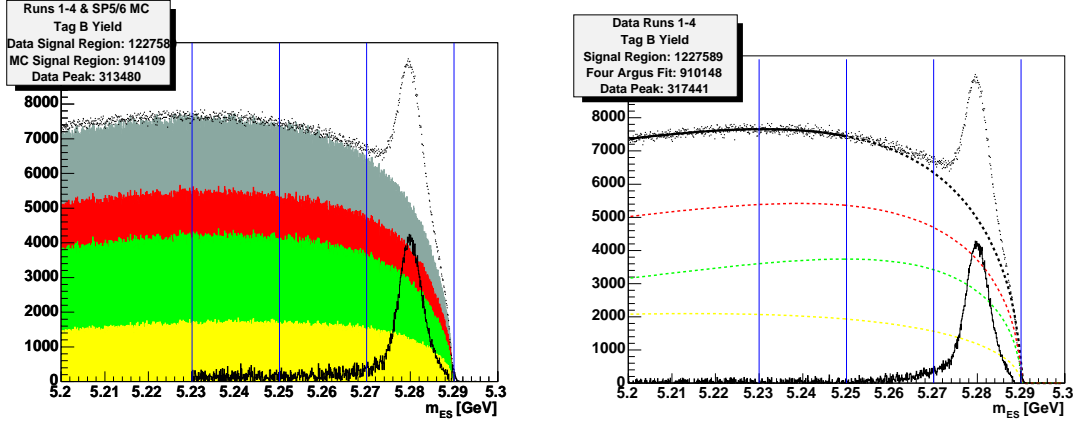


Figure 5.2: At left, Runs 1-4 data (dots) and from top to bottom generic neutral B , $B\rho B\mu$, $c\bar{c}$, $u\bar{d}s$ and $e^+e^- \rightarrow \tau^+\tau^-$ Monte carlo simulation samples (solids). The $e^+e^- \rightarrow \tau^+\tau^-$ component is not large enough to be visible. At right, a four Argus fit to the m_{ES} data distribution.

Tag B Yield

We obtain the total neutral B tag yield $N_{B^0\bar{B}^0}$ by using the continuum and generic charged B simulation samples to model the background. We first fit the generic neutral B m_{ES} distribution with a probability density function composed of a Crystal Ball plus a single Argus. The Crystal Ball component was then subtracted, so that only the combinatorial (*nonpeaking*) component of the neutral B distribution remained. The remaining continuum and charged B distributions were then added without alteration. The overall Monte Carlo simulation distribution has been shifted forward by 0.5 MeV so that its cutoff aligns with the data cutoff, and its normalization has been selected to minimize the mean square error in the region $m_{ES} \in [5.23, 5.25]$ GeV.

In order to obtain an independent estimate of the tag yield $N_{B^0\bar{B}^0}$ and thereby

estimate the tag yield systematic error, we also fitted the background m_{ES} distribution in a region far below the peak. To model the continuum and combinatorial background, we assume a probability density function which is the sum of four Argus functions, one each to model $e^+e^- \rightarrow B^0\bar{B}^0$, B^+B^- , $c\bar{c}$ and $q\bar{q}$ ($q = u, d, s$).

In the fit, the relative proportions of each component are fixed at the values obtained from the simulation samples, but the four Argus shape parameters a are free. The Argus cutoff parameter m_c is fixed at 5.29 GeV for all four Argus functions. The fit is performed only in the region $m_{ES} \in [5.20, 5.25]$, well below the peak tail.

See Figure 5.2 for the semiexclusive tag B m_{ES} distribution. The tag B yield obtained with the four Argus fit is 317441. The tag B yield obtained with the Monte Carlo simulation samples is 313480. The discrepancy is be used to establish a systematic error on $N_{B^0\bar{B}^0}$: $N_{B^0\bar{B}^0} = (3.13 \pm 0.04) \times 10^5$. Note also the absence of a peaking component in continuum and generic B^+B^- simulation samples.

5.4. Signal B Selection

Event Preselection

After applying the prescriptions for correcting known problems in the Monte Carlo simulation, we found that the distributions in data and Monte Carlo simulation did not match. See Figure 5.3 for the signal side very loose track and loose photon multiplicities. The poor agreement is presumably due to spurious events which lack a

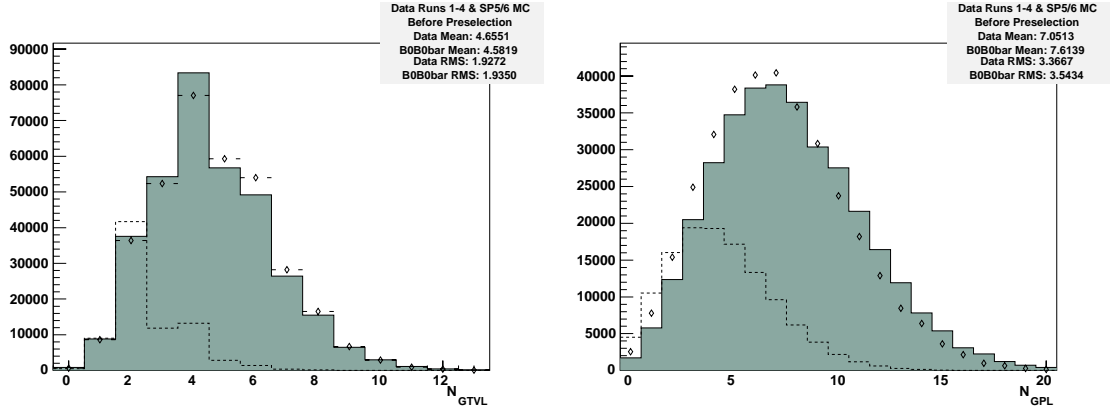


Figure 5.3: At left, the very loose track multiplicity on the signal side. At right, the loose photon multiplicity on the signal side. Only the *peaking components* of data (dots), generic neutral B (solid) and the signal cocktail (dashed) are plotted. The generic neutral B histograms are normalized to the data histograms.

definite physics topology. Therefore three requirements to select a B decay topology are imposed on the samples before beginning this analysis: i) two very loose track candidates reconstructed opposite the tag B , ii) four or fewer loose photons reconstructed opposite the tag B and iii) tag B reconstruction mode purity greater than 12%

We require that there be exactly two track candidates which do not overlap the tag B in the very loose track list. The very loose track criteria require only a minimum of four hits in the DCH and a point of origin within ten centimeters of the nominal interaction point in the z direction. We also require at most four loose photons which do not overlap the tag B , since a single tau decay to a rho particle sanctions two photons. This requirement also allows for bremsstrahlung from tau daughter electrons as well as spurious noise in the calorimeter. Finally, the tag B purity requirement is

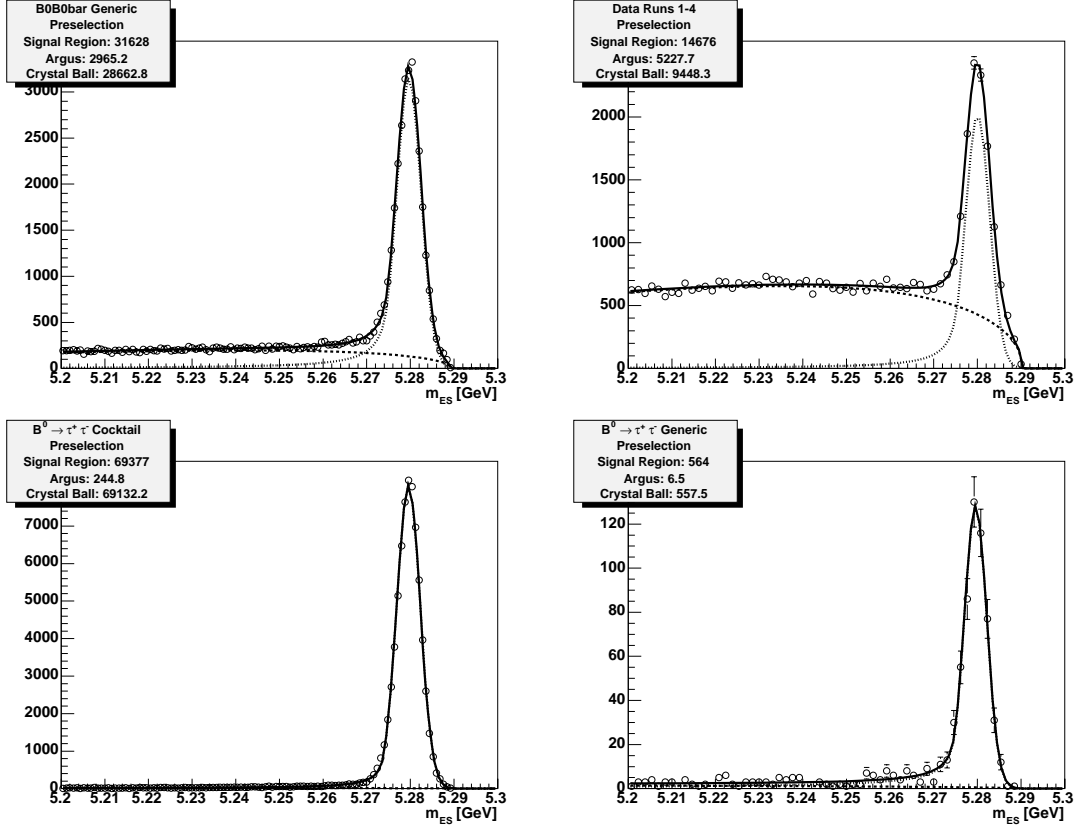


Figure 5.4: Tag yield in the semiexclusive sample after preselection. Clockwise from top left are the generic neutral B , data, signal generic, and signal cocktail samples

tightened to 0.12 or greater. This minimum purity was found to optimize the upper limit (see Section 6.4).

After imposing these requirements, the Monte Carlo simulation and data distributions came into better agreement. See the Appendix for distributions before and after the preselection requirements are imposed. See Figure 5.4 for the m_{ES} distribution fits after the preselection is imposed in the semiexclusive n-tuples of interest to this analysis.

Background Rejection

The background rejection is summarized as follows: i) zero net charge in the two loose signal side tracks, ii) zero loose charged kaon, zero default K_S and zero tight K_L and iii) minimal photon energy remaining unassigned to default neutral pions.

The dominant background to the $B^0 \rightarrow \tau^+ \tau^-$ analysis originates in $e^+ e^- \rightarrow B^0 \bar{B}^0$ events in which the tag B has been successfully reconstructed. The b quark in the signal B candidate undergoes a cascade decay $b \rightarrow W^- c (\rightarrow W^+ s)$ which produces two oppositely charged W bosons and a strange meson produced after hadronization of the strange quark. The W boson pair decay then mimics a tau pair decay and the hadronized strange quark escapes detection. A secondary background originates in events in which two tracks of opposite charge are lost in the uninstrumented forward region of the detector. Typical background events can thus be summarized as follows: either $B^0 \rightarrow D^+ (\rightarrow K_L x_1) x_2$ (where K_L is undetected) or $B^0 \rightarrow D^+ (\rightarrow K^- \pi^+ \pi^+) x$ (where $K^- \pi^+$ are lost forward). In all plots, the dark shaded histogram identifies the component of the simulation background in which a K_L is identified with simulation truth.

The preselection rejects events with very loose track multiplicity other than two in order to reduce background from high multiplicity generic B^0 decays with soft tracks. We now tighten the track selection to reject background from generic B^0 events with only two soft tracks. The loose track criteria reject very loose track candidates with

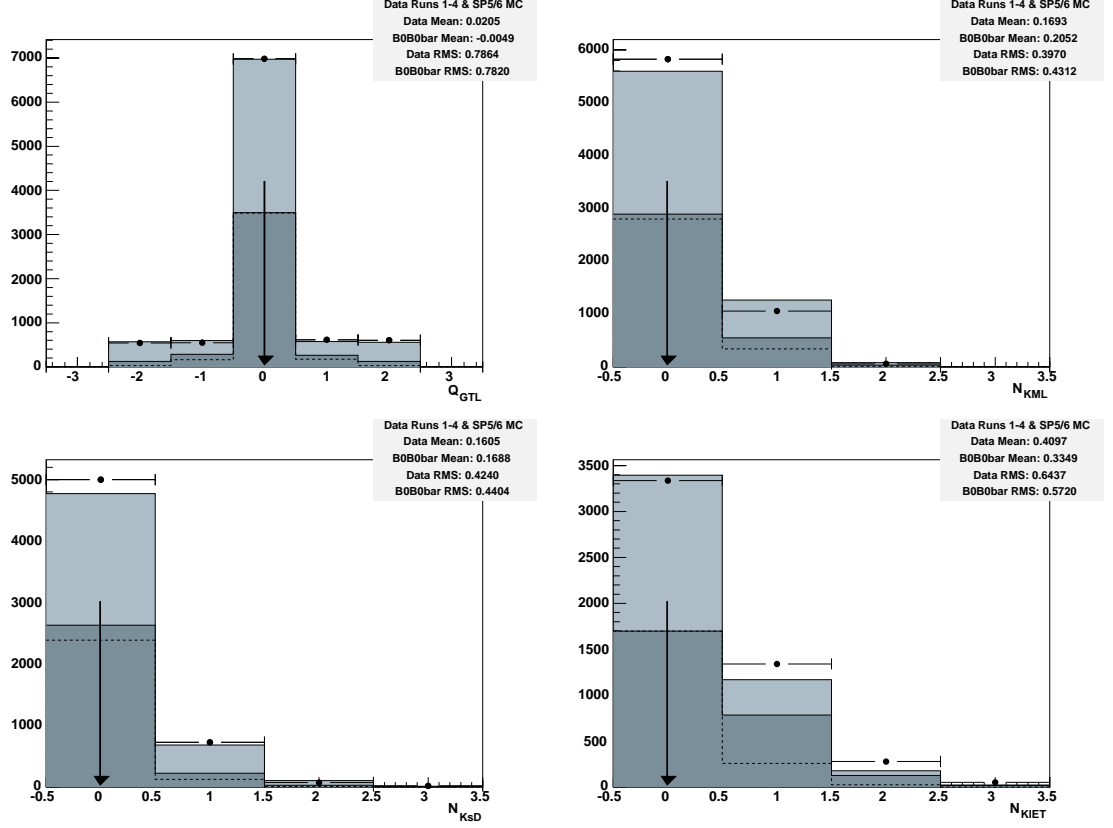


Figure 5.5: Clockwise from top left, the net loose track charge on the signal side, loose kaon, default K_S and tight K_L multiplicity on the signal side after all preceding requirements in the analysis chain have been imposed. Only the *peaking components* of data (dots), generic neutral B (solid) and the signal cocktail (dashed) are plotted. The dark shaded solid (here and in subsequent plots) is the component of the neutral B containing a truth verified K_L .

$p_t < 0.1$ GeV and fewer than 12 DCH hits. We first require a net zero charge in the loose track candidates which have not been attributed to the reconstructed tag B in order to eliminate background from sources in which the tag reconstruction has reconstructed a fake B . This requirement also rejects background in which the tag B has been successfully reconstructed but charged particles from the opposite B have escaped detection and reconstruction as a loose track. We next require that there be exactly two loose track candidates on the signal side. For a plot of net signal side charge in the loose tracks, see Figure 5.5.

At this stage in the analysis chain, most of the remaining generic neutral B Monte Carlo sample originates in $b \rightarrow W^- c (\rightarrow W^+ s)$ decays within a successfully reconstructed and isolated tag B . Therefore we veto events in which a charged or neutral kaon is detected and reconstructed as a loose kaon, default K_S or tight K_L . See Figure 5.5 for candidate kaon multiplicities. In such background cascade events, fake tau daughter momenta will exhibit an asymmetry due to the restricted amount of energy available to the $c \rightarrow sW$ transition which is not observed in the signal decay. The neural network described below is sensitive to correlations between candidate momenta.

The existence of any neutral energy which is not reconstructed in a neutral pion from the signal tau pair or in the reconstructed tag B is a strong indication that unreconstructed neutral pions are present. Therefore we require that the total energy in all candidates in the loose photon list, less the total energy in all candidates in

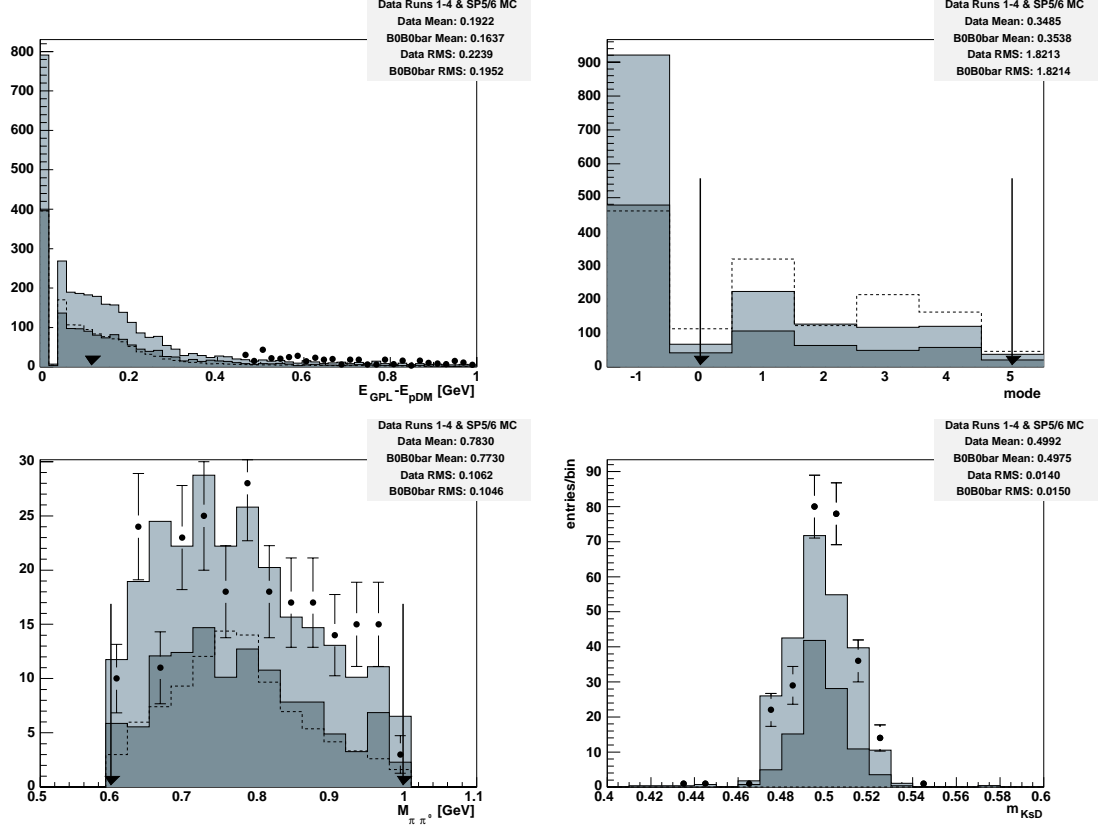


Figure 5.6: At top left, the remaining neutral energy after neutral pion reconstruction (blind). At top right, the ditau reconstruction mode (blind). At bottom left, the mass of the rho candidate. At bottom right, the mass of the K_S candidate in the extra K_S control sample. Only the *peaking components* of data (dots), B0B0bar (solid) are plotted. The dark shaded histogram (here and in subsequent control sample plots) indicates events in which the K_S reconstruction is verified with Monte Carlo truth.

Selection Mode	BR [2]	$N_e + N_\mu$	N_{π^0}	$m_{(\pi\pi^0)}$	Efficiency	Composition
0: $ll'4\nu$	0.124	2	0	na	0.31	0.92
1: $l\pi 3\nu$	0.078	1	0	na	0.53	0.23
2: $l\rho 3\nu$	0.177	1	1	[0.6, 1.0] GeV	0.29	0.68
3: $2\pi 2\nu$	0.012	0	0	na	0.81	0.05
4: $\pi\rho 2\nu$	0.056	0	1	[0.6, 1.0] GeV	0.45	0.18
5: $2\rho 2\nu$	0.063	0	2	[0.6, 1.0] GeV	0.35	0.31

Table 5.5: Branching ratio, signal mode requirements, reconstruction efficiencies and sample composition with respect to all tau pair decay modes in the signal cocktail. The composition is the fraction of events reconstructed in a given mode which are truth verified to be that mode. All requirements are imposed except the neural network selection.

the default neutral pion list, be smaller than 0.11 GeV. This value was obtained in the optimization procedure described in Section 6.4. See Figure 5.6 for the residual photon energy distribution. Since this parameter clearly has discriminating power below 0.11 GeV, it is used as an input in the neural network analysis described in the following section.

Signal Selection

The selection for the signal decays is summarized as follows: i) one tight electron, tight muon, pion or rho with charged particles passing the loose track selection, ii) a second tight electron, tight muon, pion or rho with charged particles passing the loose track selection, iii) neural network output consistent with signal tau daughter momenta, decay mode and residual photon energy and iv) zero additional default neutral pions.

The signal selection requires that any candidate neutral pion can be associated to a charged track candidate under the hypothesis that together they form a rho particle. A lepton must be reconstructed as a candidate in either the tight electron or the tight muon list. Each candidate rho sanctions one neutral pion reconstructed in the default neutral pion list. If a neutral pion has been reconstructed in the default neutral pion list, it must be associated to a loose track candidate which has not been identified in either the tight electron or tight muon list. The invariant mass of the default neutral pion candidate and a loose track candidate is computed as the magnitude of their four vector sum. The invariant mass is required to satisfy $m_{\pi\pi^0} \in [0.6, 1.0]$ GeV. If there is only one default neutral pion, it is assigned to loose track which yields an invariant mass closer to the nominal rho mass. If there are two default neutral pions, they are assigned in such a way that the sum of their squared discrepancy with the nominal rho mass is minimized. See Figure 5.6 for the invariant mass of rho candidates.

The $B^0 \rightarrow \tau^+\tau^-$ signal selection requires the lepton and neutral pion multiplicities to be consistent with a decay mode $\tau^+\tau^- \rightarrow ll'4\nu, l\pi4\nu, l\rho3\nu, 2\pi2\nu, \pi\rho2\nu$ or $2\rho2\nu$. The modes are assigned integers 0, 1, 2, 3, 4, 5 respectively in order to identify them numerically. See Table 5.5 for the signal selection requirements and their efficiency with respect to Monte Carlo truth verified tau pair decay mode after all tag B , background rejection and signal selection requirements are imposed. Any event which does not satisfy the requirements for modes 0, 1, 2, 3, 4 or 5 is assigned a mode of -1 . See Figure 5.6 for the distribution of tau pair reconstruction modes. In the

optimization procedure described in Section 6.4, it was found that the optimal set of signal reconstruction modes is $\tau^+\tau^- \rightarrow ll'4\nu$, $l\pi4\nu$, $2\pi2\nu$, or $2\rho2\nu$. Therefore the modes $\tau^+\tau^- \rightarrow l\rho3\nu$ and $\tau^+\tau^- \rightarrow \pi\rho2\nu$ (modes 2 and 4) are rejected.

Using the momentum of the reconstructed tag B and the mass hypothesis determined by the lepton candidate selection criteria, the tau daughter candidates are boosted to the signal B frame. See Figure 5.7 for reconstructed tau daughter momenta in the signal and background cocktails. Rather than placing requirements on the candidate tau daughter momenta magnitudes and subtended angle, these kinematic parameters are used together with the remaining neutral energy and lepton multiplicity parameters as inputs in a neural network analysis.

In order to best exploit correlations in selection mode, candidate tau daughter momenta and remaining neutral energy, five parameters were used as inputs in a neural network analysis. See Figure 5.8 for the m_{ES} and neural network output distributions, and 5.9 for distributions of the input parameters. The structure and training of the neural network is covered in the following section. The final requirement in the analysis chain is a cut on the neural network output value $N_{out} > 0.52$. This value was obtained by optimizing for the best upper limit on $B^0 \rightarrow \tau^+\tau^-$ in a procedure which will be described in Section 6.4.

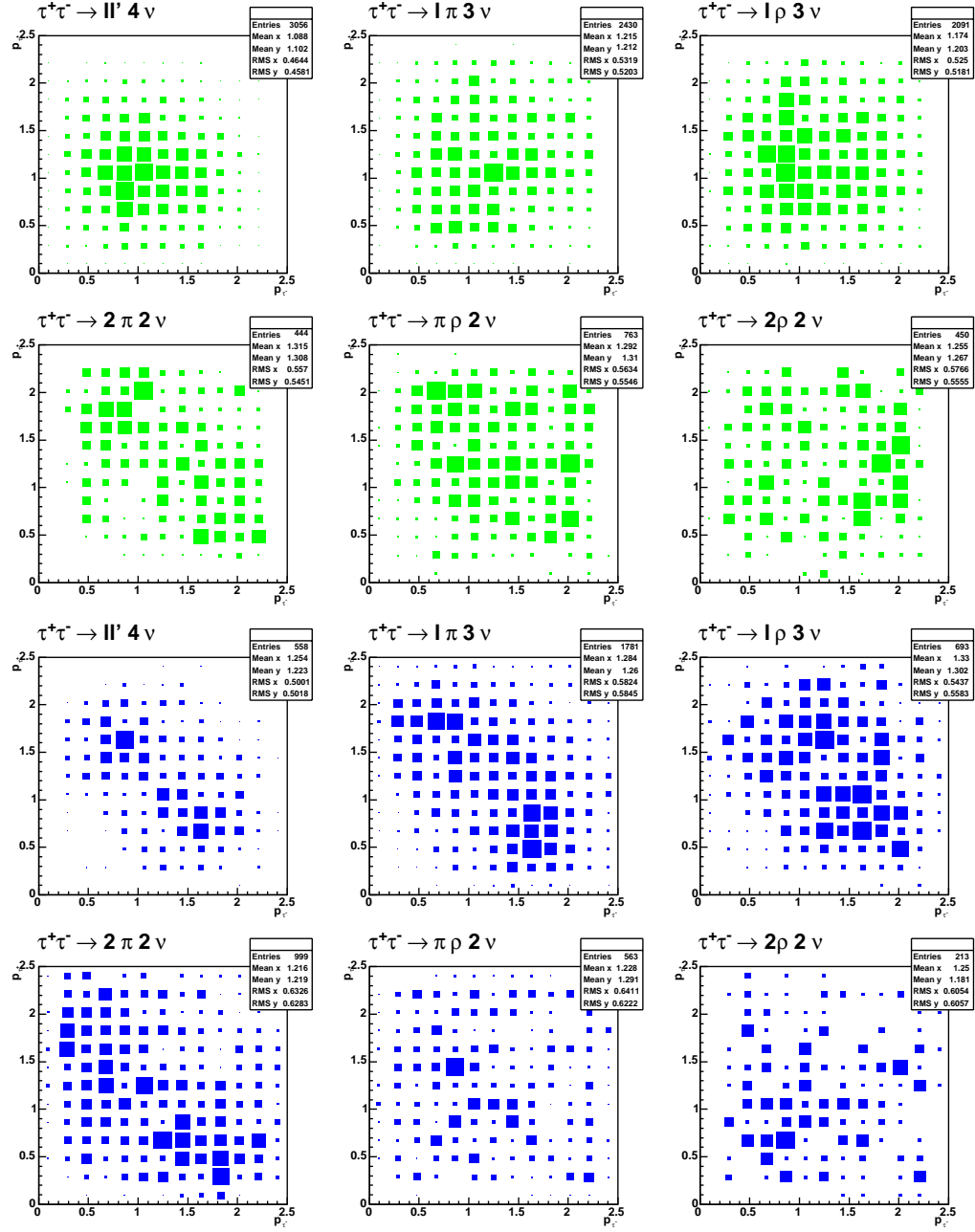


Figure 5.7: Candidate tau daughter pair momenta by mode in the signal (top) and background (bottom) cocktail Monte Carlo sample. All tag B and background rejection requirements are applied. For signal, the signal side mode reconstruction is required to be correct using Monte Carlo truth.

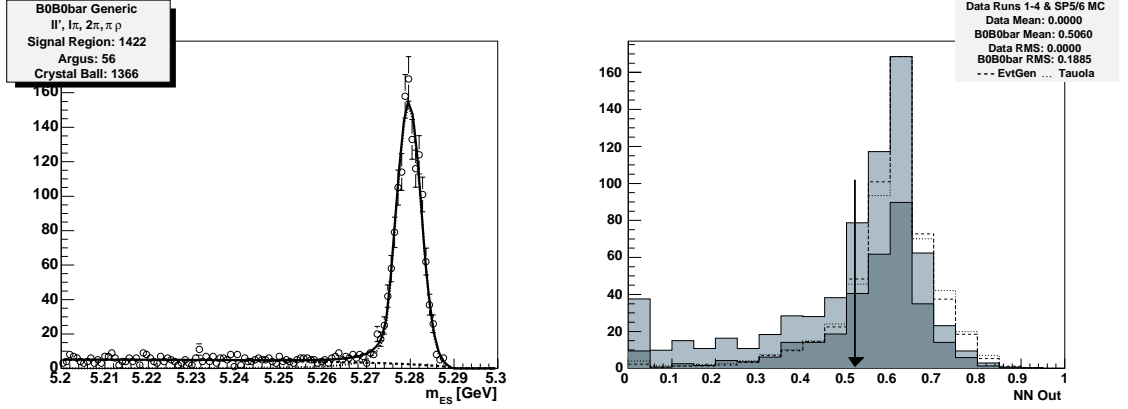


Figure 5.8: The selection for $B \rightarrow \tau^+ \tau^-$. At left, the m_{ES} distribution in Monte Carlo simulation. At right, the neural network output in Monte Carlo simulation. Only the *peaking components* of generic neutral B (solid) and the signal cocktail (dashed) are plotted. For the unblinded version of these plots, see Figure 7.2.

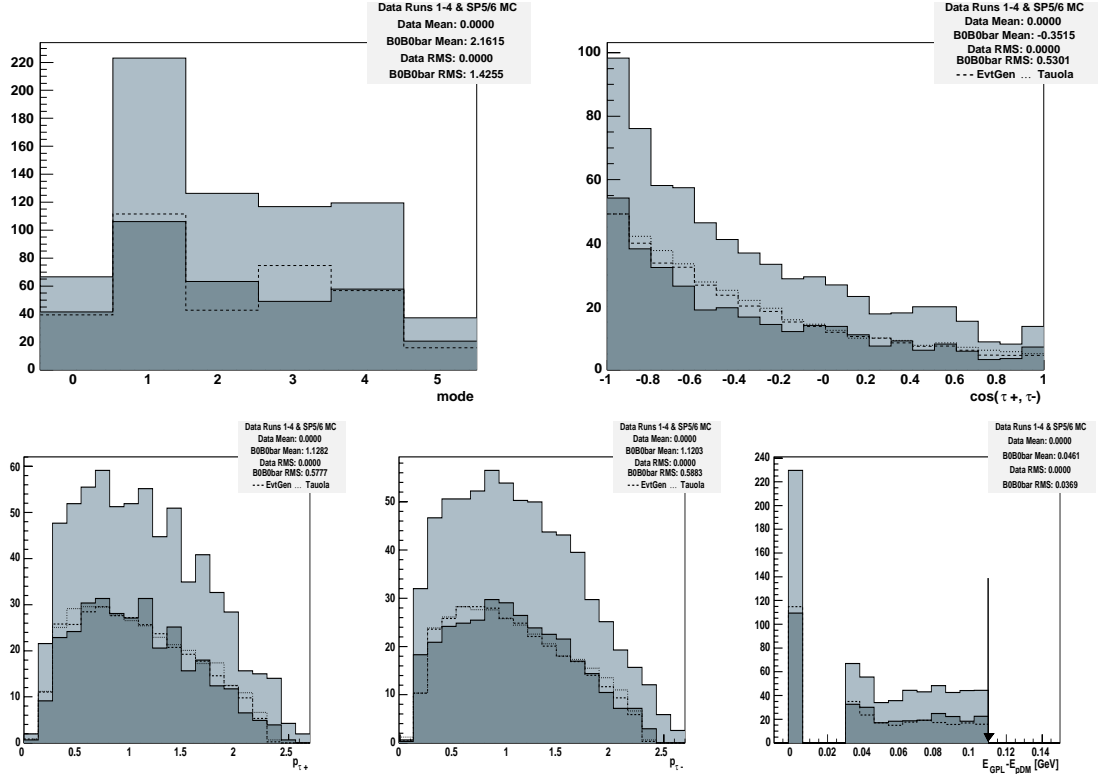


Figure 5.9: Inputs to the neural network for the $B \rightarrow \tau^+ \tau^-$ selection. Clockwise from top left are the signal multiplicity mode, cosine subtended by tau daughter candidate momenta, remaining neutral energy and magnitude of the tau daughter candidate momentum. Only the *peaking components* of data (dots), generic neutral B (solid) and the signal cocktail (dashed) are plotted. For the unblinded version of these plots, see Figure 7.3.

Input Parameter	Scale Map
$mode$	$mode/5$
$p_{\tau+}$	$p_{\tau+}/2.5 \text{ GeV}$
$p_{\tau-}$	$p_{\tau-}/2.5 \text{ GeV}$
$\cos(p_{\tau+}, p_{\tau-})$	$[1 + \cos(p_{\tau+}, p_{\tau-})]/2$
$E_{\gamma} - E_{\pi^0}$	$[E_{\gamma} - E_{\pi^0}]/0.5 \text{ GeV}$

Table 5.6: The inputs for the neural network and their scale maps. The scale maps facilitate training by mapping the inputs to the unit interval

5.5. The Neural Network

The neural network employed in this analysis is a *multilayer perceptron*, characterized by its sigmoidal response, the existence of hidden units and a high degree of connectivity. In a *feed forward* multilayer perceptron, nodes are arranged in layers and a directionality is defined for signal propagation through the layers. The input nodes form the first layer, then hidden units form one or more layers, and finally the output nodes form the last layer.

When updated in *topological order*, the input activation levels are first determined by the signal at the inputs. Then the hidden unit activations in the first hidden layer are calculated based on the outputs of the input layer nodes. The signal thus propagates forward through each layer until the activations of the output layer nodes are calculated based on the activations of the previous layer of hidden units. In a *fully connected* multilayer perceptron, each node in a given layer is connected by links to all nodes in the previous layer.

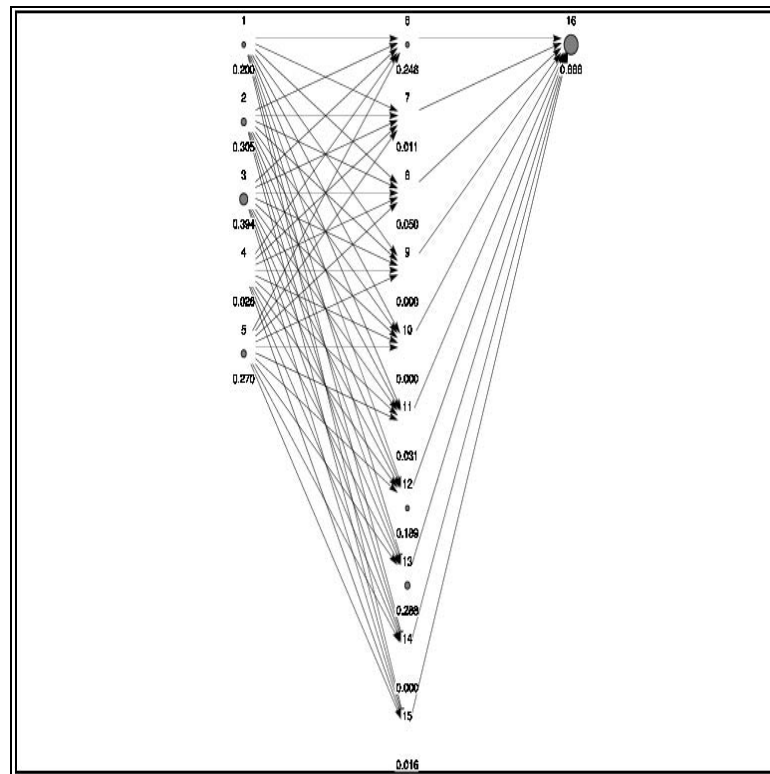


Figure 5.10: The neural network topology. From left to right are input, hidden and output units. The activation level a_i for each node i is displayed.

See Figure 5.10 for a diagram of the topology of the neural network and Table 5.6 for the input parameters and their scale maps. The inputs are first scaled to the unit interval in order to facilitate training.

The activity v_i of node i is defined to be $v_i = \sum_{j \in L} w_{ij} o_j$, where L is the set of nodes in the layer previous to the layer in which the node i lies. The activation level of node i is then defined by the activation function ϕ evaluated at the activity $\phi(v_i)$. If ϕ is a logistic function, which is typical for a multilayer perceptron (and which is true for the analysis described here), then the activation of node i is

$$a_i = \frac{1}{1 + \exp(\theta_i - v_i)} \quad (5.10)$$

where θ_i is the *threshold* (or *bias*) of node i . The node i is thus active ($a_i \approx 1$) when the activity is high compared to the threshold, inactive ($a_i \approx 0$) when the activity is much lower than the threshold, and in transition ($a_i \approx 1/2$) between active and inactive states when the activity is close to the threshold. The output function for the neural network described in this analysis is the identity function: $o_i = a_i$.

Once the topological structure of a neural network is chosen, the weights w and thresholds θ completely characterize the response of a multilayer perceptron. The power of a neural network lies in its ability to adjust these parameters to values which enable the network to correctly model a data sample. The *training* of a neural network is the iterative adjustment of w and θ for each node based on the performance

of the neural network at each iteration.

The goal of training a neural network is *generalization*, which is attained when the network correctly (or nearly correctly) describes the input-output relation ψ in a data sample which was not used to train the network (but which was taken from the same data population). Generalization therefore requires the subdivision of a data population into disjoint *training*, *validation* and *evaluation* sets. The training set generates input patterns and the correct output for the pattern for use in adjusting the weights and thresholds while the validation set provides input patterns and the correct outputs (generated with ψ) for evaluation at each iteration during training. The evaluation set can then be used to evaluate how well the neural network generalizes after training.

Clearly, a neural network's ability to generalize depends on its topological properties and the how one defines "nearly correctly". If M is the number of hidden nodes, W is the number of weights and ϵ is the fraction of permitted errors in describing the input-output relation ψ , then according to [66] a sufficient number of training patterns required for generalization is

$$N \geq \frac{32W}{\epsilon} \ln \left(\frac{32M}{\epsilon} \right) \quad (5.11)$$

It should be emphasized that this is a sufficient condition for generalization. It is not a necessary condition. The theorem assumes implicitly that inputs are, at least

in principle, sufficient to fully separate signal from background, and should therefore only apply to the maximal subset of signal and background events which are, in fact separable. No number of training patterns is sufficient to separate signal from irreducible background.

In the $B^0 \rightarrow \tau^+\tau^-$ analysis, signal and background cocktail samples were separated into training and validation samples in the ratio 4 : 1. The generic signal and neutral B samples provided the evaluation sets. For perfect performance ($\epsilon = 1$), the theorem requires $N \geq 1.2384 \times 10^4$ training patterns. We trained with a training set containing in excess of 2.6×10^6 , comfortably satisfying the criterion for separating signal from irreducible background.

Training using training and validation data sets proceeds as follows. If t_i is the desired response of output node i at iteration n , then $\mathcal{E} = \sum_{i \in O} (t_i - o_i)^2$ quantifies the degree to which the neural network does not correctly reproduce the input-output relation in the data sample. Since it is desirable to minimize \mathcal{E} with respect to each weight, the weight adjustment at each iteration n should be proportional to the partial derivative of \mathcal{E} with respect to w_{ij}^n : $\Delta w_{ij}^n = -\eta \partial \mathcal{E} / \partial w_{ij}^n$. The minus sign indicates that the weight should be decreased for an increasing \mathcal{E} . The positive parameter η is the *learning parameter*, and it determines how finely the weights are adjusted at each step. It can be shown (see [66]) that for a fully connected feed forward multilayer perceptron, this requirement implies that the adjustment for each link connecting forward to node i be given by $\Delta w_{ij}^n = \eta o_i^n \delta_i^n$ where $\delta_i^n = \phi'(v_i^n)(t_i - o_i)$ for output

nodes i and $\delta_i^n = \phi'(v_i^n) \sum_{k \in L} \delta_k^n w_{jk}^n$ for hidden nodes i . Here L denotes the layer lying in front of the node i . In training, the thresholds θ_i are treated as weights w_{i0} of links connecting node i to an imaginary node 0 with constant output $o_0 = -1$. One can normalize the error \mathcal{E} using $RMSE \equiv (\mathcal{E}/(N - W))$, where N is the number of training patterns and W is the number of weights.

The neural network was implemented on the Stuttgart Neural Network Simulator (SNNSv4.2) [67] in a $5 - 10 - 1$ topology. The feed forward network is fully connected and standard backpropagation is the learning algorithm. We separated each of the signal and background cocktail Monte Carlo simulation into two disjoint subsamples, one for purposes of training the neural network and the other for evaluating the neural network performance.

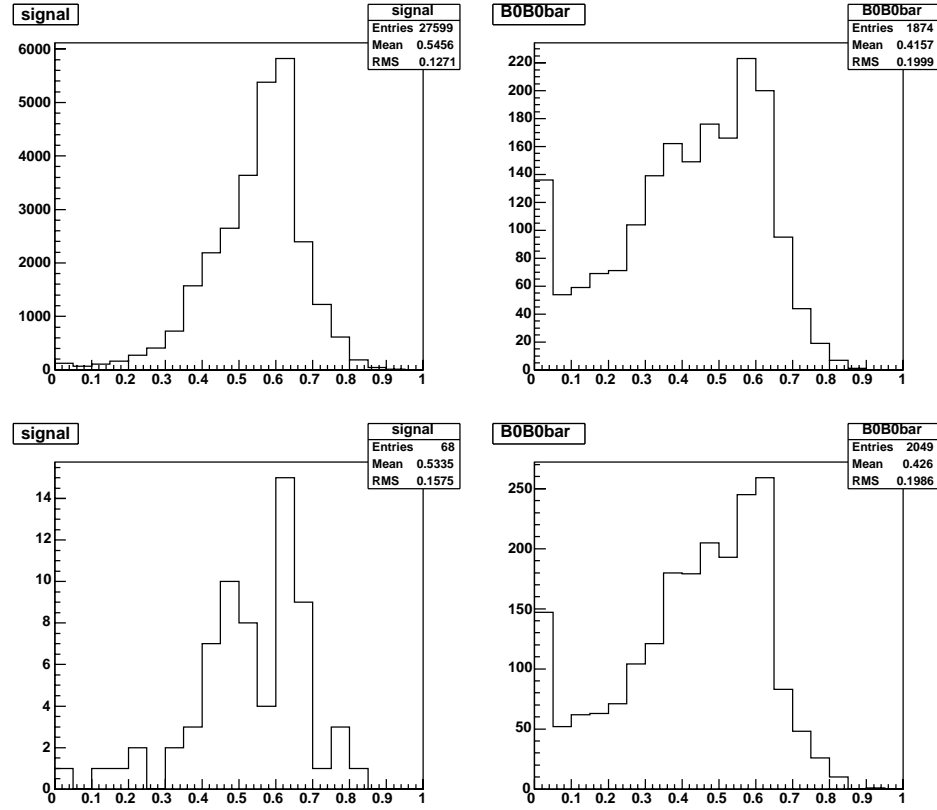


Figure 5.12: Performance of the neural network in the cocktail (top) and generic (bottom) samples. All preceding requirements in the analysis chain are imposed. No background subtraction is performed.

The training required the output to register a 1 for the signal events and a 0 for generic neutral B events. We stopped the neural network training after the minimum root mean square error (RMSE) obtained. See Figure 5.11 for a plot of the cumulative minimum RMSE vs training cycle for the neural network in this analysis. See Figures 5.12 (cocktail samples) and 5.12 (generic samples) for the neural network output in data and Monte Carlo simulation without background subtraction.

5.6. Data Control Sample

To gain confidence that the event selection and neural network performance in data matched its performance in the simulation samples, we studied a sample selected to control for the dominant background source. The selection is orthogonal in one parameter to the analysis chain employed in the previous section for signal selection.

Since K_S are readily reconstructed in the decay $K_S \rightarrow \pi^+\pi^-$, there is an experimentally obtainable data sample which mimics the background to $B^0 \rightarrow \tau^+\tau^-$: the *extra* K_S control sample is the strange meson CP conjugate of the background sample to the signal. In a background B decay, if the strange quark hadronizes into a K_S rather than a K_L , the event is both detectable and will share the topological characteristics of the background event with a K_L . Moreover, when the K_S candidate is a fake, the event will model the secondary background to the signal analysis, namely events in which two oppositely charged particles are lost forward.

In the extra K_S control sample, the requirement $N_{KsD} = 0$ is replaced by the requirement $N_{KsD} = 1$, with the provision that the loose K_S daughter charged pions are invisible to the analysis chain. All other requirements in the signal analysis chain apply, except for the requirement $N_{KlET} = 0$. When a K_S has been reconstructed there is no reason to expect a K_L from a single B decay. See Figure 5.6 for the invariant mass of the reconstructed K_S candidate. See Figure 5.13 for the m_{ES} and neural network output distributions. For the distributions of input parameters in the

Requirement	B0B0bar Monte Carlo		Data Runs 1-4	
	Peak Yield	Efficiency	Peak Yield	Efficiency
Preselection	57095.5 ± 348.9	100.00 ± 0.00	20203.2 ± 344.2	100.00 ± 0.00
$Q_{GTL} = 0$	27009.5 ± 241.0	47.31 ± 0.44	9344.5 ± 176.3	46.25 ± 1.13
$N_{GTL} = 2$	22426.2 ± 198.6	39.28 ± 0.36	7670.0 ± 199.3	37.96 ± 1.15
$N_{KML} = 0$	15435.5 ± 171.5	27.03 ± 0.31	5632.4 ± 164.1	27.88 ± 0.92
$N_{KsD} = 1$	3589.6 ± 76.7	6.29 ± 0.14	1413.9 ± 57.4	7.00 ± 0.30
$E_{res} < 0.11$ GeV	1556.0 ± 44.5	2.73 ± 0.08	562.2 ± 35.4	2.78 ± 0.18
$ll', l\pi, 2\pi, 2\rho$	509.8 ± 24.2	0.89 ± 0.04	188.1 ± 17.0	0.93 ± 0.09
$N_{out} > 0.52$	354.3 ± 18.7	0.62 ± 0.03	135.4 ± 14.3	0.67 ± 0.07

Table 5.7: Cumulative yields and efficiencies for the extra K_S control sample in data and Monte Carlo simulation. Here E_{res} is the residual neutral energy $E_{GPL} - E_{pDM}$. The preselection requires four or fewer loose signal side photons and *four* very loose signal side tracks.

control sample, see Figure 5.14. The efficiencies in data and Monte Carlo simulation are represented in Table 5.7.

The observed number of events in the control sample is 135.4 ± 14.3 . From Monte Carlo simulation, the expected number of events in the control sample is 125.4 ± 6.9 , yielding a relative discrepancy of $(7.3 \pm 11.7)\%$. Modulo error, the observed number of events in the extra K_S control sample agrees with the expected number. Agreement between control sample neural network output distribution shapes in Monte Carlo simulation and data adds assurance that the neural network correctly models the dominant background to this analysis.

Given the expected number of background events, moreover, the number of observed events in the control sample is close to the expectation. If one assumes that the efficiency for default K_S candidates is 55%, as found by the authors in [68], and that

60% of the background originated in events with an unreconstructed K_L , we expect $0.33B$ (where B is the background expectation for $B \rightarrow \tau^+\tau^-$) events with true K_S in the control sample. Adding in bad K_S reconstructions, assuming a purity of roughly 40%, this gives an expectation of $0.50B$ for the control sample yield. Events with an unreconstructed K_L dominate the background, and the extra K_S control sample establishes that the neural network models these events well.

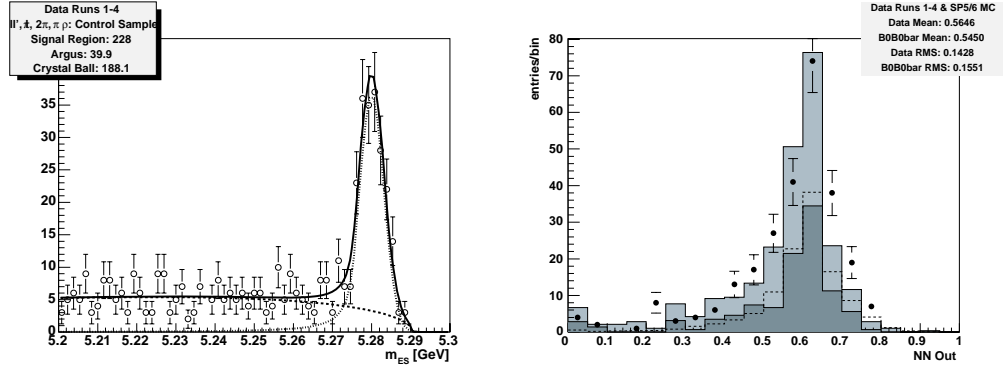


Figure 5.13: The selection for the extra K_S control sample. At left, the m_{ES} distributions in data. At right, the neural network output in data and Monte Carlo samples. Only the *peaking components* of data (dots), B0B0bar (solid) and the signal cocktail (dashed) are plotted.

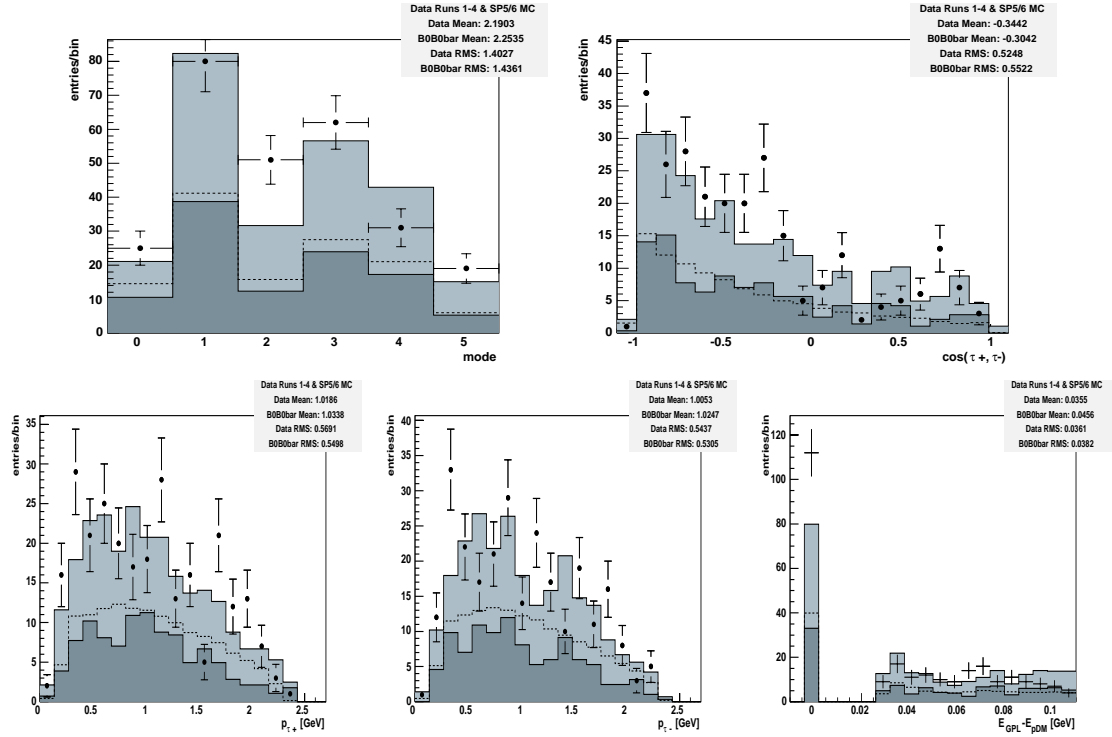


Figure 5.14: Inputs to the neural network for the extra K_S control sample. Clockwise from top left are the signal multiplicity mode, cosine subtended by tau daughter candidate momenta, remaining neutral energy and magnitude of the tau daughter candidate momentum. Only the *peaking components* of data (dots), generic neutral B (solid) and the signal cocktail (dashed) are plotted.

Chapter 6

STATISTICAL ANALYSIS

This chapter obtains the numerical results necessary for determining the measurement of $B^0 \rightarrow \tau^+ \tau^-$. The signal and background simulation samples are subjected to the full signal selection described in Chapter 5 and the survival efficiencies are determined. The analysis remains blind to the data samples for the last three requirements in the analysis chain in order to establish systematic biases without any knowledge of the data yield.

Since the signal decay is not expected to be observed in the data after unblinding, the procedure for establishing an upper limit on the branching ratio $\mathcal{B}(B^0 \rightarrow \tau^+ \tau^-)$ is outlined. All systematic biases which are expected to introduce deviations in the simulation efficiencies from the data efficiencies are described, and systematic errors associated with each bias are evaluated.

The chapter concludes by optimizing the signal selection for the best expected upper limit. The requirements for four parameters referenced in Chapter 5 are chosen such that the expected upper limit is minimized. Finalizing the signal selection and the systematic errors leads to unblinding the analysis in Chapter 7.

6.1. Analysis Chain Efficiencies

Efficiencies for the $B \rightarrow \tau^+\tau^-$ analysis are extracted from the m_{ES} fits using the sum of peaking events in the signal region. Denote by N_i the number of events in the signal region and by p_i the purity after the i th requirement in the analysis chain. Efficiencies for each successive requirement in the analysis chain are calculated with respect to the peak yield with no requirements imposed ($\epsilon_i = N_i p_i / N_0 p_0$), and their error is determined by the combined statistical and fitting error. The signal region survival ratio $y_i \equiv N_i / N_0$ is the efficiency of the i th requirement in the signal region without background subtraction. The background subtraction factor p_i / p_0 is determined from the m_{ES} shapes.

The error on ϵ_i for the simulation samples originates in the statistical error on y_i and the fitting error contained in the purities p_i and p_0 . These errors are

$$\delta_{p_i/p_0} = \frac{p_i}{p_0} \sqrt{\sum_{j,k} \left(\frac{\partial p_i}{\partial x_j} \frac{\partial p_i}{\partial x_k} \frac{C_{jk}^{ii}}{p_i^2} + 2 \frac{\partial p_i}{\partial x_j} \frac{\partial p_0}{\partial x_k} \frac{C_{jk}^{i0}}{p_i^2} + \frac{\partial p_0}{\partial x_j} \frac{\partial p_0}{\partial x_k} \frac{C_{jk}^{00}}{p_0^2} \right)} \quad (6.1)$$

$$\delta_{y_i} = \sqrt{\frac{y_i(1-y_i)}{N_0}}. \quad (6.2)$$

Here C_{jk}^{mn} is the covariance matrix between the m_{ES} fits after the m th and n th analysis chain requirement, and j, k index the free parameters x in the fits. Since the fit parameters at the i th and 0th stages in the analysis chain are expected to be correlated, the terms in δ_{p_i/p_0} involving C_{jk}^{i0} cannot be neglected. But since the

purities and the fitted parameter values vary only very slowly with i (see Tables 6.3 and 6.6), we argue that $\partial_j p_0 \approx \partial_j p_i$, $C_{jk}^{i0} \approx C_{jk}^{ii}$ and $C_{jk}^{i0} \approx C_{jk}^{00}$. Then we get

$$\delta_{p_i/p_0} \approx \frac{p_i}{p_0} \sqrt{2 \sum_{j,k} \left(\frac{\partial p_i}{\partial x_j} \frac{\partial p_i}{\partial x_k} \frac{C_{jk}^{ii}}{p_i^2} + \frac{\partial p_0}{\partial x_j} \frac{\partial p_0}{\partial x_k} \frac{C_{jk}^{00}}{p_0^2} \right)} \quad (6.3)$$

The C_{jk}^{ii} and C_{jk}^{00} are obtained from the fitting program from the second derivative of the likelihood function at the maximum likelihood.

The expansion for the squared efficiency error at second order is

$$\delta_\epsilon^2 = \sum_{x=y_i, p_i, p_0} \sum_{y=y_i, p_i, p_0} \sigma_{xy}^2 \frac{\partial \epsilon}{\partial x} \frac{\partial \epsilon}{\partial y} \quad (6.4)$$

We argue that $\sigma_{y_i p_i}^2$ and $\sigma_{y_i p_0}^2$ are negligible since y_i is a purely statistical ratio while p_i and p_0 are derived from m_{ES} shapes. These parameter errors are uncorrelated. We include the correlations between fit parameters from Equation 6.3 in the error on the efficiency:

$$\delta_\epsilon = \epsilon \sqrt{\delta_{y_i}^2 + \delta_{p_i/p_0}^2}. \quad (6.5)$$

See Table 6.1 for the cumulative efficiencies and their error in data and generic neutral B , and Table 6.4 for cumulative efficiencies in the signal cocktail and generic samples. Both the fit error and the statistical error are reported. For the exclusive efficiencies, for which a single requirement only is imposed, see Table 6.2 for data and

Requirement	B0B0bar Monte Carlo		Data Runs 1-4	
	Peak Yield	Efficiency	Peak Yield	Efficiency
Preselection	28662.8 ± 217.6	100.00 ± 0.00	9448.3 ± 151.9	100.00 ± 0.00
$Q_{GTL} = 0$	21497.7 ± 169.8	75.00 ± 0.57	7062.8 ± 146.3	74.75 ± 1.75
$N_{GTL} = 2$	21384.2 ± 180.1	74.61 ± 0.60	7024.6 ± 145.3	74.35 ± 1.74
$N_{KML} = 0$	17235.5 ± 162.3	60.13 ± 0.55	5888.6 ± 123.9	62.32 ± 1.48
$N_{KsD} = 0$	14701.9 ± 146.0	51.29 ± 0.49	5046.2 ± 103.1	53.41 ± 1.24
$N_{KIET} = 0$	10471.9 ± 115.1	36.53 ± 0.39	3371.6 ± 80.0	35.69 ± 0.93
$E_{res} < 0.11$ GeV	4974.1 ± 74.9	17.35 ± 0.26	<i>blind</i>	<i>blind</i>
$l'l', l\pi, 2\pi, 2\rho$	1372.1 ± 38.5	4.79 ± 0.13	<i>blind</i>	<i>blind</i>
$N_{out} > 0.52$	852.1 ± 30.4	2.97 ± 0.11	<i>blind</i>	<i>blind</i>

Table 6.1: Cumulative yields and efficiencies (in %) for the analysis chain in the Monte Carlo and data samples. The statistical error is added in quadrature with the fit uncertainty. For the unblinded version, see Table 7.3.

Requirement	B0B0bar Monte Carlo		Data Runs 1-4	
	Peak Yield	Efficiency	Peak Yield	Efficiency
Preselection	28662.8 ± 217.6	100.0 ± 0.0	9448.3 ± 151.9	100.0 ± 0.0
$Q_{GTL} = 0$	21497.7 ± 169.8	75.0 ± 0.6	7062.8 ± 146.3	74.8 ± 1.8
$N_{GTL} = 2$	24895.3 ± 228.7	86.9 ± 0.8	8222.6 ± 162.6	87.0 ± 2.0
$N_{KML} = 0$	22722.2 ± 188.6	79.3 ± 0.6	7783.9 ± 157.2	82.4 ± 1.9
$N_{KsD} = 0$	24119.5 ± 253.8	84.1 ± 0.9	7889.9 ± 160.1	83.5 ± 1.9
$N_{KIET} = 0$	20726.5 ± 169.1	72.3 ± 0.6	6345.2 ± 137.2	67.2 ± 1.6
$E_{res} < 0.11$ GeV	11540.3 ± 123.2	40.3 ± 0.4	3580.7 ± 117.6	37.9 ± 1.3
$l'l', l\pi, 2\pi, 2\rho$	10295.1 ± 114.4	35.9 ± 0.4	3048.8 ± 73.5	32.3 ± 0.9
$N_{out} > 0.52$	8813.1 ± 106.4	30.7 ± 0.4	2755.5 ± 71.8	29.2 ± 0.8

Table 6.2: Exclusive yields and efficiencies (in %) for the analysis chain in the Monte Carlo and data samples. The statistical error is added in quadrature with the fit uncertainty.

Requirement	B0B0bar Monte Carlo		Data Runs 1-4	
	Survival	Purity	Survival	Purity
Preselection	100 ± 0	90.62 ± 0.46	100 ± 0	64.38 ± 0.89
$Q_{GTL} = 0$	74.0 ± 0.2	91.85 ± 0.41	72.5 ± 0.4	66.37 ± 1.21
$N_{GTL} = 2$	73.6 ± 0.2	91.92 ± 0.49	71.9 ± 0.4	66.61 ± 1.22
$N_{KML} = 0$	59.0 ± 0.3	92.44 ± 0.55	58.9 ± 0.4	68.15 ± 1.23
$N_{KsD} = 0$	50.3 ± 0.3	92.44 ± 0.55	49.2 ± 0.4	69.86 ± 1.17
$N_{KIET} = 0$	35.4 ± 0.3	93.57 ± 0.53	31.7 ± 0.4	72.49 ± 1.35
$E_{res} < 0.11$ GeV	16.8 ± 0.2	93.82 ± 0.58	<i>blind</i>	<i>blind</i>
$l'l', l\pi, 2\pi, 2\rho$	4.5 ± 0.1	96.49 ± 0.88	<i>blind</i>	<i>blind</i>
$N_{out} > 0.52$	2.79 ± 0.09	96.50 ± 1.14	<i>blind</i>	<i>blind</i>

Table 6.3: Cumulative survival fraction $y_i \equiv N_i/N_0$ and purities p_i (in %) in the data and background samples. The statistical error is added in quadrature with the fit uncertainty. For the unblinded version, see Table 7.4

Requirement	Signal Cocktail		Signal Generic	
	Peak Yield	Efficiency	Peak Yield	Efficiency
Tag B Yield	230574.1 \pm 595.3	100.00 \pm 0.00	1929.5 \pm 60.5	100.00 \pm 0.00
Preselection	69132.2 \pm 282.1	29.98 \pm 0.12	557.5 \pm 26.1	28.89 \pm 1.38
$Q_{GTL} = 0$	62000.0 \pm 264.5	26.89 \pm 0.11	481.6 \pm 23.7	24.96 \pm 1.25
$N_{GTL} = 2$	61864.2 \pm 264.2	26.83 \pm 0.11	480.7 \pm 25.6	24.92 \pm 1.35
$N_{KML} = 0$	55009.4 \pm 251.7	23.86 \pm 0.10	433.9 \pm 22.4	22.49 \pm 1.18
$N_{KsD} = 0$	52067.4 \pm 239.7	22.58 \pm 0.10	412.8 \pm 20.3	21.39 \pm 1.07
$N_{KlET} = 0$	44556.6 \pm 219.7	19.32 \pm 0.09	324.9 \pm 19.4	16.84 \pm 1.02
$E_{res} < 0.11$ GeV	25009.4 \pm 161.0	10.85 \pm 0.07	188.3 \pm 13.7	9.76 \pm 0.71
$ll', l\pi, 2\pi, 2\rho$	12008.6 \pm 109.6	5.21 \pm 0.05	100.4 \pm 10.0	5.20 \pm 0.52
$N_{out} > 0.52$	9991.2 \pm 100.3	4.33 \pm 0.04	80.5 \pm 9.0	4.17 \pm 0.47

Table 6.4: Cumulative yields and efficiencies for the analysis chain in the signal samples. The statistical error is added in quadrature with the fit uncertainty.

Requirement	Signal Cocktail		Signal Generic	
	Peak Yield	Efficiency	Peak Yield	Efficiency
Preselection	69132.2 \pm 282.1	100.0 \pm 0.0	557.5 \pm 26.1	100.0 \pm 0.0
$Q_{GTL} = 0$	62000.0 \pm 264.5	89.7 \pm 0.2	481.6 \pm 23.7	86.4 \pm 2.8
$N_{GTL} = 2$	62992.6 \pm 262.7	91.1 \pm 0.2	493.6 \pm 25.6	88.5 \pm 3.2
$N_{KML} = 0$	61828.5 \pm 272.2	89.4 \pm 0.2	504.1 \pm 24.8	90.4 \pm 3.0
$N_{KsD} = 0$	64869.1 \pm 277.0	93.8 \pm 0.2	517.2 \pm 22.9	92.8 \pm 2.3
$N_{KlET} = 0$	59088.0 \pm 253.2	85.5 \pm 0.2	450.4 \pm 21.3	80.8 \pm 2.4
$E_{res} < 0.11$ GeV	36165.8 \pm 197.5	52.3 \pm 0.2	311.0 \pm 18.3	55.8 \pm 2.6
$ll', l\pi, 2\pi, 2\rho$	36080.7 \pm 196.8	52.2 \pm 0.2	304.1 \pm 18.2	54.6 \pm 2.6
$N_{out} > 0.52$	37439.9 \pm 201.1	54.2 \pm 0.2	288.3 \pm 18.5	51.7 \pm 2.7

Table 6.5: Exclusive yields and efficiencies for the analysis chain in the signal samples. The statistical error is added in quadrature with the fit uncertainty.

Requirement	Signal Cocktail		Signal Generic	
	Survival	Purity	Survival	Purity
Preselection	29.40 \pm 0.09	99.65 \pm 0.15	24.87 \pm 0.91	98.84 \pm 2.03
$Q_{GTL} = 0$	26.34 \pm 0.09	99.76 \pm 0.15	21.52 \pm 0.86	98.69 \pm 1.91
$N_{GTL} = 2$	26.28 \pm 0.09	99.77 \pm 0.14	21.47 \pm 0.86	98.71 \pm 2.75
$N_{KML} = 0$	23.37 \pm 0.09	99.76 \pm 0.17	19.58 \pm 0.83	97.72 \pm 2.00
$N_{KsD} = 0$	22.11 \pm 0.09	99.82 \pm 0.14	18.43 \pm 0.81	98.75 \pm 0.47
$N_{KlET} = 0$	18.91 \pm 0.08	99.87 \pm 0.14	14.55 \pm 0.74	98.47 \pm 2.27
$E_{res} < 0.11$ GeV	10.61 \pm 0.06	99.92 \pm 0.12	8.42 \pm 0.58	98.57 \pm 0.47
$ll', l\pi, 2\pi, 2\rho$	5.09 \pm 0.05	99.98 \pm 0.02	4.45 \pm 0.43	99.40 \pm 0.37
$N_{out} > 0.52$	4.24 \pm 0.04	99.98 \pm 0.08	3.57 \pm 0.39	99.44 \pm 0.38

Table 6.6: Cumulative survival fraction $y_i \equiv N_i/N_0$ and purities p_i in the signal samples. The statistical error is added in quadrature with the fit uncertainty.

generic neutral B and Table 6.5 for signal cocktail and generic samples. The survival fractions y_i and purities p_i are in Tables 6.3 and 6.6.

It will be noted that the signal efficiencies are with respect to the tag B yield, while the data and neutral B efficiencies are with respect to the tag B yield after preselection. See the Appendix for the fits used in obtaining these efficiencies.

The signal efficiency and its error, together with the expected number of background events and its error, will determine the expected upper limit for $B^0 \rightarrow \tau^+ \tau^-$. The expected number of events from background for this analysis is determined by the number of data events remaining after the preselection and the expected efficiency determined from the generic neutral B simulation sample. The background expectation is obtained by multiplying the neutral B simulation efficiency (measured with respect to the yield after preselection) obtained in column two, last row in Table 6.1, by the data yield after preselection obtained in column three, first row in Table 6.1. The error on both efficiency and data yield propagates through to the error on the expected background B .

The signal efficiency obtained from the signal generic sample is $\epsilon_{sig} = 4.17 \pm 0.47\%$. In the data analyzed, assuming the Standard Model branching ratio $B^0 \rightarrow \tau^+ \tau^-$, we expect 0.00037 events. The expected number of background events is $B = 280.9 \pm 11.0$. These errors do not include systematic errors, which are treated in Section 6.3.

6.2. Limit Setting Procedure

We seek an upper limit on the branching ratio R for $B^0 \rightarrow \tau^+ \tau^-$. The number of data events we observe after imposing all requirements in the analysis chain is

$$n = RN_{B^0 \bar{B}^0} \epsilon_{sig} + B \quad (6.6)$$

where $N_{B^0 \bar{B}^0}$ is the tag B yield, ϵ_{sig} is the signal efficiency and B is the expected background. In a single observation of n_{obs} events in data, the determination of R is complicated by the Gaussian fluctuations in $N_{B^0 \bar{B}^0}$, ϵ_{sig} and B as well as the Poisson fluctuation on n .

To obtain the 90% confidence level upper limit R_{ul}^{90} on the branching ratio R , we determine the corresponding upper limit n_{ul}^{90} on the number of observed events

$$n_{ul}^{90} = R_{ul}^{90} N_{B^0 \bar{B}^0} \epsilon_{sig} + B \quad (6.7)$$

where n follows a Poisson distribution. We do so by finding R_{ul}^{90} such that

$$\sum_{n=0}^{n_{obs}} P(n; n_{ul}^{90}) = 0.1 \quad (6.8)$$

where $P(n; n_{ul}^{90})$ is the Poisson distribution with mean n_{ul}^{90} . Equivalently, we seek the branching ratio R such that the fraction of events generated according to the Poisson

distribution with $n \leq n_{obs}$ is only 10%. Once this equation holds for R_{ul}^{90} , we can rule out at the 90% confidence level the hypothesis that $R \geq R_{ul}^{90}$.

We follow the approach taken in [69] and [70] and imagine N_{exp} experiments in which $N_{B^0\bar{B}^0}$, ϵ_{sig} , B and n fluctuate according to their parent distributions. We first fix a low hypothesis R_0 for the branching ratio. Then for each experiment, we sample:

$$\tilde{N}_{B^0\bar{B}^0} \in G(N_{B^0\bar{B}^0}, \delta_{N_{B^0\bar{B}^0}}) \quad (6.9)$$

$$\tilde{\epsilon}_{sig} \in G(\epsilon_{sig}, \delta_{\epsilon_{sig}}) \quad (6.10)$$

$$\tilde{B} \in G(B, \delta_B) \quad (6.11)$$

$$\tilde{n} \in P(R_0 \tilde{N}_{B^0\bar{B}^0} \tilde{\epsilon}_{sig} + \tilde{B}) \quad (6.12)$$

where $G(\mu, \sigma)$ is a Gaussian distribution with mean μ and standard deviation σ , and $P(\mu)$ is a Poisson distribution with mean μ .

After N_{exp} such experiments, the fraction of experiments for which $\tilde{n} \leq n_{obs}$ is calculated. If it is larger than 10%, the hypothesis R_0 is increased and another N_{exp} experiments are carried out. The procedure repeats until the fraction of experiments with $\tilde{n} \leq n_{obs}$ is, to within a small tolerance, 10%.

It should be noted that [70] discusses three different conventions for sampling parameters from parent distributions, distinguished as distinct *prior assumptions*: that of Cousins and Highland, the Babar Statistics Working Group and Jeffries. The prior assumption used here is the natural one of Cousins and Highland [69].

In the prior assumption of Cousins and Highland, all parameters $N_{B^0\bar{B}^0}$, ϵ_{sig} , B , and n_{obs} are allowed to fluctuate according to their parent distributions with their own widths. In contrast, the prior assumptions of the Babar Statistics Working Group and Jeffries assumes that the ratio of two normally distributed parameters is also normally distributed, with a width obtained by combining the widths of the two parent distributions. This allowance is undesirable. Since each prior assumption gives a slightly different result for R_{ul}^{90} , the distinction is important.

6.3. Systematic Errors

Several sources of systematic error affect the four quantities ($N_{B^0\bar{B}^0}$, ϵ_{sig} , B and n_{obs}) which will determine the expected limit on $\mathcal{B}(B^0 \rightarrow \tau^+\tau^-)$. The relative systematic error on the tag B yield is estimated by comparing the tag B yield with a four Argus fit to the yield obtained with the simulation samples. That comparison, made in Section 5.3.3, yields $\delta_{N_{B^0\bar{B}^0}}/N_{B^0\bar{B}^0} = 1.3\%$

Two systematic errors affect all four values: simulation statistical error and fit parameter error. These errors have been discussed in a previous section. Other sources of systematic error affect only the Monte Carlo simulation efficiency ϵ_{sig} and background expectation B : i) particle identification error for e, μ and K^\pm , ii) neutrals energy resolution and scale error, iii) track reconstruction efficiency error and iv) remaining neutral energy error. The systematic errors for reconstructing e, μ and

Systematic Effect	Signal Cocktail	Signal Generic	Signal Max.	B0B0bar
MC Stat and Fit Parameters	1.0	11.2	11.2	3.6
Electron Particle ID	0.4	4.9	4.9	0.6
Muon Particle ID	0.2	7.4	7.4	2.6
Kaon Particle ID	5.4	1.2	5.4	2.3
Photon Energy Resolution	0.8	2.5	2.5	3.0
Signal Decay Model	2.3	2.4	2.4	0.0
Tracking Efficiency	2.6	2.6	2.6	2.6
Remaining Photon Energy	11.5	11.5	11.5	11.5
Total Error	13.3	18.8	19.6	13.2

Table 6.7: Relative systematic errors δ_ϵ/ϵ (in %) for the signal cocktail efficiency, signal generic efficiency and generic neutral B efficiency. Column three indicates the larger of the two signal systematic errors.

K^\pm in the tight electron, tight muon and loose kaon lists are obtained by comparing the efficiencies before and after the `baseClass` killing switches `-pe`, `-pm` and `-pk` were employed and calculating the relative difference in efficiency. These switches use the efficiency tables generated by the particle identification group to adjust the simulation efficiencies using data control sample efficiencies. The lepton tables were generated after imposing a loose kaon veto.

Similarly, the systematic error for neutrals reconstruction was obtained by comparing the efficiencies before and after the switch `-SN` was employed. This switch enables the smearing and scaling of photon energies to match the performance in data control samples. Since we only employ efficiencies relative to the tag B yield in Monte Carlo simulation, the tag side tracks contribute no systematic error. For two signal side tracks, we take the track reconstruction error to be twice the single track systematic error 1.3% recommended by the 2004 Babar tracking task force.

In principle, all background systematic biases have been corrected for with the prescribed simulation corrections. Any deviations from the simulation expectations are, in principle, due to statistical fluctuations. But it is suspected that the modeling of background hits in the EMC probably introduces a systematic bias on the residual neutral energy measured there which has not yet been accounted for.

The systematic error due to the remaining neutral energy we derive from the extra K_S control sample. While the difference between the generic neutral B simulation expectation and data observation could be taken as an estimate of the error due to the generic neutral B remaining neutral energy systematic, a statistical fluctuation in the control sample yield may distort the measure. Noting that simulation and data yields agree well within error, we take a slightly more conservative estimate of the unassigned neutral energy error to be the data control sample yield error (statistical and fit) added in quadrature with the simulation control sample yield error (statistical and fit). We expect this error to be of the same magnitude for the signal simulation efficiency, and so assign the same error to the signal efficiency.

The reason for adopting the error on the control sample yield, rather than the control sample yield discrepancy, is as follows. Since the systematic biases from PID, neutrals and tracking have all been corrected for with the standard prescriptions, we believe that the only remaining nonstatistical reason why the MC control sample should not correctly predict the data control sample yield is the background hit modeling in the EMC, which introduces a bias in the residual neutral energy distribution.

But after noting that the MC and data control sample yields agree very well, we have to acknowledge that a statistical fluctuation may have made the agreement seem artificially good. The uncertainty on the yield gives us a measure of how large the yield discrepancy due to the residual neutral energy modeling might be while allowing for a statistical fluctuation in data or MC or both.

The only way to decouple statistical effects from the measure of the neutral energy bias is to estimate the magnitude of the statistical effects and suppose that, in the worst case scenario, a statistical fluctuation has entirely compensated for the discrepancy due to residual neutral energy bias. In that case, the residual neutral energy bias is of the same magnitude as the statistical fluctuation. It is the worst case scenario assumption which makes our estimate conservative.

A final systematic error affects only the signal efficiency ϵ_{sig} . This signal decay systematic is due to bias in the signal Monte Carlo simulation of the signal B decay to a tau pair. The correlations between tau daughter momenta are used the neural network analysis, and variations between decay models can be estimated. In order to obtain an independent set of ditau decay kinematic parameters, we used the simulation package Tauola [45].

Using Tauola, 10^6 events were generated in which a $\tau^+\tau^-$ pair with opposite helicities and the requisite momentum for ditau B decay. For each signal simulation event, the EvtGen tau daughter momenta are resampled from the Tauola distribution based on true EvtGen tau decay modes. The momenta are boosted from the B frame

back to the detector frame to verify that they are within the detector acceptance. If they are, the tau daughters are boosted back to the B frame with the mass hypotheses assigned by particle identification. Finally, the daughter momenta are smeared by 1.2%, in accord with the momentum resolution in EvtGen and the full detector simulation.

The tau daughter momenta, subtended angle and neural network output distributions for both Tauola and EvtGen are plotted in Figures 5.8 and 5.9. The systematic error on the signal decay simulation is then taken to be the relative difference in efficiencies obtained with the Tauola and EvtGen simulations. See Table 6.7 for the signal decay model systematic error and a complete list of all systematic errors.

The total systematic error on the signal generic efficiency is dominated by statistical error. After all analysis requirements are imposed on the signal generic sample, only 81 events remain. This increases the likelihood that the systematic error estimates are biased by the low statistics effects. The signal cocktail sample, in contrast, contains 9991 events after all analysis chain requirements are imposed, so that low statistics effects are unlikely to bias the systematic error estimate. For these reasons, we include a column in Table 6.7 which assumes the larger of the two signal systematic error estimates for a conservative estimate of the total systematic and statistical uncertainty on the signal efficiency.

In order to study the effect of error on the expected upper limit (see the following section), we varied the errors on the tag B yield, the expected background B and the

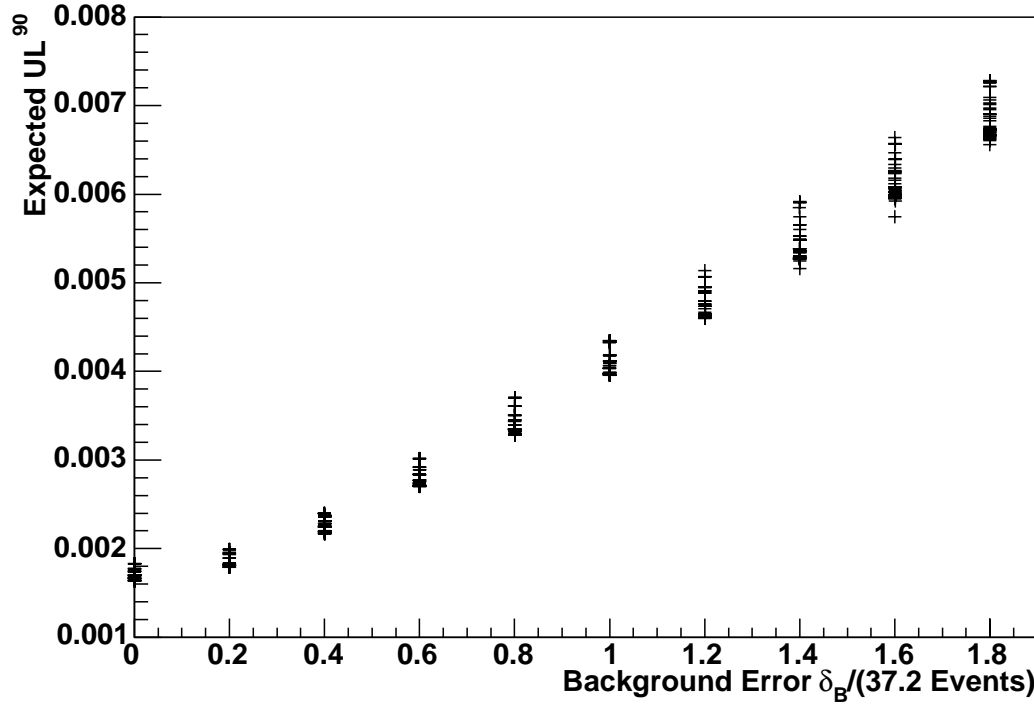


Figure 6.1: The expected 90% upper limit plotted against the error on the background expectation (in units of the nominal error, 37.2 events). Both the tag B yield error and the signal efficiency errors are varied.

signal efficiency error. The errors were varied from zero to nearly twice their nominal values, from zero to 1.5 times the nominal tag B yield error, from zero to 1.8 times the nominal background error and from zero to 1.8 times the nominal signal efficiency error.

See Figure 6.1 for the expected upper limit plotted against the error on the background expectation. The results show that the background error dominates the expected upper limit. The expected upper limit with the nominal errors is 4.0×10^{-3} .

The tag B yield error has negligible impact. The signal efficiency error does not dramatically affect the expected upper limit, decreasing the upper limit only by about 5% when it drops to zero. If the remaining photon energy systematic error is half the nominal value, the overall background error is 0.67 times the nominal overall background error, which yields 3.0×10^{-3} for the expected upper limit. When the total error on the expected background drops to half the nominal value (as it would if the remaining photon energy systematic error was zero), the expected upper limit drops to 2.5×10^{-3} . When all errors are at zero, the expected upper limit is 1.5×10^{-3} .

6.4. Upper Limit Optimization

We chose four analysis chain parameter requirements such that they minimize the upper limit R_{ul}^{90} . The discrete parameters are the tag B purity (which is an ordering of tag B reconstruction modes) and the signal ditau selection modes. The continuous parameters are the neural network output and the unassigned photon energy. These are the only continuous parameters in the analysis, and the expected upper limit varies continuously with their cut values.

The optimization proceeds by requiring a minimal tag B purity and a fixed subset M of the set of signal modes to be reconstructed and sampling each cut value from a uniform distribution on an interval appropriate for the parameter: $[0.1, 0.7]$ for the neural network output N_{out} and $[0.1, 0.5]$ for the upper bound on the unassigned

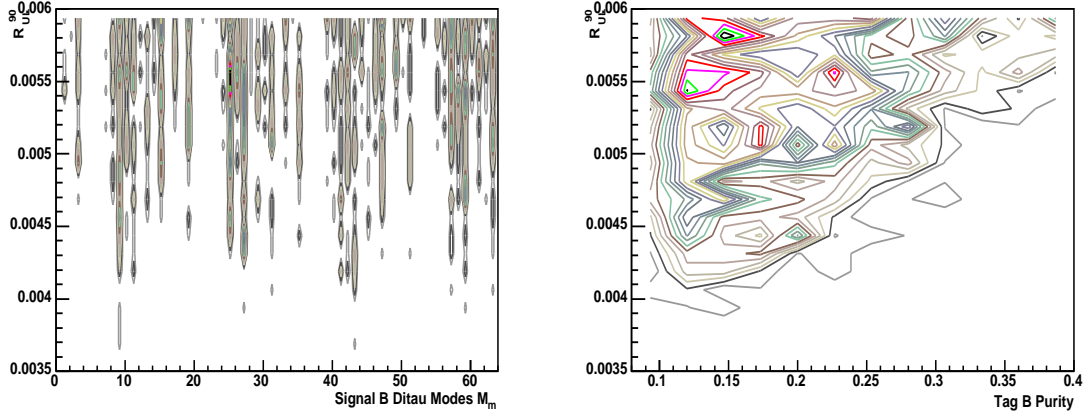


Figure 6.2: Contour plots of the expected 90% confidence level upper limit R_{ul}^{90} plotted versus mode subset number m . Mode subsets $m = 9, 27, 43$ and 59 generate $R_{ul}^{90} < 4 \times 10^{-3}$. The first contours are rejected as marking statistical outliers.

photon energy $E_{GPL} - E_{pDM}$. The systematic errors on the signal efficiency and background expectation for this set of cut values is computed as described in Section 6.3. The systematic error on the tag B yield is independent of the cut values. Assuming that the number of observed data events is equal to the background expectation, the upper limit R_{ul}^{90} is determined as described in Section 6.2. For each set of cut values, the number of trial experiments N_{exp} is 10^4 .

We first optimized the minimal tag B purity and the ditau selection modes. The optimization was over all subsets M of the set of modes $\{ll'4\nu, l\pi3\nu, l\rho3\nu, 2\pi2\nu, \pi\rho2\nu, 2\rho2\nu\}$. In 10^3 choices of random mode subset, both continuous parameters and the purity were allowed to vary randomly. Each mode subset M can be uniquely mapped to an integer m in the range $[0, 63]$ using a binary representation: $m = \sum_{i \in M} 2^i$. See Figure 6.2 for a contour plot of the expected upper limit R_{ul}^{90} against subset representation

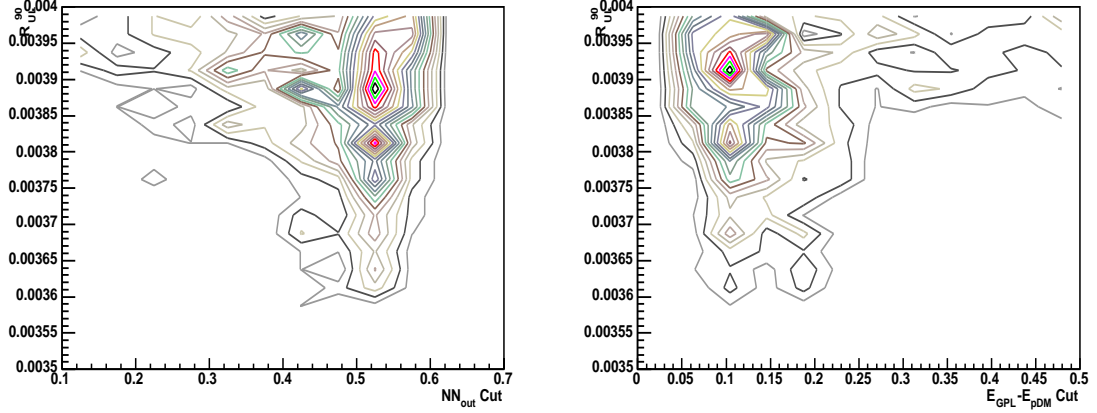


Figure 6.3: Contour plots of the expected 90% confidence level upper limit R_{ul}^{90} plotted versus cut values for lower bound for the neural network output (left) and upper bound for unassigned photon energy (right). The first contours are rejected as marking statistical outliers.

m and a contour plot of the expected upper limit R_{ul}^{90} against minimum tag B purity.

Four signal mode subsets yield $R_{ul}^{90} < 4 \times 10^{-3}$:

$$M_9 = \{ll'4\nu, 2\pi2\nu\} \quad (6.13)$$

$$M_{27} = \{ll'4\nu, l\pi3\nu, 2\pi2\nu, \pi\rho2\nu\} \quad (6.14)$$

$$M_{43} = \{ll'4\nu, l\pi3\nu, 2\pi2\nu, 2\rho2\nu\} \quad (6.15)$$

$$M_{59} = \{ll'4\nu, l\pi3\nu, 2\pi2\nu, \pi\rho2\nu, 2\rho2\nu\}. \quad (6.16)$$

We treat the first contour as marking the extent of statistical outliers and take the next two contours to indicate the optimal cut values. This selects the modes in $M_{43} = \{ll'4\nu, l\pi3\nu, 2\pi2\nu, 2\rho2\nu\}$ and the minimum tag B purity $B_{pur} > 0.12$.

Next, we fixed the mode selection and the minimal tag B purity at the optimal result to include all modes and optimized only over continuous parameters in 10^3 choices for cut values. See Figure 6.3 for plots of the expected upper limit R_{ul}^{90} against E_{res} and N_{out} cut value. Again rejecting the first contour as statistical outliers, the cut values which minimize the upper limit over the sampled set are

$$N_{out} > 0.52 \tag{6.17}$$

$$E_{GPL} - E_{pDM} < 0.11 \tag{6.18}$$

Therefore these values are chosen for the analysis.

Chapter 7

RESULTS

This chapter presents the results of the analysis for $B^0 \rightarrow \tau^+\tau^-$ described in Chapters 5 and 6. The chapter begins by identifying the tag B yield, expected background and the signal efficiency together with the estimated systematic errors on these quantities. The unblinded data yield, which determines the upper limit on the branching ratio for $B^0 \rightarrow \tau^+\tau^-$, is then presented. The unblinded neural network input and output distributions after the full selection are shown. The chapter concludes by drawing out the implications of the established upper limit for the theoretical models described in Chapter 2 and reflecting on how a better measurement of this rare decay can be made.

7.1. Blinded Expectation and Unblinded Results

The upper limit is established using the observed number of events in the signal region after unblinding, the tag B yield and its error, the signal efficiency and its error and the expected background and its error. Systematic errors are taken from Table 6.7. The background expectation is obtained from the data preselection yield and the background efficiency from Table 6.1. The background error is the error reported in

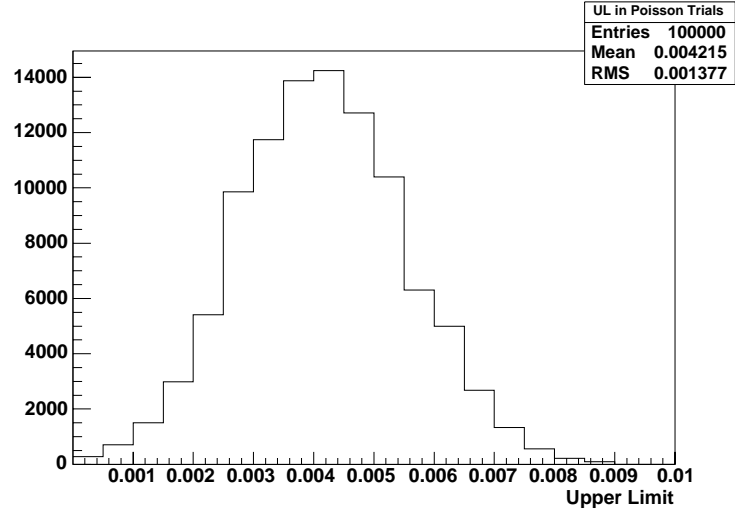


Figure 7.1: The distribution of the 90% confidence level upper limit in 10^5 Poisson trials with mean 281 assuming zero signal events.

Table 6.7, but with the relative error on the data preselection yield from Table 6.1 added in quadrature. The signal efficiency is obtained from Table 6.4.

The cut values obtained after optimization for best upper limit determine the latter three to be:

$$N_{B^0 \bar{B}^0} = 3.13 \times 10^5 \times (1 \pm 0.013) \quad (7.1)$$

$$\epsilon_{sig} = 0.0417 \times (1 \pm 0.196) \quad (7.2)$$

$$B = 280.9 \times (1 \pm 0.132 \oplus 0.012). \quad (7.3)$$

The two errors in the expression for B are the systematic error and the error on the data preselection yield. Using the limit setting procedure described in Section 6.2, we find the upper limit determined by a set of possible outcomes for the number of

n_{obs}	R_{ul}^{90}	n_{obs}	R_{ul}^{90}	n_{obs}	R_{ul}^{90}	n_{obs}	R_{ul}^{90}
230	0.00016	257	0.0022	284	0.0045	311	0.0067
231	0.00024	258	0.0023	285	0.0045	312	0.0068
232	0.00032	259	0.0024	286	0.0046	313	0.0069
233	0.00035	260	0.0025	287	0.0047	314	0.007
234	0.00042	261	0.0026	288	0.0048	315	0.0071
235	0.00048	262	0.0026	289	0.0048	316	0.0072
236	0.00056	263	0.0027	290	0.005	317	0.0072
237	0.00064	264	0.0028	291	0.005	318	0.0073
238	0.0007	265	0.0029	292	0.0051	319	0.0074
239	0.00081	266	0.003	293	0.0052	320	0.0075
240	0.00089	267	0.003	294	0.0053	321	0.0076
241	0.00098	268	0.0031	295	0.0054	322	0.0077
242	0.001	269	0.0032	296	0.0055	323	0.0078
243	0.0011	270	0.0033	297	0.0055	324	0.0079
244	0.0012	271	0.0034	298	0.0056	325	0.0079
245	0.0013	272	0.0035	299	0.0057	326	0.008
246	0.0014	273	0.0035	300	0.0058	327	0.0081
247	0.0014	274	0.0036	301	0.0059	328	0.0082
248	0.0015	275	0.0037	302	0.0059	329	0.0083
249	0.0016	276	0.0038	303	0.0061	330	0.0084
250	0.0017	277	0.0039	304	0.0061	331	0.0085
251	0.0018	278	0.0039	305	0.0062	332	0.0086
252	0.0018	279	0.004	306	0.0063	333	0.0086
253	0.0019	280	0.0041	307	0.0064	334	0.0087
254	0.002	281	0.0042	308	0.0065	335	0.0088
255	0.0021	282	0.0043	309	0.0066	336	0.0089
256	0.0021	283	0.0044	310	0.0066	337	0.009
$N_{B^0\bar{B}^0} = 313480 \pm 3961, \epsilon_{sig} = 0.0417 \pm 0.0082, B = 280.9 \pm 37.2$							

Table 7.1: The upper limit R_{ul}^{90} for a 99.7% coverage range of outcomes n_{obs} . The number of trial experiments for each result is 10^5 . The background expectation is obtained from the data preselection yield and the background efficiency from Table 6.1. The signal efficiency is obtained from Table 6.4. Systematic errors, which include simulation sample statistical error, are taken from Table 6.7.

data events observed after the full signal selection (n_{obs}). See Table 7.1 for the upper limits R_{ul}^{90} determined by n_{obs} and the values above. The summed Poisson probability for the range of n_{obs} in the table is 99.7%, omitting only 0.3% of possible outcomes.

We found the distribution of the upper limit in 10^5 Poisson trials assuming zero signal events in the sample. The background is sampled from a Poisson distribution with mean 281. See Figure 7.1. The distribution indicates that if there are no signal events in the data, it is highly unlikely to obtain an upper limit higher than 7.5×10^{-3} or lower than 1.0×10^{-3} .

When we unblind the analysis, we observe $n_{obs} = 262.6$ data events in the signal region. Using the established procedure from Table 7.1, this yields the result

$$\mathcal{B}(B^0 \rightarrow \tau^+ \tau^-) < 2.7 \times 10^{-3} \quad (7.4)$$

at the 90% confidence level. The result is consistent with a downward fluctuation by 1.1 standard deviations of the expected Standard Model background. See Table 7.2 for the expected background and the observed number of events by mode. See Table 7.3 for the unblinded efficiency table and Figures 7.2 and 7.3 for the unblinded plots.

7.2. Implications for Theoretical Models

Several theoretical models of particle physics, and the implications for $B^0 \rightarrow \tau^+ \tau^-$ in each, were described in Chapter 2. Since no evidence for signal events was observed,

Signal Mode	Signal Efficiency	Expected Background	Observed Events
$l'l'4\nu$	0.88 ± 0.21	45.8 ± 3.9	53.7 ± 7.3
$l\pi 3\nu$	1.49 ± 0.28	122.1 ± 6.4	105.1 ± 11.0
$2\pi 2\nu$	1.47 ± 0.28	88.6 ± 5.5	79.8 ± 10.5
$2\rho 2\nu$	0.29 ± 0.13	21.0 ± 2.9	15.1 ± 5.7

Table 7.2: The signal efficiency, expected background and observed number of events by signal mode. The errors are statistical and fit error added in quadrature. The systematic errors are not included.

Requirement	B0B0bar Monte Carlo		Data Runs 1-4	
	Peak Yield	Efficiency	Peak Yield	Efficiency
Preselection	28662.8 ± 217.6	100.00 ± 0.00	9448.3 ± 151.9	100.00 ± 0.00
$Q_{GTL} = 0$	21497.7 ± 169.8	75.00 ± 0.57	7062.8 ± 146.3	74.75 ± 1.75
$N_{GTL} = 2$	21384.2 ± 180.1	74.61 ± 0.60	7024.6 ± 145.3	74.35 ± 1.74
$N_{KML} = 0$	17235.5 ± 162.3	60.13 ± 0.55	5888.6 ± 123.9	62.32 ± 1.48
$N_{KsD} = 0$	14701.9 ± 146.0	51.29 ± 0.49	5046.2 ± 103.1	53.41 ± 1.24
$N_{KIET} = 0$	10471.9 ± 115.1	36.53 ± 0.39	3371.6 ± 80.0	35.69 ± 0.93
$E_{res} < 0.11$ GeV	4974.1 ± 74.9	17.35 ± 0.26	1474.8 ± 42.9	15.61 ± 0.49
$l'l', l\pi, 2\pi, 2\rho$	1372.1 ± 38.5	4.79 ± 0.13	402.7 ± 21.7	4.26 ± 0.23
$N_{out} > 0.52$	852.1 ± 30.4	2.97 ± 0.11	262.6 ± 18.9	2.78 ± 0.20

Table 7.3: Unblinded cumulative yields and efficiencies (in %) for the analysis chain in the Monte Carlo and data samples. E_{res} is the residual neutral energy $E_{GPL} - E_{pDM}$. The statistical error is added in quadrature with the fit uncertainty. The systematic errors are not included. Note in particular that the $3\sigma^{stat+fit}$ discrepancy after applying the residual energy requirement is well below $1\sigma^{stat+syst}$.

Requirement	B0B0bar Monte Carlo		Data Runs 1-4	
	Peak Yield	Efficiency	Peak Yield	Efficiency
Preselection	100.0 ± 0.0	90.62 ± 0.46	100.0 ± 0.0	64.38 ± 0.89
$Q_{GTL} = 0$	74.0 ± 0.2	91.85 ± 0.41	72.5 ± 0.4	66.37 ± 1.21
$N_{GTL} = 2$	73.6 ± 0.2	91.92 ± 0.49	71.9 ± 0.4	66.61 ± 1.22
$N_{KML} = 0$	59.0 ± 0.3	92.44 ± 0.55	58.9 ± 0.4	68.15 ± 1.23
$N_{KsD} = 0$	50.3 ± 0.3	92.44 ± 0.55	49.2 ± 0.4	69.86 ± 1.17
$N_{KIET} = 0$	35.4 ± 0.3	93.57 ± 0.53	31.7 ± 0.4	72.49 ± 1.35
$E_{res} < 0.11$ GeV	16.8 ± 0.2	93.82 ± 0.58	13.7 ± 0.3	73.16 ± 1.37
$l'l', l\pi, 2\pi, 2\rho$	4.5 ± 0.1	96.49 ± 0.88	3.3 ± 0.1	83.04 ± 2.41
$N_{out} > 0.52$	2.8 ± 0.1	96.50 ± 1.14	2.1 ± 0.1	83.63 ± 3.74

Table 7.4: Unblinded survival fraction $y_i \equiv N_i/N_0$ and purities p_i (in %) for the analysis chain in the Monte Carlo and data samples. E_{res} is the residual neutral energy $E_{GPL} - E_{pDM}$. The statistical error is added in quadrature with the fit uncertainty. The systematic errors are not included.

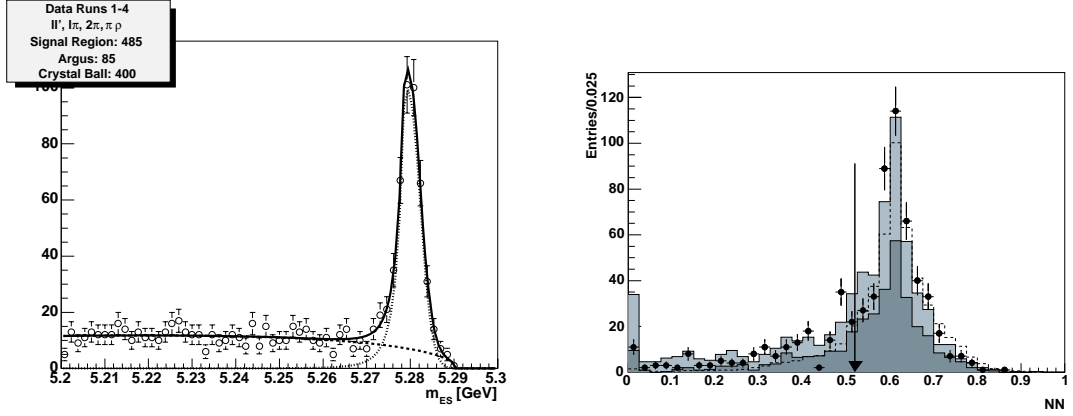


Figure 7.2: The selection for $B \rightarrow \tau^+ \tau^-$. At left, the m_{ES} distribution in Monte Carlo simulation. At right, the neural network output in Monte Carlo simulation. Only the *peaking components* of generic neutral B (solid) and the signal cocktail (dashed) are plotted. The mode selection has not been applied at right.

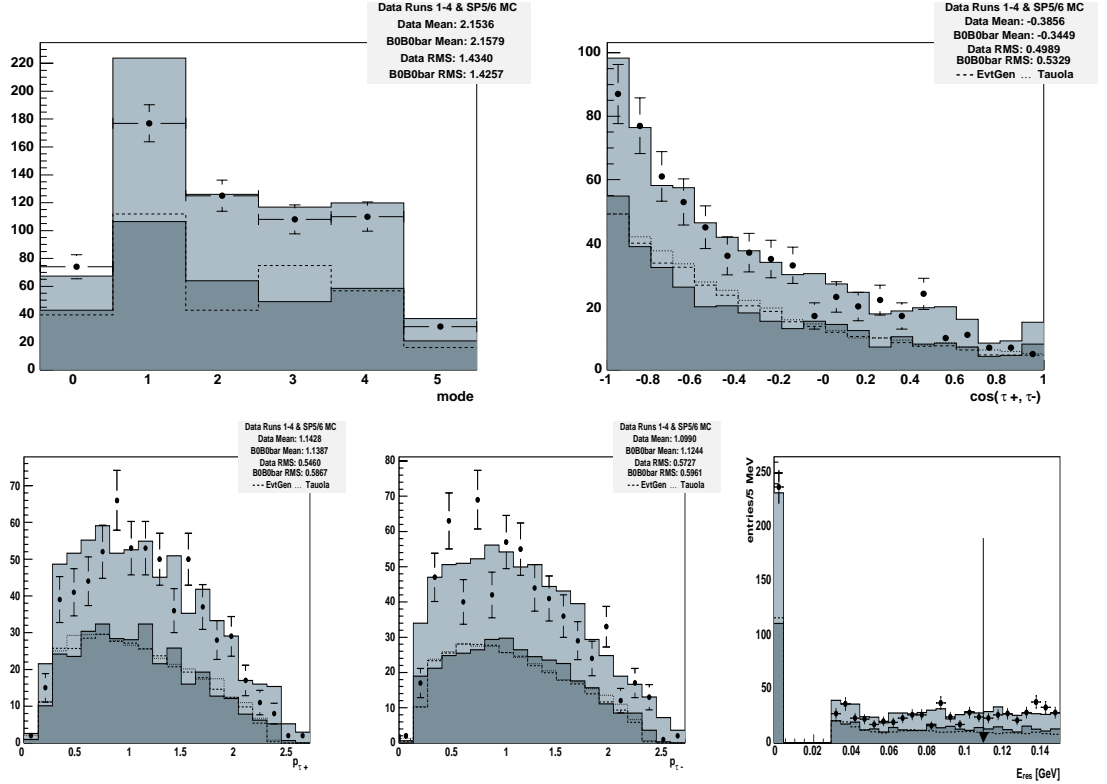


Figure 7.3: Inputs to the neural network for the $B \rightarrow \tau^+ \tau^-$ selection. Clockwise from top left are the signal multiplicity mode, cosine subtended by tau daughter candidate momenta, remaining neutral energy and magnitude of the tau daughter candidate momentum. Only the *peaking components* of data (dots), generic neutral B (solid) and the signal cocktail (dashed) are plotted.

the measured branching ratio cannot be compared with the expectation in various models. However, the upper limit on $\mathcal{B}(B^0 \rightarrow \tau^+ \tau^-)$ does have implications for the free parameters in each model.

In the 2HDM and MSSM, the results place constraints on $\tan \beta$ and m_{H^+} . For the MSSM these constraints are multidimensional constraints involving the chargino and stop masses. The constraints from $\mathcal{B}(B^0 \rightarrow \tau^+ \tau^-)$ are, however, redundant due to the much better limit on $\mathcal{B}(B^0 \rightarrow \mu^+ \mu^-)$ obtained at Babar. In order for the $B^0 \rightarrow \tau^+ \tau^-$ measurement to provide tighter constraints on the parameter space of these models, an upper limit of at least $(m_\tau/m_\mu)^2 \times \mathcal{B}^{UL}(B^0 \rightarrow \mu^+ \mu^-) \approx 2.4 \times 10^{-5}$ would have been required. See Figure 7.4 for the excluded region of the $\tan \beta - m_{H^+}$ plane obtained from the upper limits on both $\mathcal{B}(B^0 \rightarrow \mu^+ \mu^-)$ and $\mathcal{B}(B^0 \rightarrow \tau^+ \tau^-)$.

In leptoquark models the constraints are not redundant since the couplings from third generation leptons to third generation quarks are here, for the first time, measured in a process accessible to experiment. Using Equation 2.67, we obtain

$$\lambda_{31L}^{V_0} \lambda_{33R}^{V_0}, \lambda_{31R}^{V_0} \lambda_{33L}^{V_0} < 1.3 \times 10^{-3} \left[\frac{m_{LQ}}{100 \text{ GeV}} \right]^2 \quad (7.5)$$

$$\lambda_{31R}^{S_{1/2}} \lambda_{33R}^{S_{1/2}}, \lambda_{31R}^{\tilde{S}_0} \lambda_{33R}^{\tilde{S}_0} < 9.8 \times 10^{-3} \left[\frac{m_{LQ}}{100 \text{ GeV}} \right]^2 \quad (7.6)$$

$$\lambda_{31R}^{V_0} \lambda_{33R}^{V_0}, \lambda_{31L}^{V_0} \lambda_{33L}^{V_0}, \lambda_{31R}^{V_{1/2}} \lambda_{33R}^{V_{1/2}} < 1.3 \times 10^{-3} \left[\frac{m_{LQ}}{100 \text{ GeV}} \right]^2 \quad (7.7)$$

at the 90% confidence level. See Figure 7.5 for the excluded regions in the $m_{LQ} - \lambda_{31}^{LQ} \lambda_{33}^{LQ}$ plane.

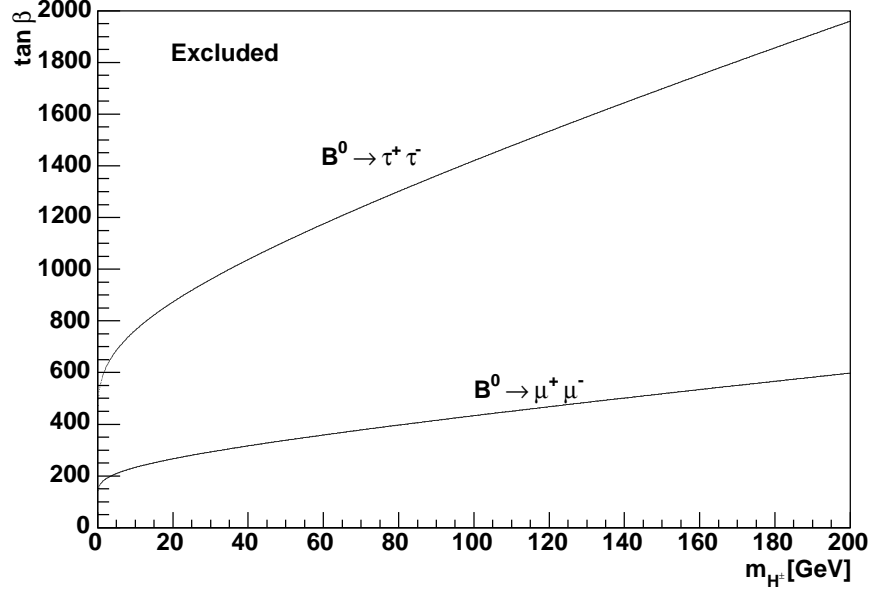


Figure 7.4: The regions of the $\tan \beta - m_{H^+}$ plane which are excluded at the 90% confidence level by the upper limit measurements on $\mathcal{B}(B^0 \rightarrow \mu^+ \mu^-)$ and $\mathcal{B}(B^0 \rightarrow \tau^+ \tau^-)$.

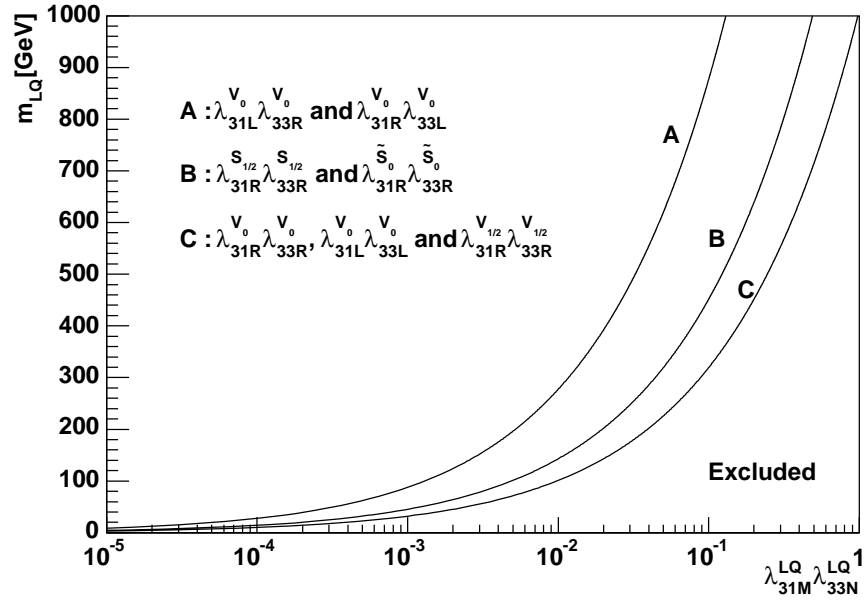


Figure 7.5: The regions of the $m_{LQ} - \lambda_{31}^{LQ} \lambda_{33}^{LQ}$ plane which are excluded at the 90% confidence level by the upper limit measurements on $\mathcal{B}(B^0 \rightarrow \tau^+ \tau^-)$.

7.3. Conclusion

The measurement made in this dissertation provides the first limit on a helicity- and FCNC-suppressed rare decay of a third generation pseudoscalar meson to a lepton pair from the third generation: $\mathcal{B}(B^0 \rightarrow \tau^+ \tau^-) < 2.7 \times 10^{-3}$ at the 90% confidence level. The measurement gives the first constraints on leptoquark couplings to quarks and leptons in the third generation. If the leptoquark mass scale is light, around 100 GeV, the geometric means of leptoquark couplings are constrained to be less than 0.1 when the natural coupling is order 1.

Some small improvement on the upper limit might be made at Babar. With greater luminosity, the error on the control sample discrepancy will be reduced. Thus the systematic error on the residual photon energy will also be reduced. The effect will be to lower the upper limit until the error on the discrepancy becomes smaller than the discrepancy itself or the discrepancy is zero.

In order to provide a substantially better upper limit on $B^0 \rightarrow \tau^+ \tau^-$, the two dominant backgrounds must be reduced. For the K_L background, either a more efficient K_L detector or a detector large enough to measure the K_L decay products are required. For the background due to lost particles in the forward region, either a detector with no boost or instrumentation in the boost direction are required. An alternative would require a more precise vertex detector to measure the tau lifetime in order to separate signal events from background events.

APPENDIX A

DISTRIBUTIONS BEFORE AND AFTER PRESELECTION

The purpose of this appendix is twofold. It first serves to compare observable parameter distributions (in data and simulation) before and after the preselection is imposed. Secondly, it serves to compare the observable parameter distributions after preselection in SP5 and Runs 1-3 data to SP6 and Run 4 data. These plots show unambiguously that there is no dramatic difference in the simulation performance between SP5 and SP6, though the improvement in tight muon multiplicity (Figure A.24) in SP6 is notable.

The preselection requires two very loose tracks and four or fewer loose photons on the signal side. In the observable parameters which are of interest to this analysis (loose photon energy, default neutral pion multiplicity and energy, good track charge, lepton multiplicities) a distinct improvement in the agreement between data and simulation is observed after imposing the preselection. This is both the motivation and justification for the preselection. In other parameters little or no improvement is observed after applying the preselection.

It should be emphasized that the preselection simulation histograms are normalized to the data tag yield after preselection, so the data and simulation are expected to match perfectly in the very loose track multiplicity distribution (Figure 5.5).

The procedure for obtaining these plots was outlined in Section 5.3.2 and is repeated below. From Section 5.3.2:

In order to compare data with Monte Carlo simulation in the parameters used in the analysis chain described in this note, each parameter range is subdivided and m_{ES} fits are performed on the events which lie within that subrange. For purposes of plotting, the ranges of the parameters of the analysis chain are divided into subranges, each of which corresponds to one bin in the parameter plot. With these *bin-by-bin* fits, we are able to compare only the central peaking components between data and Monte Carlo simulation. The aim is to obtain simulation efficiency (of peaking components) on a bin-by-bin basis, then to multiply this single bin efficiency by the total data tag yield. The signal region purity p is determined by the ratio of the area in the Crystal Ball to the area of the overall fitting function on the interval $[5.27, 5.29]$ GeV:

$$p = \frac{\int_{5.27}^{5.29} dm c_x X(m; \sigma, m_0, \alpha, n)}{\int_{5.27}^{5.29} dm F(m; a, m_c, \sigma_i, m_i)} \quad (\text{A.1})$$

The peak yield is then taken to be pN , the purity times the total number of events N in the signal region $m_{ES} \in [5.27, 5.29]$ GeV. All generic neutral B Monte Carlo simulation histograms are normalized to the data tag yield after preselection (described in the following section), except for those to which the analysis is still blind, in which case the histograms are unnormalized. Signal samples are normalized to half the generic neutral B normalization.

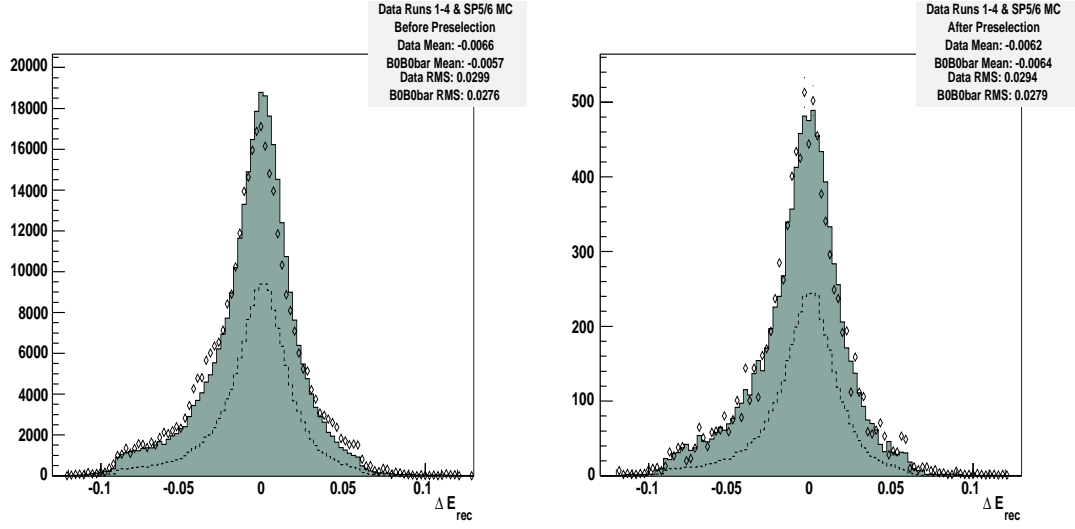


Figure A.1: Tag B ΔE before (left) and after (right) preselection. Only the *peaking components* of data (error bars) and generic neutral B (solid) and signal cocktail (dashed) have been plotted.

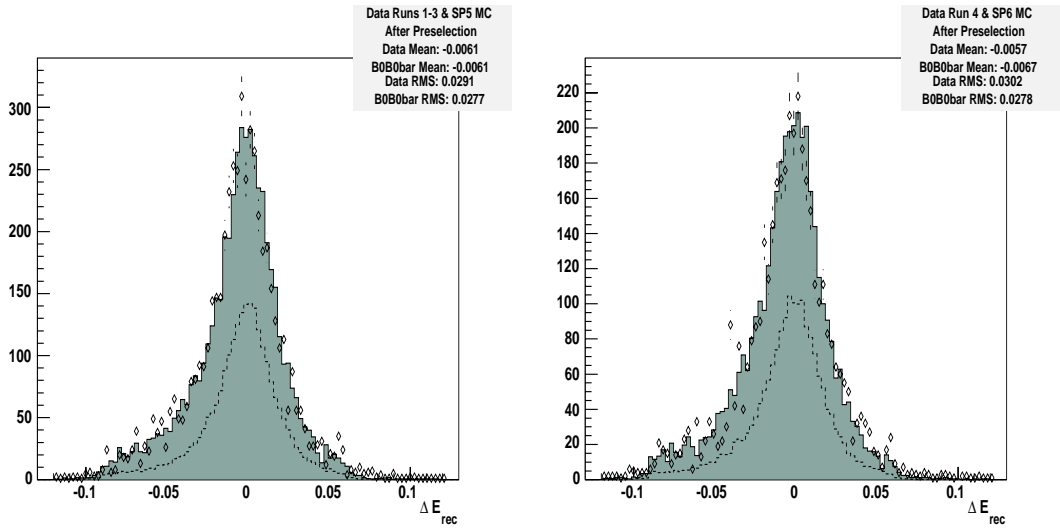


Figure A.2: Tag B ΔE after preselection for Runs 1-3 (left) and Run 4 (right). Only the *peaking components* of data (error bars) and generic neutral B (solid) and signal cocktail (dashed) have been plotted.

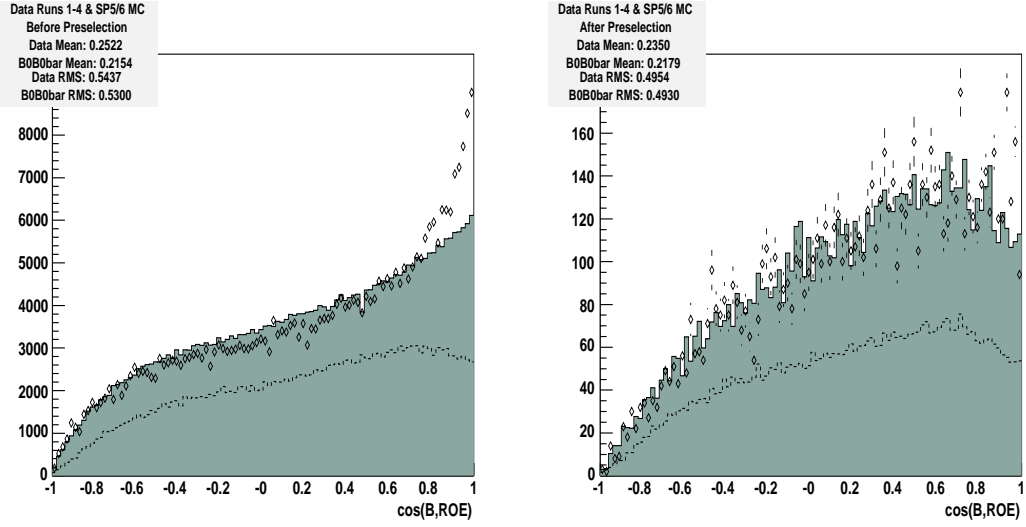


Figure A.3: The cosine of the angle between the tag B and the rest of the event before (left) and after (right) preselection. Only the *peaking components* of data (error bars) and generic neutral B (solid) and signal cocktail (dashed) have been plotted.

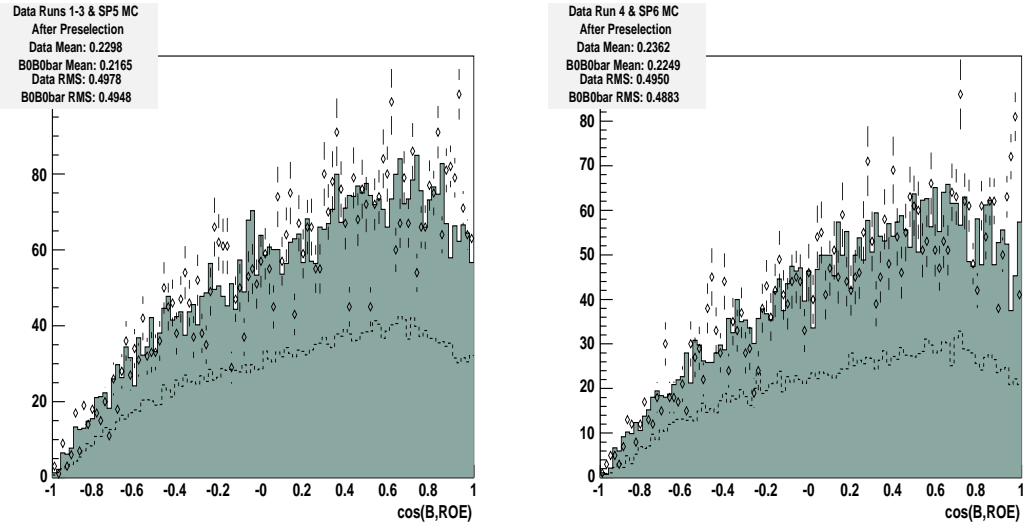


Figure A.4: The cosine of the angle between the tag B and the rest of the event after preselection for Runs 1-3 (left) and Run 4 (right). Only the *peaking components* of data (error bars) and generic neutral B (solid) and signal cocktail (dashed) have been plotted.

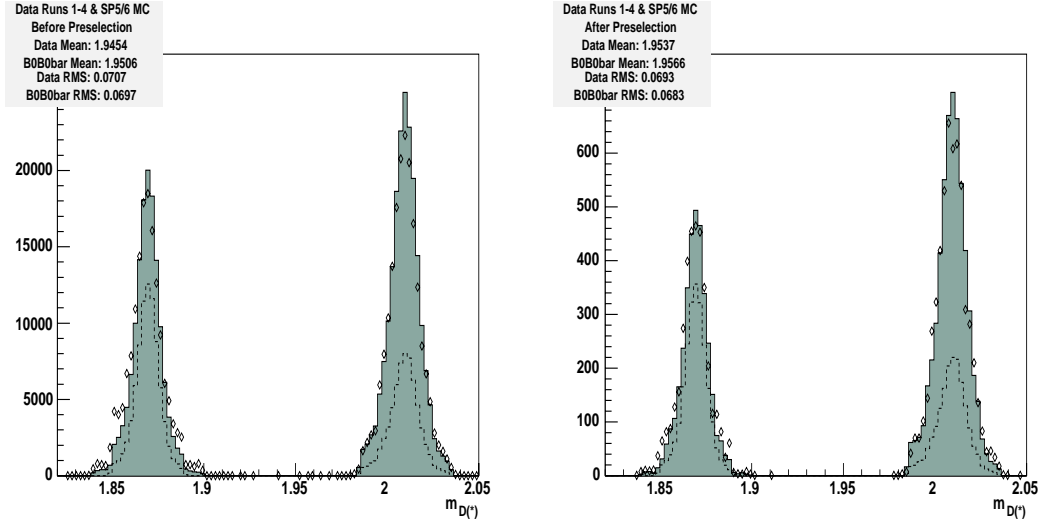


Figure A.5: The mass of the D or D^* used for reconstructing the tag B before (left) and after (right) preselection. Only the *peaking components* of data (error bars) and generic neutral B (solid) and signal cocktail (dashed) have been plotted.

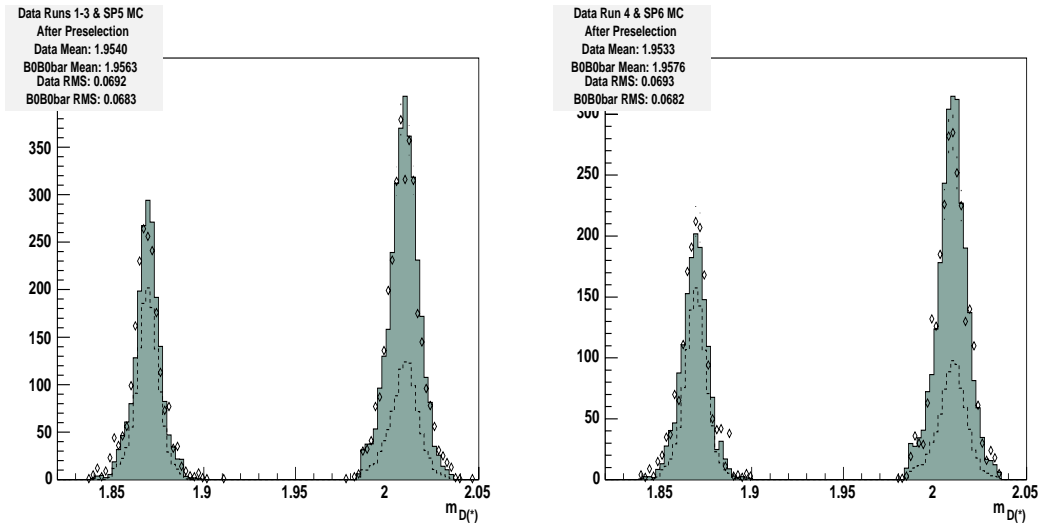


Figure A.6: The mass of the D or D^* used for reconstructing the tag B after preselection for Runs 1-3 (left) and Run 4 (right). Only the *peaking components* of data (error bars) and generic neutral B (solid) and signal cocktail (dashed) have been plotted.

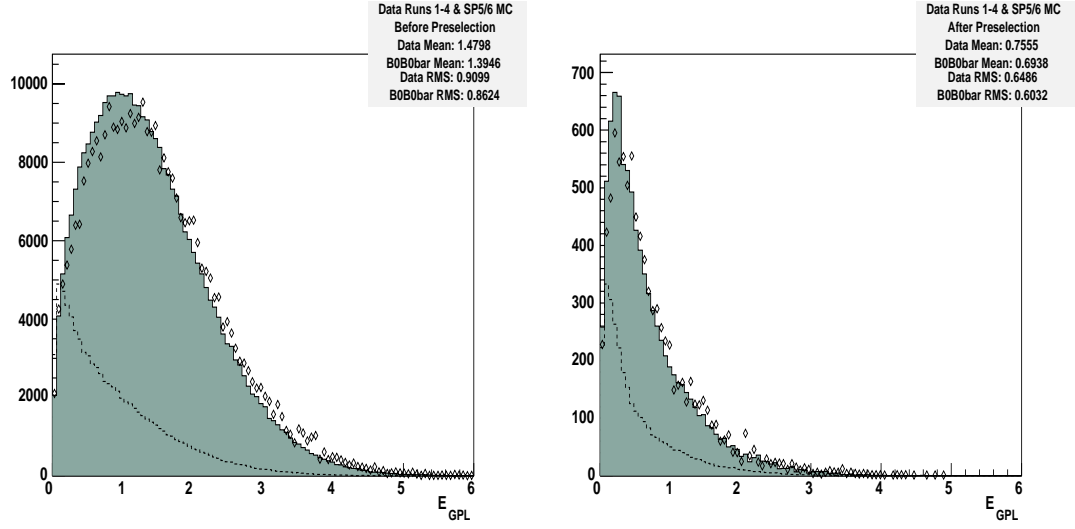


Figure A.7: The signal side energy in all `GoodPhotonsLoose` candidates before (left) and after (right) preselection. Only the *peaking components* of data (error bars) and generic neutral B (solid) and signal cocktail (dashed) have been plotted.

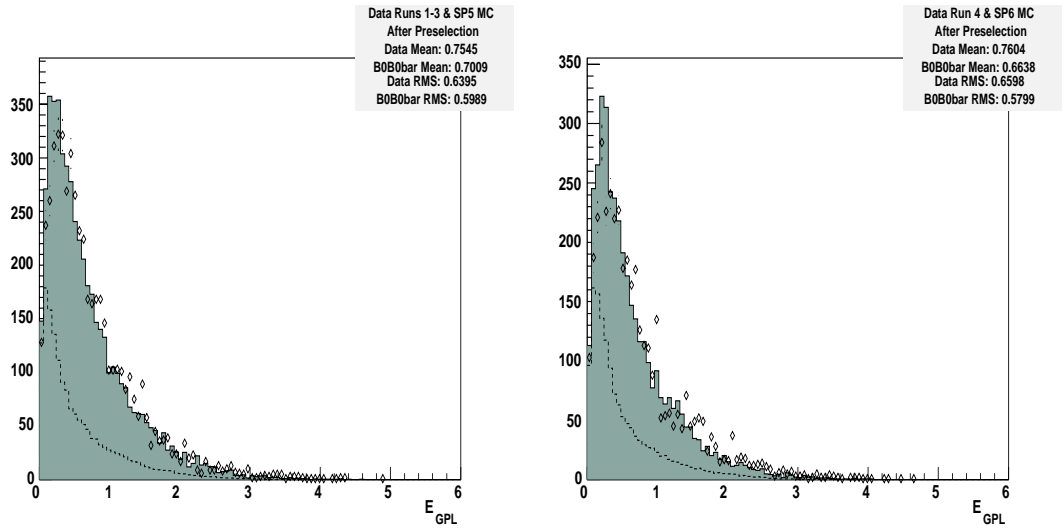


Figure A.8: The signal side energy in all `GoodPhotonsLoose` candidates after preselection for Runs 1-3 (left) and Run 4 (right). Only the *peaking components* of data (error bars) and generic neutral B (solid) and signal cocktail (dashed) have been plotted.

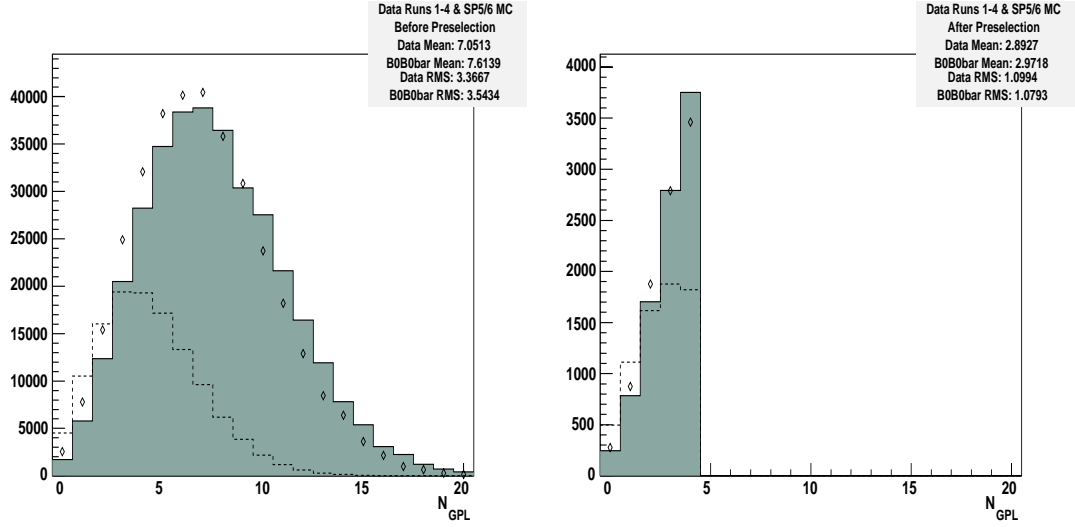


Figure A.9: The signal side `GoodPhotonsLoose` multiplicity before (left) and after (right) preselection. Only the *peaking components* of data (error bars) and generic neutral B (solid) and signal cocktail (dashed) have been plotted.

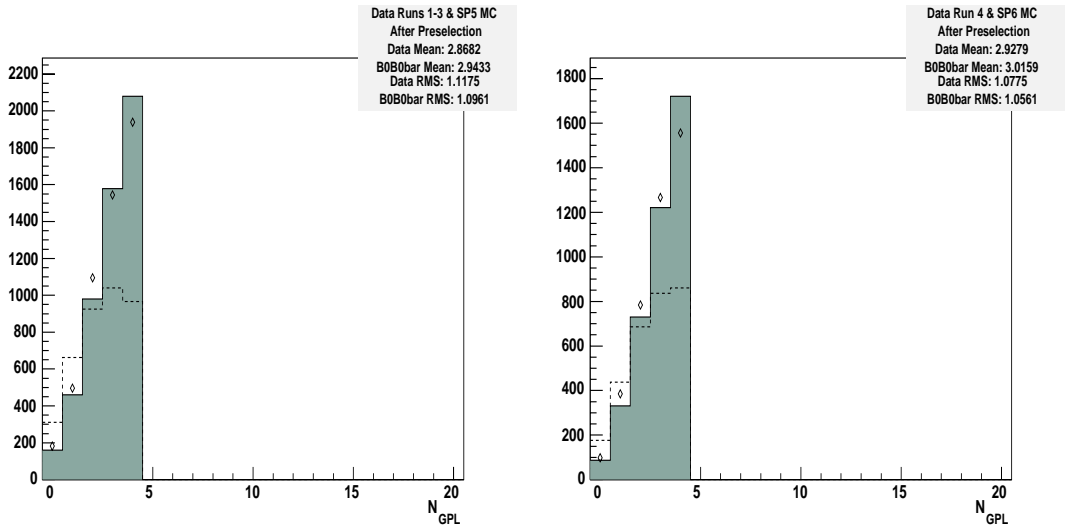


Figure A.10: The signal side `GoodPhotonsLoose` multiplicity after preselection for Runs 1-3 (left) and Run 4 (right). Only the *peaking components* of data (error bars) and generic neutral B (solid) and signal cocktail (dashed) have been plotted.

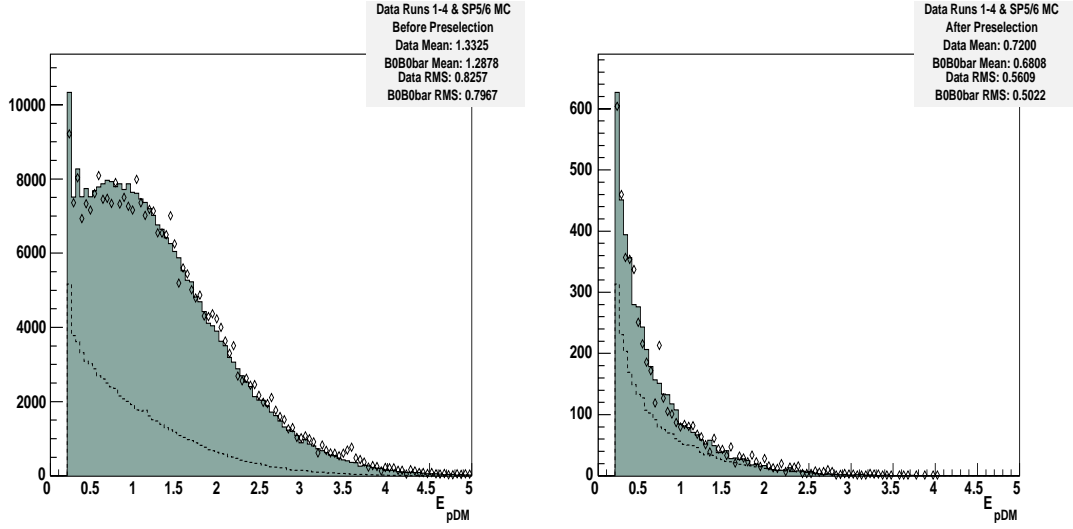


Figure A.11: The signal side energy in the π^0 DefaultMass candidates before (left) and after (right) preselection. Only the *peaking components* of data (error bars) and generic neutral B (solid) and signal cocktail (dashed) have been plotted.

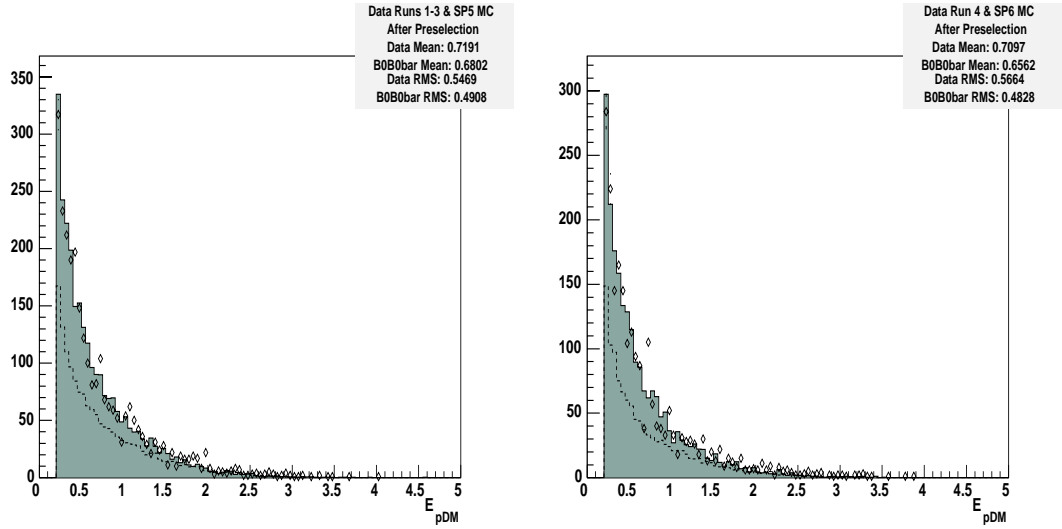


Figure A.12: The signal side energy in the π^0 DefaultMass candidates after preselection for Runs 1-3 (left) and Run 4 (right). Only the *peaking components* of data (error bars) and generic neutral B (solid) and signal cocktail (dashed) have been plotted.

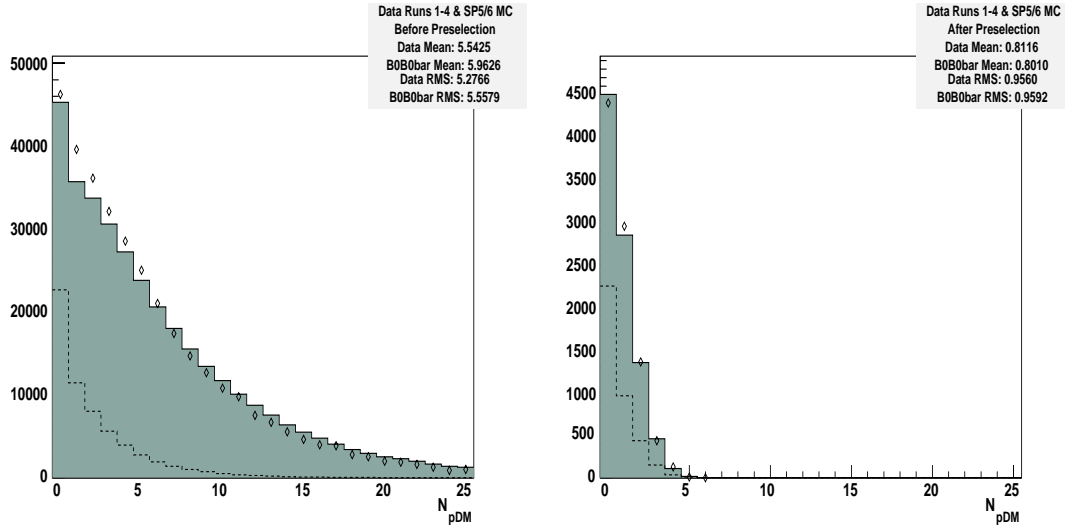


Figure A.13: The signal side π^0 DefaultMass multiplicity before (left) and after (right) preselection. Only the *peaking components* of data (error bars) and generic neutral B (solid) and signal cocktail (dashed) have been plotted.

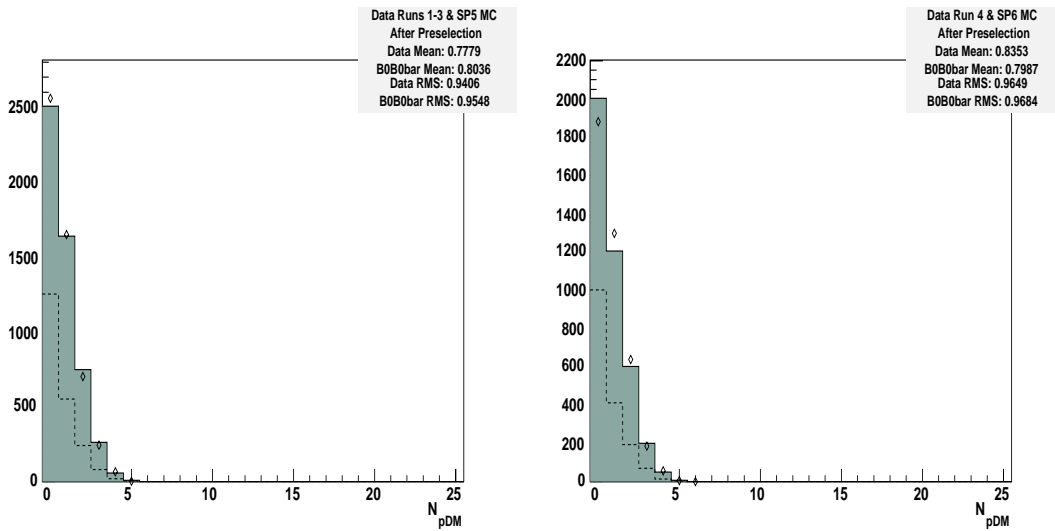


Figure A.14: The signal side π^0 DefaultMass multiplicity after preselection for Runs 1-3 (left) and Run 4 (right). Only the *peaking components* of data (error bars) and generic neutral B (solid) and signal cocktail (dashed) have been plotted.

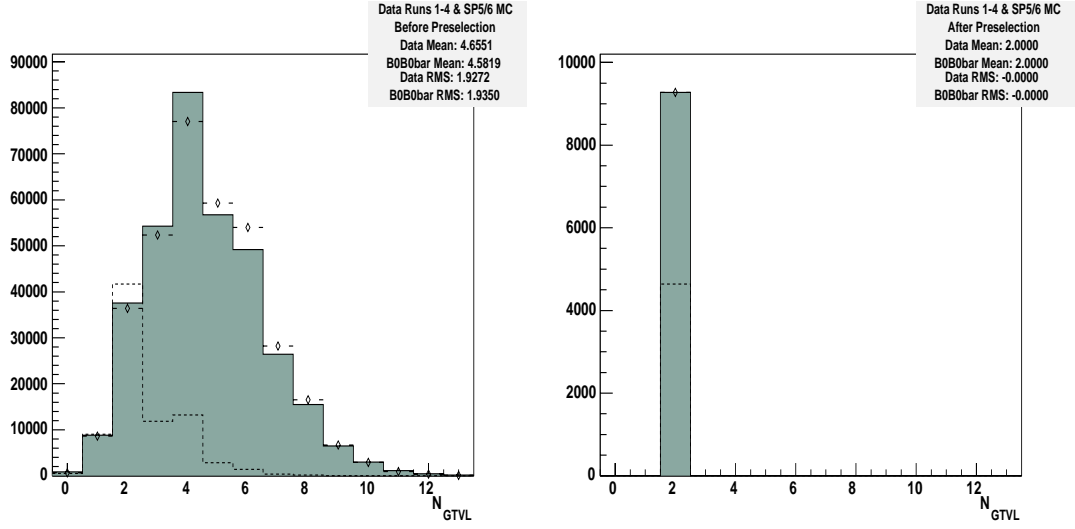


Figure A.15: The signal side `GoodTracksVeryLoose` multiplicity before (left) and after (right) preselection. Only the *peaking components* of data (error bars) and generic neutral B (solid) and signal cocktail (dashed) have been plotted.

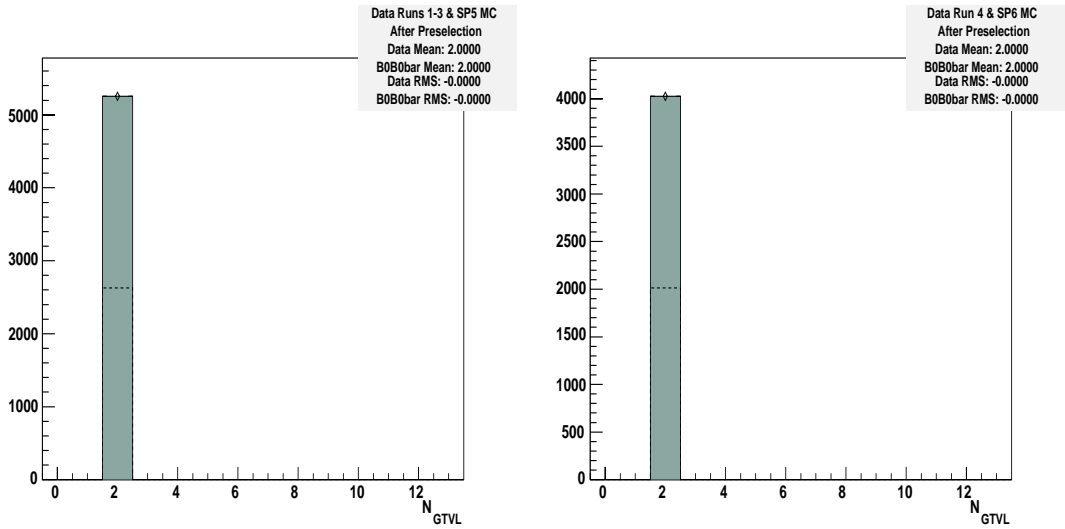


Figure A.16: The signal side `GoodTracksVeryLoose` multiplicity after preselection for Runs 1-3 (left) and Run 4 (right). Only the *peaking components* of data (error bars) and generic neutral B (solid) and signal cocktail (dashed) have been plotted.

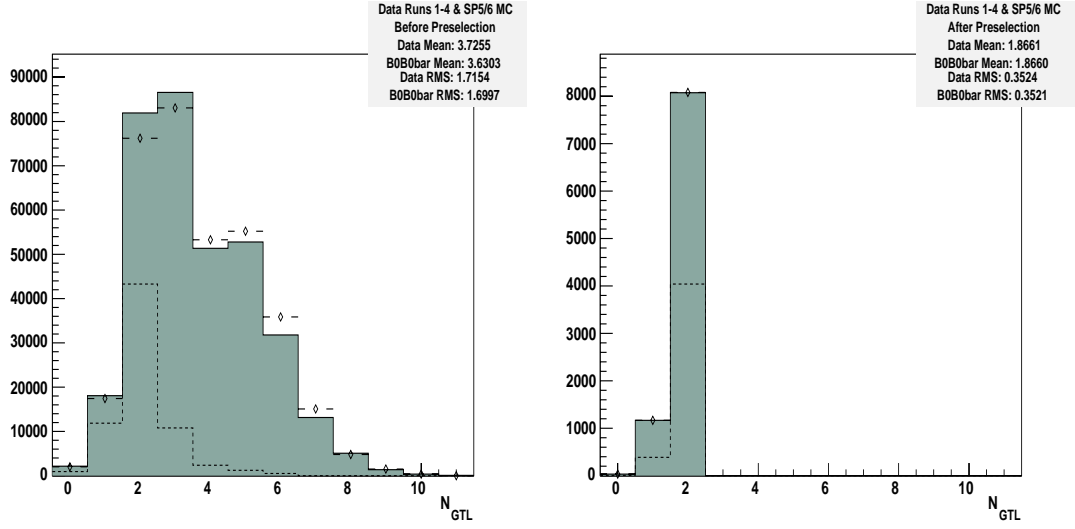


Figure A.17: The signal side `GoodTracksLoose` multiplicity before (left) and after (right) preselection. Only the *peaking components* of data (error bars) and generic neutral B (solid) and signal cocktail (dashed) have been plotted.

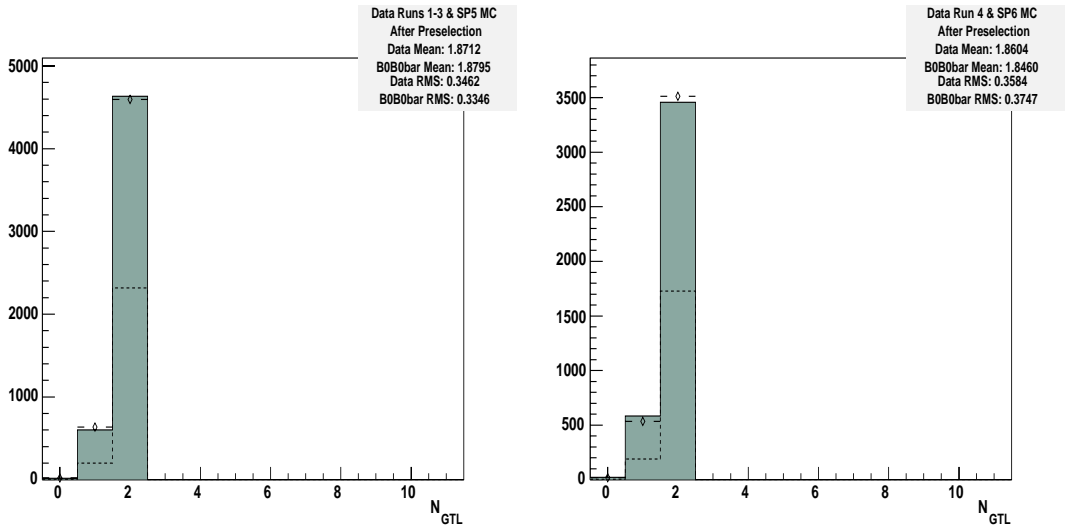


Figure A.18: The signal side `GoodTracksLoose` multiplicity after preselection for Runs 1-3 (left) and Run 4 (right). Only the *peaking components* of data (error bars) and generic neutral B (solid) and signal cocktail (dashed) have been plotted.

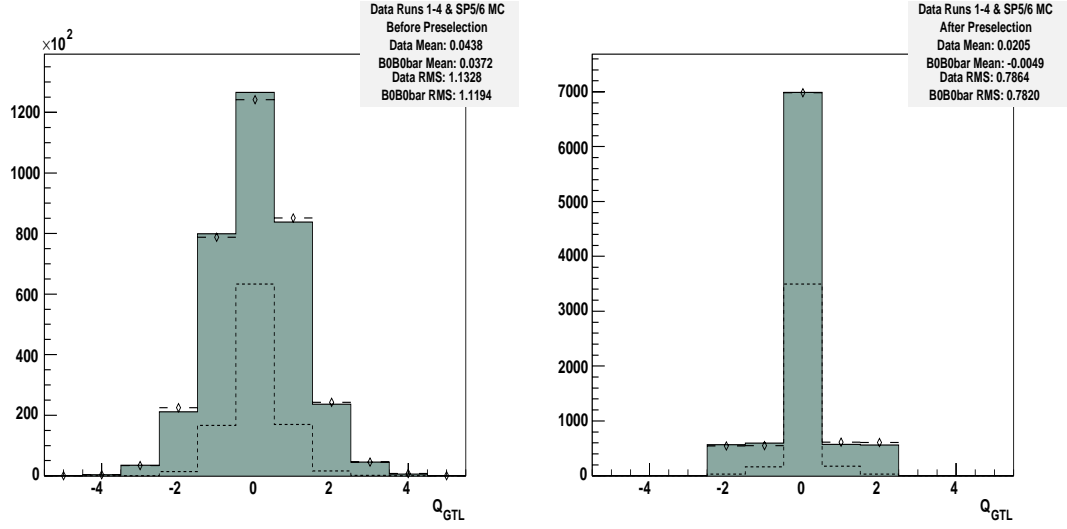


Figure A.19: The total signal side charge in GoodTracksLoose before (left) and after (right) preselection. Only the *peaking components* of data (error bars) and generic neutral B (solid) and signal cocktail (dashed) have been plotted.

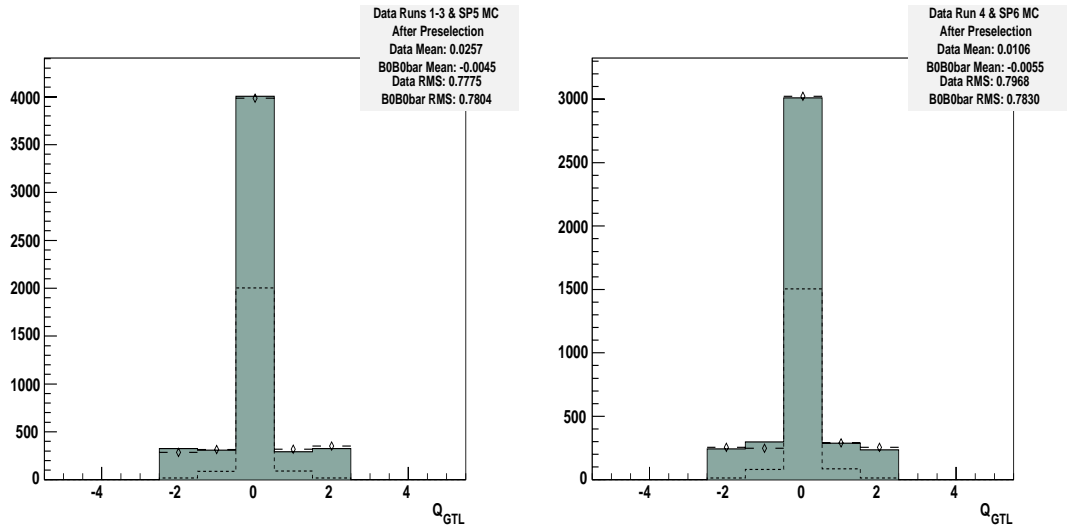


Figure A.20: The total signal side charge in GoodTracksLoose after preselection for Runs 1-3 (left) and Run 4 (right). Only the *peaking components* of data (error bars) and generic neutral B (solid) and signal cocktail (dashed) have been plotted.

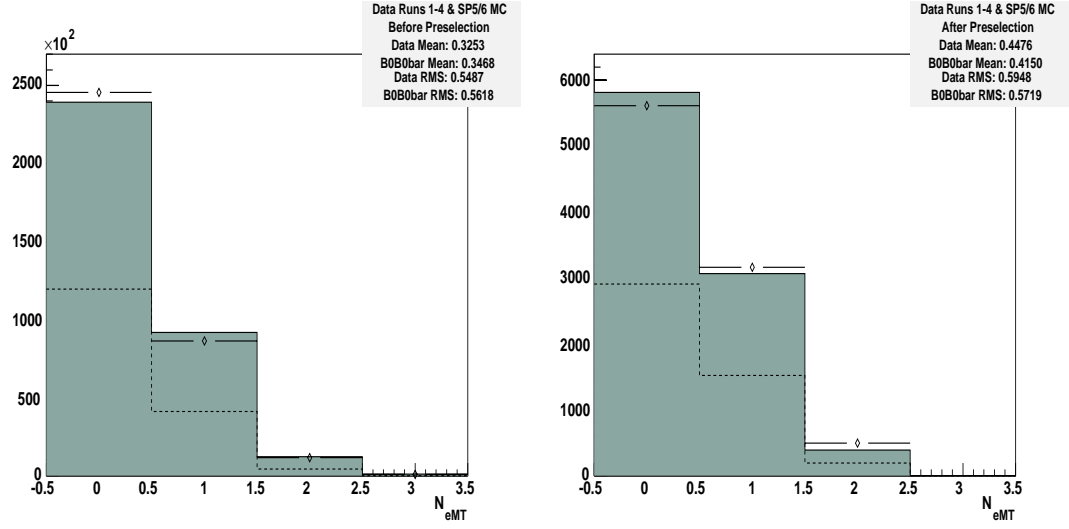


Figure A.21: The signal side $e\text{MicroTight}$ multiplicity before (left) and after (right) preselection. Only the *peaking components* of data (error bars) and generic neutral B (solid) and signal cocktail (dashed) have been plotted.

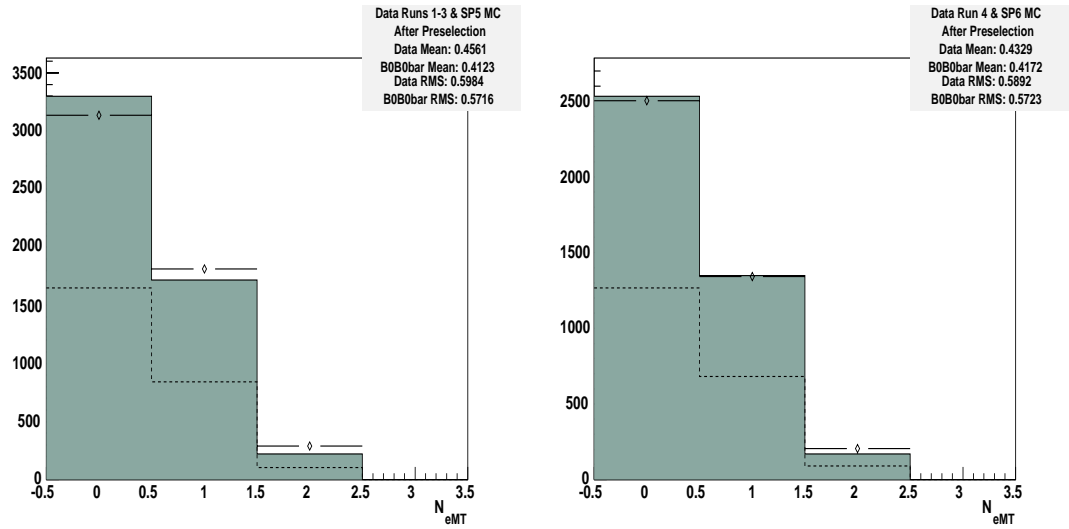


Figure A.22: The signal side $e\text{MicroTight}$ multiplicity after preselection for Runs 1-3 (left) and Run 4 (right). Only the *peaking components* of data (error bars) and generic neutral B (solid) and signal cocktail (dashed) have been plotted.

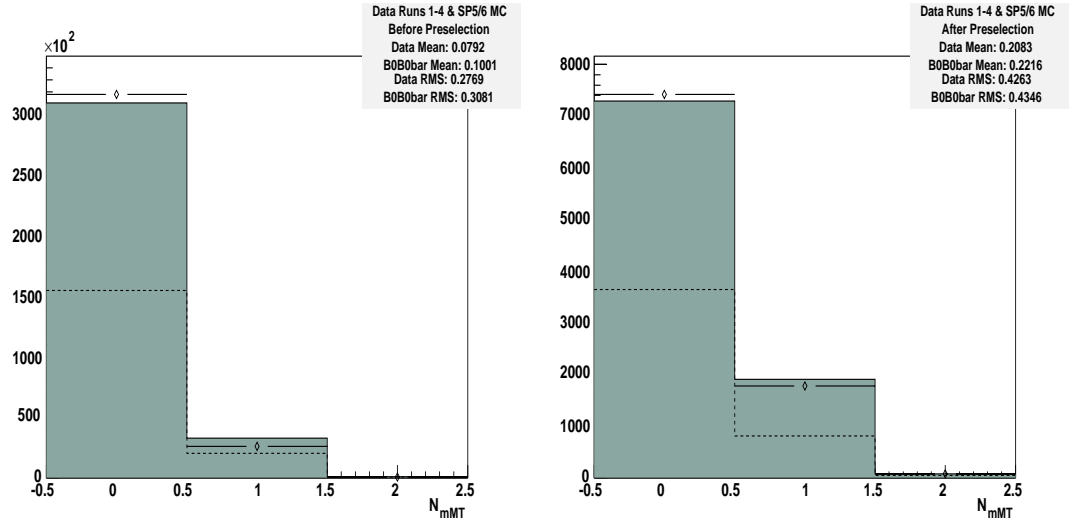


Figure A.23: The signal side $\mu\text{MicroTight}$ multiplicity before (left) and after (right) preselection. Only the *peaking components* of data (error bars) and generic neutral B (solid) and signal cocktail (dashed) have been plotted.

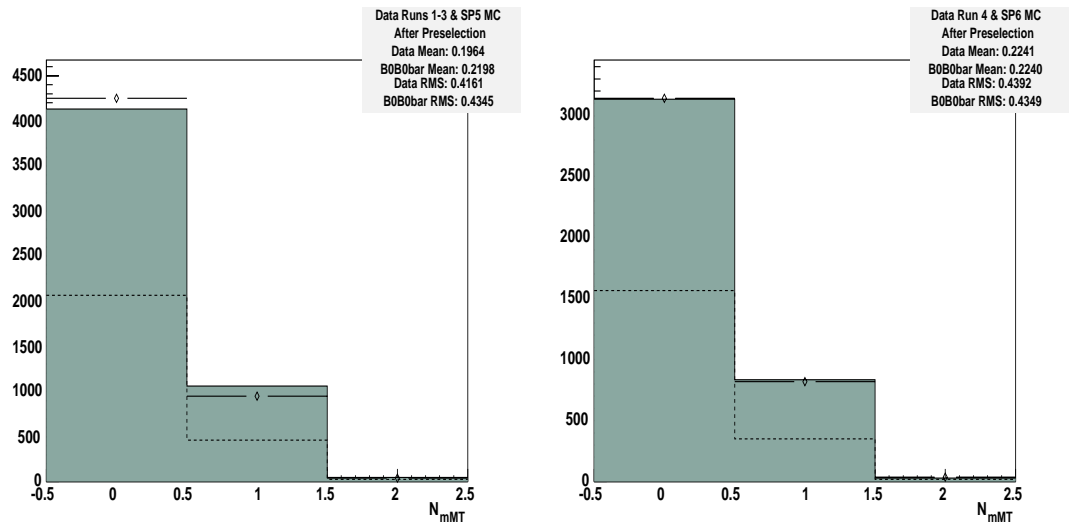


Figure A.24: The signal side $\mu\text{MicroTight}$ multiplicity after preselection for Runs 1-3 (left) and Run 4 (right). Only the *peaking components* of data (error bars) and generic neutral B (solid) and signal cocktail (dashed) have been plotted.

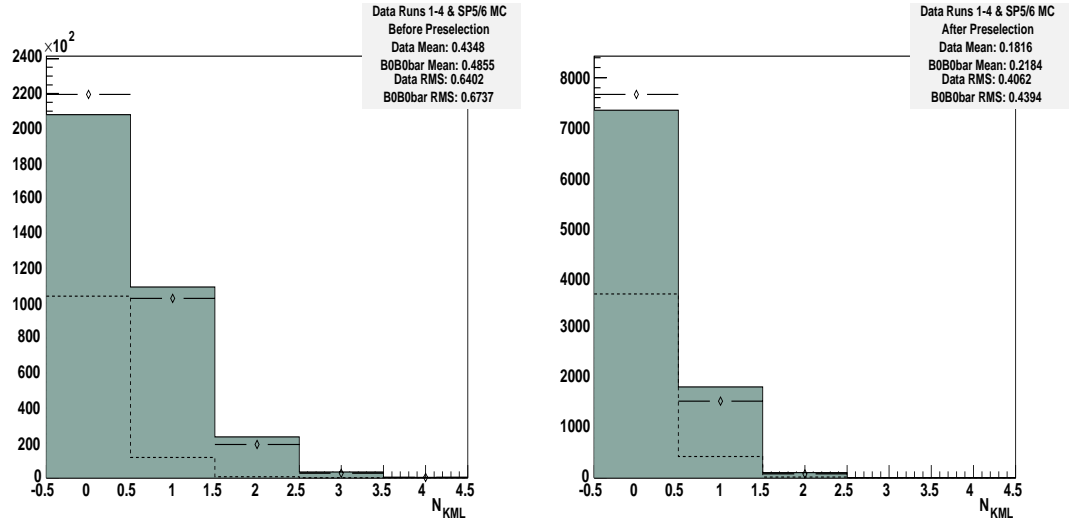


Figure A.25: The signal side $K_{\text{MicroLoose}}$ multiplicity before (left) and after (right) preselection. Only the *peaking components* of data (error bars) and generic neutral B (solid) and signal cocktail (dashed) have been plotted.

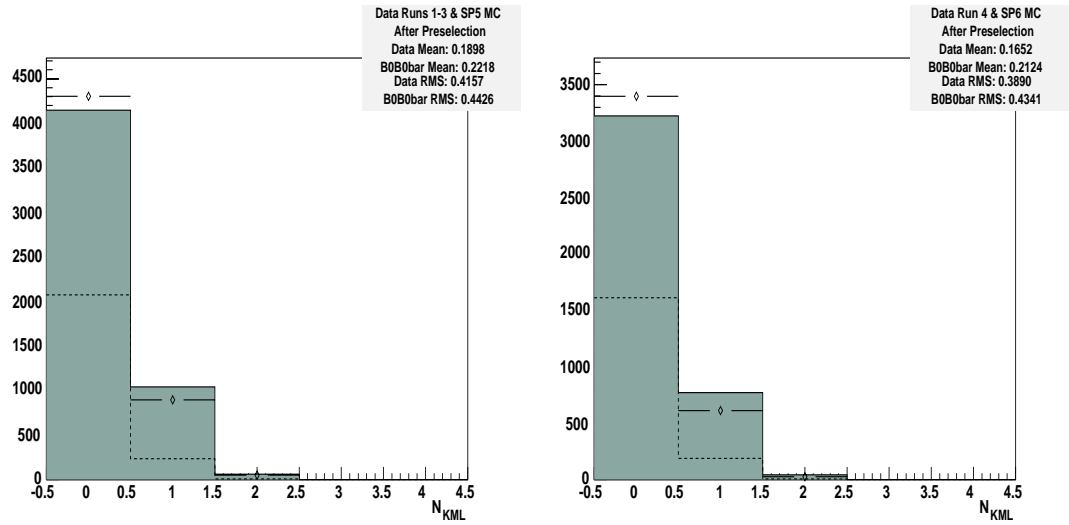
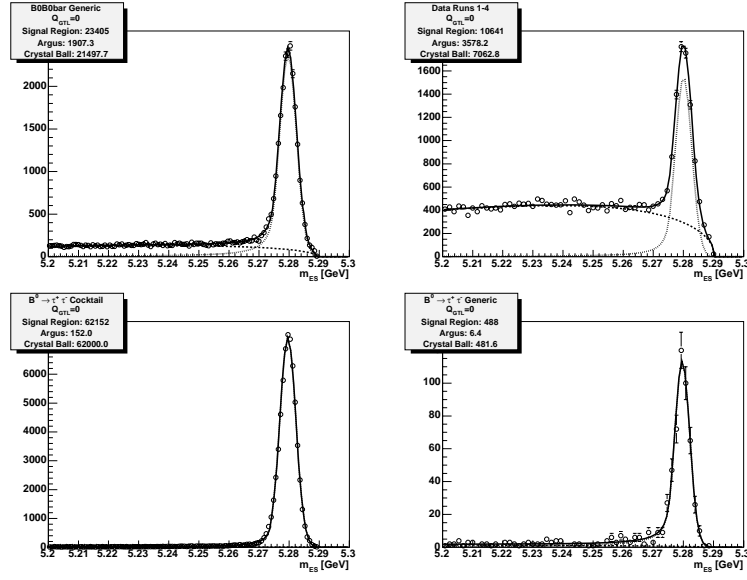
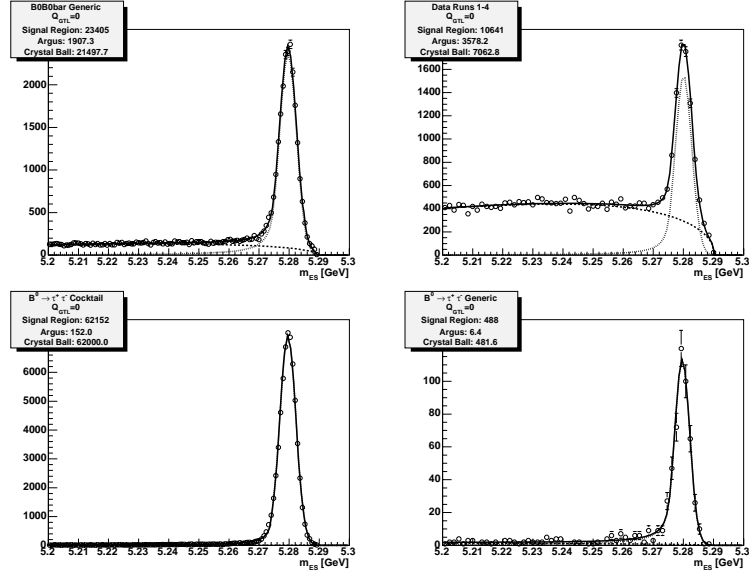
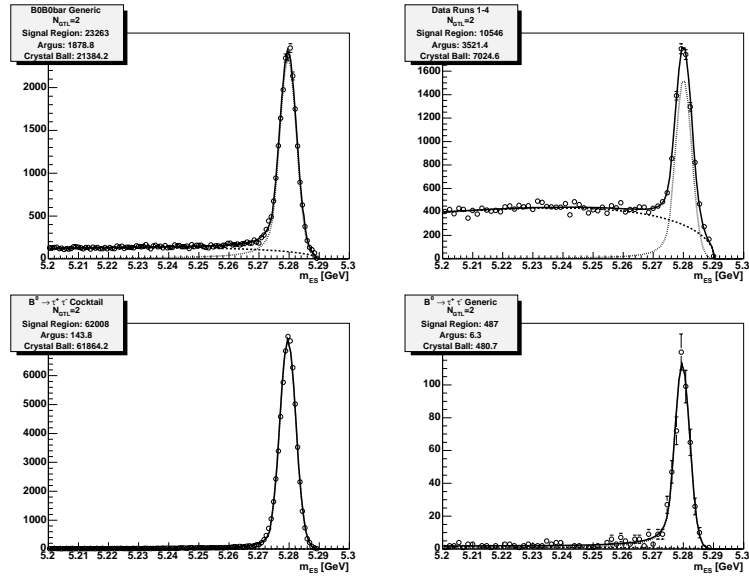
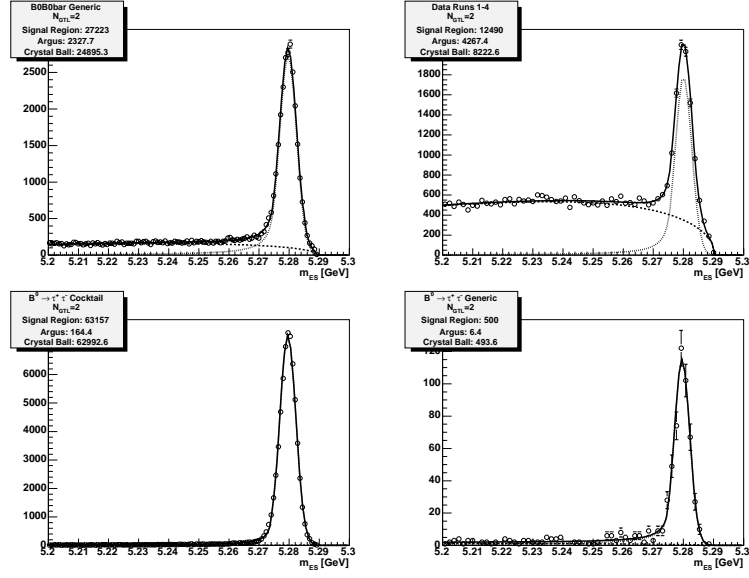
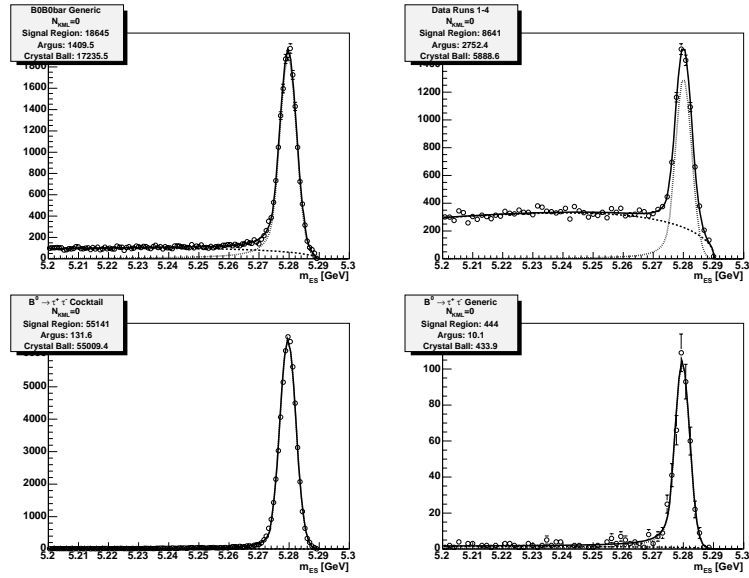


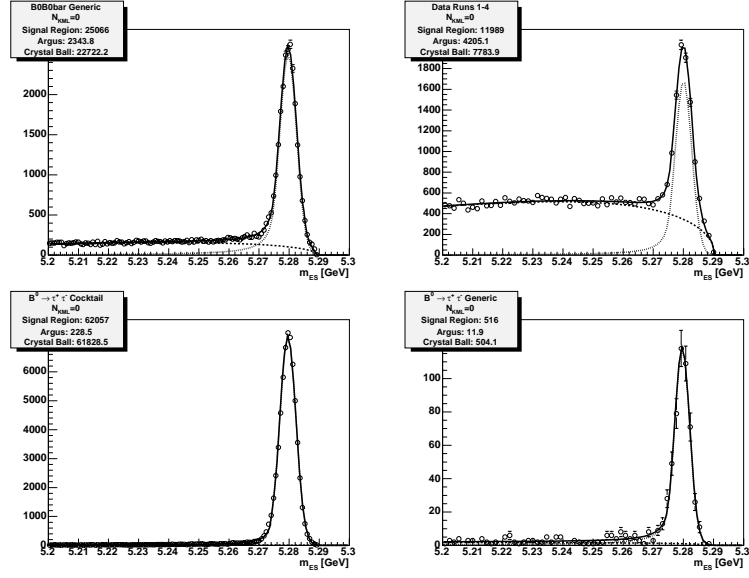
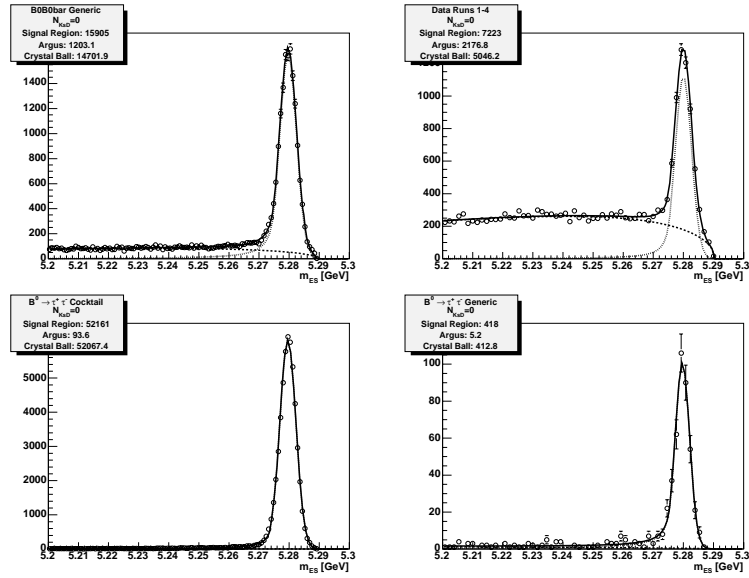
Figure A.26: The signal side $K_{\text{MicroLoose}}$ multiplicity after preselection for Runs 1-3 (left) and Run 4 (right). Only the *peaking components* of data (error bars) and generic neutral B (solid) and signal cocktail (dashed) have been plotted.

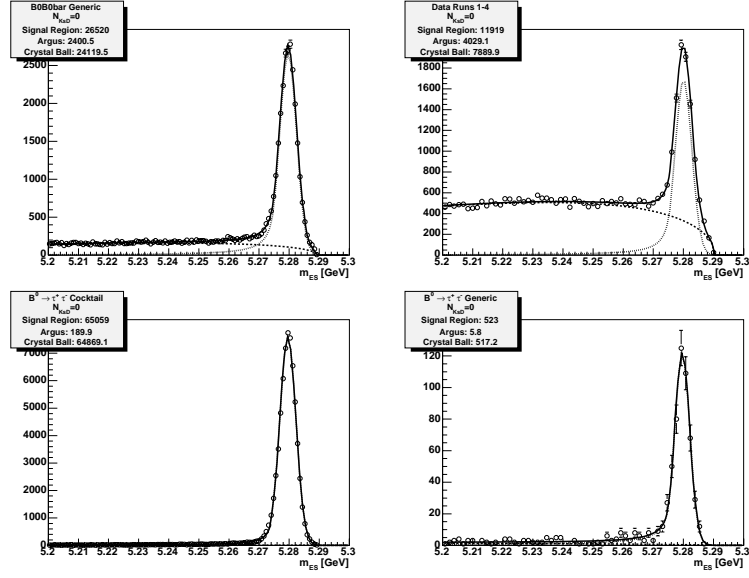
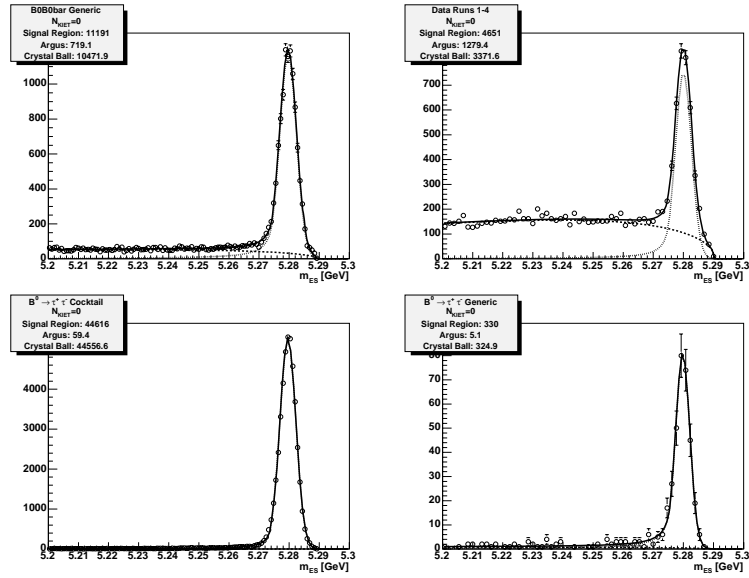
APPENDIX B

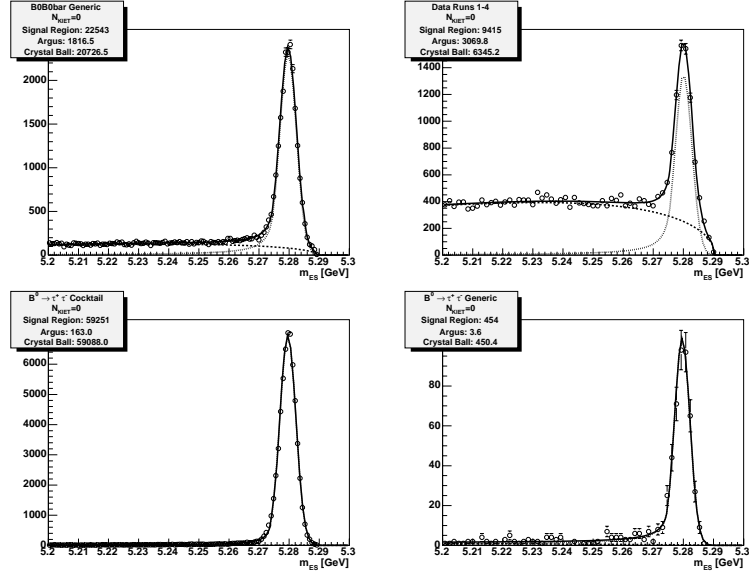
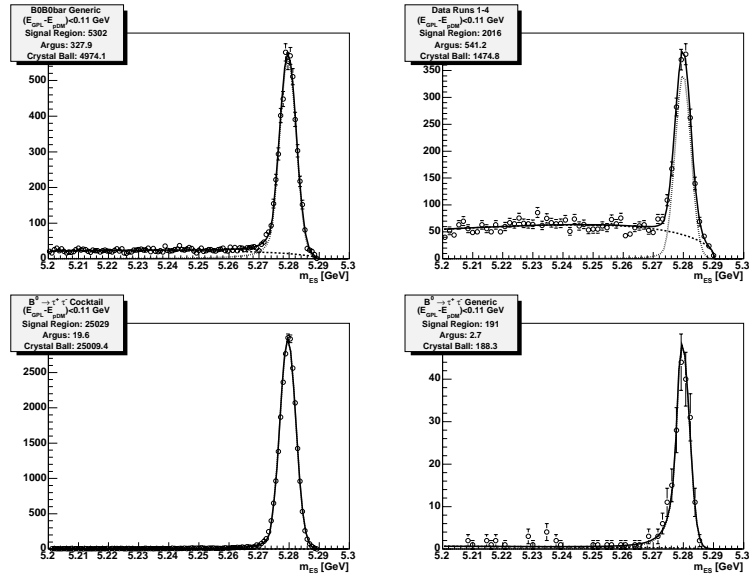
 m_{ES} FITS FOR EXTRACTING EFFICIENCIESFigure B.1: Cumulative $Q_{GTL} = 0$

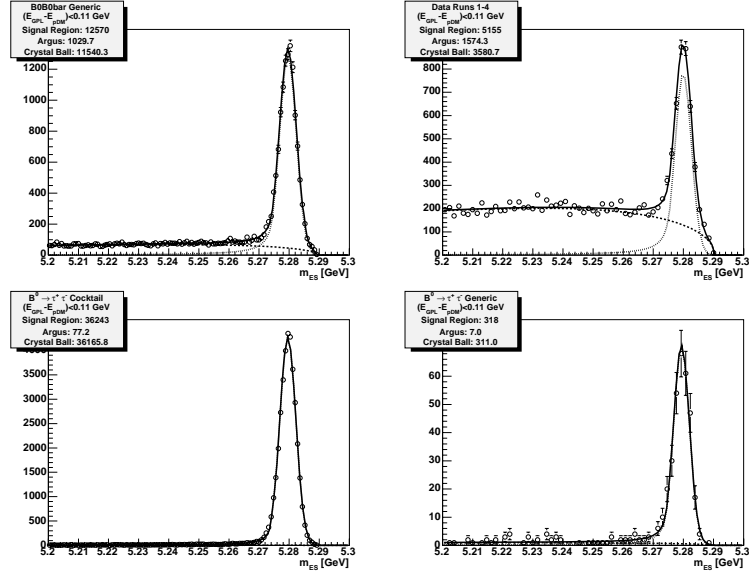
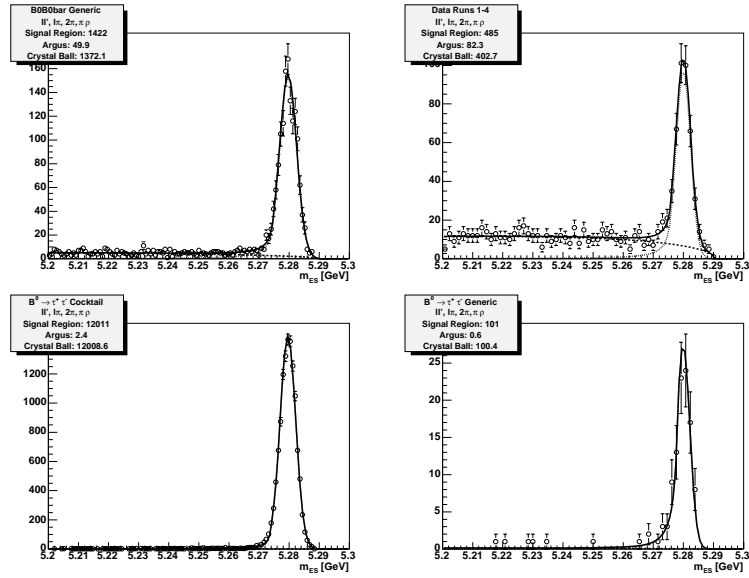
Figure B.2: Exclusive $Q_{GTL} = 0$ Figure B.3: Cumulative $N_{GTL} = 2$

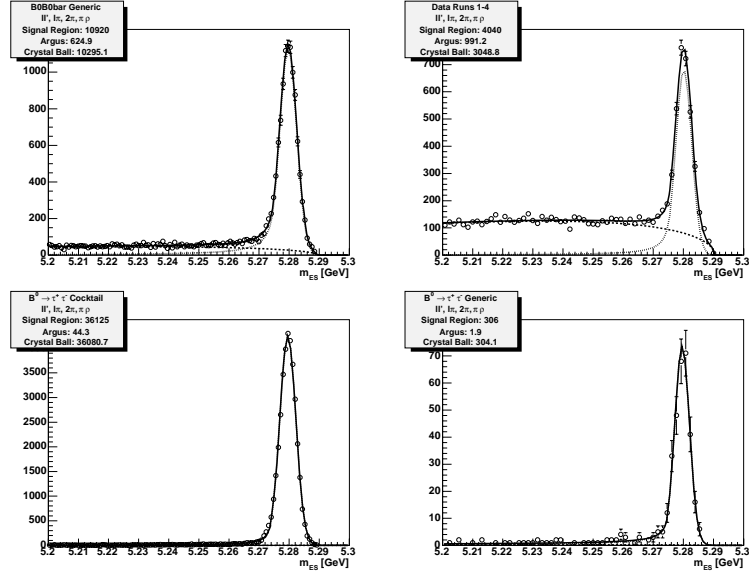
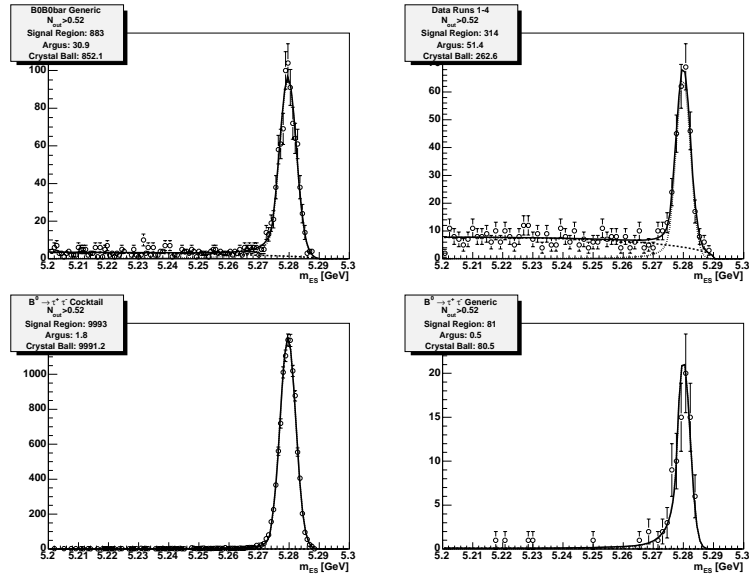
Figure B.4: Exclusive $N_{GTL} = 2$ Figure B.5: Cumulative $N_{KML} = 0$

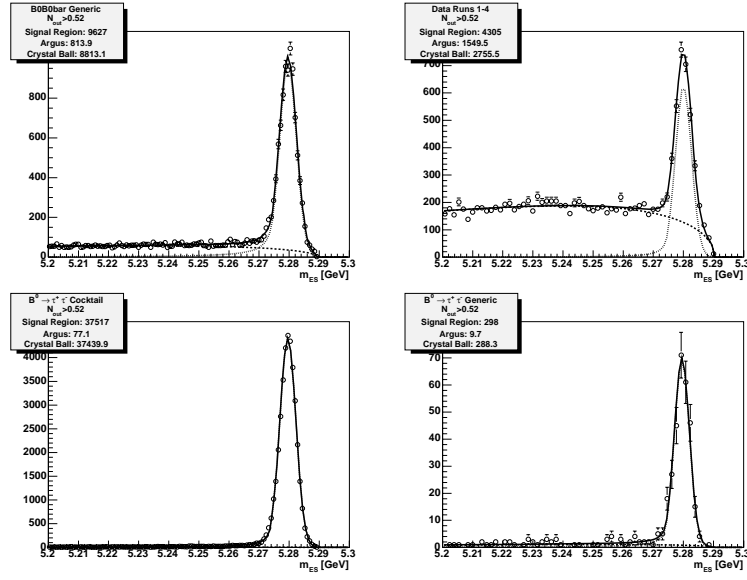
Figure B.6: Exclusive $N_{KML} = 0$ Figure B.7: Cumulative $N_{KsD} = 0$

Figure B.8: Exclusive $N_{KSD} = 0$ Figure B.9: Cumulative $N_{KLET} = 0$

Figure B.10: Exclusive $N_{KLET} = 0$ Figure B.11: Cumulative $E_{GPL} - E_{pDM} < 0.11$ GeV

Figure B.12: Exclusive $E_{GPL} - E_{pDM} < 0.11$ GeVFigure B.13: Cumulative mode subset M_{43}

Figure B.14: Exclusive mode subset M_{43} Figure B.15: Cumulative $NN > 0.52$

Figure B.16: Exclusive $NN > 0.52$

BIBLIOGRAPHY

- [1] The BaBar Collaboration. The BaBar detector. *Nucl. Instrum. Meth. A*, 479:1, 2002.
- [2] Particle Data Group. Review of particle physics. *Physical Review D*, 2002.
- [3] The BaBar Collaboration. The BaBar physics book. Technical Report SLAC-R-504, 1998.
- [4] CLEO Collaboration. Measurement of the form factors for $\bar{B}^0 \rightarrow D^{*+} l^- \bar{\nu}$. *Phys. Rev. Lett.*, 76:3898–3902, 1996.
- [5] B. Aubert et al. (The BaBar Collaboration). Search for decays of B^0 mesons into pairs of charged leptons: $B^0 \rightarrow e^+ e^-$, $B^0 \rightarrow \mu^+ \mu^-$, $B^0 \rightarrow e^+ \mu^-$. *hep-ex/0408096*.
- [6] B. Aubert et al. (The BaBar Collaboration). Search for B^0 decays to invisible final states and to $\nu \bar{\nu} \gamma$. *Phys. Rev. Lett.*, 93:091802, 2004.
- [7] J.J. Aubert et al. Experimental observation of a heavy particle J. *Phys. Rev. Lett.*, 33:1404, 1974.
- [8] J.E. Augustin et al. Discovery of a narrow resonance in $e^+ e^-$ annihilation. *Phys. Rev. Lett.*, 33:1406, 1974.
- [9] S.L. Glashow, L. Iliopolous, and L. Maiani. *Phys. Rev.*, D2:1285, 1970.
- [10] B. Aubert et al. (The BaBar Collaboration). Measurement of CP -violating asymmetries in B^0 decays to CP eigenstates. *Phys. Rev. Lett.*, 86:2515–2522, 2001.
- [11] Giuseppe Finocchiaro Riccardo De Sangro, Donatella Falciai and Yuehong Xie. Reconstruction of neutral hadrons. *BaBar Analysis Document 136*, 2001.
- [12] Yuval Grossman, Zoltan Ligeti, and Enrico Nardi. $B \rightarrow \tau^+ \tau^- (x)$ decays: First constraints and phenomenological implications. *Phys. Rev.*, D55:2768–2773, 1997.
- [13] W.N. Cottingham and D.A. Greenwood. *An Introduction to the Standard Model of Particle Physics*. Cambridge University Press, 1998.

- [14] Vernon D. Barger and Roger J.N. Phillips. *Collider Physics*. Addison Wesley Publishing Company Inc., 1996.
- [15] Particle Data Group. Electroweak model and constraints on new physics. *Physics Letters B*, 592, 2004.
- [16] Takeo Inami and C.S. Lim. Effects of superheavy quarks and leptons in low-energy weak processes $K_L \rightarrow \mu\bar{\mu}$, $K^+ \rightarrow \pi^+\nu\bar{\nu}$ and $K^0 \leftrightarrow \bar{K}^0$. *Prog. Theor. Phys.*, 65:297–314, 1981.
- [17] W. Skiba and J. Kalinowski. $B_s \rightarrow \tau^+\tau^-$ decay in a two-higgs-doublet model. *Nucl. Phys.*, B404:3–19, 1993.
- [18] G. Buchalla and A.J. Buras. QCD corrections to K - and B -decays. *Nucl. Phys.*, B400:225–239, 1993.
- [19] Heather E. Logan and Ulrich Nierste. $B_{s,d} \rightarrow l^+l^-$ in a two-higgs-doublet model. *Nucl. Phys.*, B586:39–55, 2000.
- [20] John F. Gunion, Howard E. Haber, Gordon Kane, and Sally Dawson. *The Higgs Hunter's Guide*. Perseus Books, 1990.
- [21] K.S. Babu and Christopher Kolda. Higgs-mediated $B^0 \rightarrow \mu^+\mu^-$ in minimal supersymmetry. *Phys. Rev. Lett.*, 84:241802, 2000.
- [22] Piotr H. Chankowski and Lucja Slawianowski. $B_{d,s}^0 \rightarrow \mu^+\mu^-$ in the MSSM. *Phys. Rev. D*, 63:054012, 2001.
- [23] Stephen P. Martin. A supersymmetry primer. In G.L. Kane, editor, *Perspectives on Supersymmetry*. World Scientific, 1998.
- [24] Gino Isidori and Alessandra Retico. Scalar flavour-changing neutral currents in the large- $\tan\beta$ limit. *JHEP*, 0111:001, 2001.
- [25] Particle Data Group. Supersymmetry. *Physics Letters B*, 592, 2004.
- [26] A. Dedes, H. Dreiner, and U. Nierste. Correlation of $B_s \rightarrow \mu^+\mu^-$ and $(g-2)_\mu$ in minimal supergravity. *Phys. Rev. Lett.*, 87:251804, 2001.
- [27] R. Arnowitt, B. Dutta, T. Kamon, and M. Tanaka. Detection of $B_s \rightarrow \mu\mu$ at the Tevatron Run II and constraints on the SUSY parameter space. *Phys. Lett. B*, 538:121, 2002.
- [28] Seungwon Baek, P. Ko, and Wan Young Song. Implications on SUSY breaking mediation mechanisms from observing $B_s \rightarrow \mu^+\mu^-$ and the muon $(g-2)$. *Phys. Rev. Lett.*, 89:271801, 2002.

- [29] J.K. Mizukoshi, Xerxes Tata, and Yili Wang. Higgs-mediated leptonic decays of B_s and B_d mesons as probes of supersymmetry. *Phys. Rev. D*, 66:115003, 2002.
- [30] Sacha Davidson, David Bailey, and Bruce A. Campbell. Model independent constraints on leptoquarks from rare processes. *Z. Phys.*, C61:613–643, 1994.
- [31] JoAnne L. Hewett and Thomas G. Rizzo. Much ado about leptoquarks: A comprehensive analysis. *Phys. Rev.*, D56:5709–5724, 1997.
- [32] Jogesh C. Pati and Abdus Salam. Lepton number as the fourth color. *Phys. Rev.*, D10:275–289, 1974.
- [33] M. Panofsky, W.K.H. Breidenbach. Accelerators and detectors. *Rev. Mod. Phys.*, 71:S121, 1999.
- [34] The BaBar Collaboration. Babar technical design report. Technical Report SLAC-R-95-457, SLAC, 1995.
- [35] J.T. Seeman et. al. Status and future plans of the PEP-II B-factory. Technical Report SLAC-PUB-9451, SLAC, 2002.
- [36] David Lange. The EvtGen particle decay simulation package. *Nucl. Instrum. Meth. A*, 462:152–155, 2001.
- [37] Torbjörn Sjöstrand, Patrik Edén, Christer Friberg, Leif Lönnblad, Gabriela Miu, Stephen Mrenna, and Emanuel Norrbin. High-energy-physics event generation with PYTHIA 6.1. *Comp. Phys. Commun.*, 135:238, 2001.
- [38] Z. Was and S. Jadach. Monte Carlo simulation of the process $e^+e^- \rightarrow \tau^+\tau^-$, $\tau^\pm \rightarrow x^\pm$ including radiative $O(\alpha^3)$ QED corrections, spin and mass effects. *Comp. Phys. Commun.*, 36:191, 1985.
- [39] Stdhep. <http://www-cpd.fnal.gov/psm/stdhep/>, 2004.
- [40] GEANT Collaboration. GEANT4-a simulation toolkit. *Nucl. Instrum. Meth. A*, 506:250–303, 2003.
- [41] Anders Ryd et al. EvtGen: A Monte Carlo generator for B -physics. *Babar Analysis Document 522*, 2003.
- [42] B. van Eijk E. Barberio and Z. Was. *Comput. Phys. Commun.*, 66:69, 1991.
- [43] E. Richter-Was. QED bremsstrahlung in semileptonic B and leptonic τ decays. *Phys. Lett. B*, 303:163–169, 1993.
- [44] Achim Stahl. *Physics with tau leptons*. Springer-Verlag, 2000.

- [45] P. Golonka, B. Kersevan, T. Pierzchala, E. Richter-Was, Z. Was, and M. Worek. The tauola-photos-f environment for the Tauola and Photos packages, Release II. *hep-ph/0312240v1*, 2003.
- [46] P.F. Harrison and H.R. Quinn. The BaBar physics book. Technical Report SLAC-R-504, SLAC, 1998.
- [47] Jeffrey D. Richman. *Heavy-Quark Physics and CP Violation*. Elsevier Science B.V., 1998.
- [48] Daryl Scora and Nathan Isgur. Semileptonic meson decays in the quark model: An update. *Phys. Rev. D*, 52:2783–2812, 1995.
- [49] J.L. Goity and W. Roberts. Soft pion emission in semileptonic B -meson decays. *Phys. Rev. D*, 51:3459–3477, 1995.
- [50] Matthias Neubert and Berthold Stech. Non-leptonic weak decays of B mesons. In *Heavy Flavours II*. World Scientific, 1998.
- [51] GEANT4 user’s guide: For application developers. <http://wwwasd.web.cern.ch/wwwasd/geant4/G4UsersDocuments/UsersGuides/Fo%rApplicationDeveloper/html/index.html>, 2004.
- [52] GEANT4 physics reference manual. <http://wwwasd.web.cern.ch/wwwasd/geant4/G4UsersDocuments/UsersGuides/PhysicsReferenceManual/html/PhysicsReferenceManual.html>, 2004.
- [53] D.H. Wright et. al. Using GEANT4 in the BaBar simulation. Technical Report SLAC-PUB-9862, SLAC, 2003.
- [54] Mirna van Hoek and Harpreet Singh. Drift chamber simulation. *Babar Analysis Document 169*, 2001.
- [55] N.R. Barlow, A.A. Borgland, D. Cote-Ahern, V. Halyo, and M. van Hoek. Improvement of the background mixing for all subsystems in the BaBar Monte Carlo simulation. *Babar Analysis Document 332*, 2002.
- [56] BaBar Particle Identification Analysis Working Group. <http://www.slac.stanford.edu/BFROOT/www/Physics/Tools/Pid/pid.html>, 2004.
- [57] BaBar Neutrals Reconstruction Analysis Working Group. <http://www.slac.stanford.edu/BFROOT/www/Physics/Analysis/AWG/Neutrals/>, 2004.

- [58] Tracking Efficiency Task Force. [http://www.slac.stanford.edu/BFROOT/www/Physics/TrackEffTaskForce/Tra%
ckingTaskForce-2004.html](http://www.slac.stanford.edu/BFROOT/www/Physics/TrackEffTaskForce/TrackingTaskForce-2004.html), 2004.
- [59] Electron Identification Analysis Working Group. Cut-based electron identification. *BaBar Analysis Document 90*, 2001.
- [60] Muon Identification Analysis Working Group. Muon identification in the BaBar experiment. *BaBar Analysis Document 60*, 2001.
- [61] Giampiero Mancinelli and Stefan Spanier. Kaon selection at the BaBar experiment. *BaBar Note 116*, 2001.
- [62] Neutral Identification and Reconstruction Analysis Working Group. Studies on π^0 reconstruction: Status report. *BaBar Analysis Document 20*, 2000.
- [63] Daniele DelRe, Sergio Grancagnolo, Riccardo Faccini, Alessio Sarti, and Guglielmo Denardo. Semi-exclusive B reconstruction. *BaBar Analysis Document 271*, 2001.
- [64] ROOT: An object-oriented data analysis framework. <http://root.cern.ch/>, 2004.
- [65] Minuit minimization package. [http://wwwasdoc.web.cern.ch/
wwwasdoc/WWW/minuit/minmain/minmain.html](http://wwwasdoc.web.cern.ch/wwwasdoc/WWW/minuit/minmain/minmain.html), 2004.
- [66] Simon Haykin. *Neural Networks: A Comprehensive Foundation*. MacMillan Publishing Company, 1994.
- [67] Stuttgart neural network simulator. [http://www-ra.informatik.
uni-tuebingen.de/SNNS/](http://www-ra.informatik.uni-tuebingen.de/SNNS/), 2004.
- [68] Riccardo Faccini Marcella Bona and Melanie Langer. Studies on $K_S \rightarrow \pi^+ \pi^-$ reconstruction. *BaBar Analysis Document 19*, 2000.
- [69] Robert D. Cousins and Virgil L. Highland. Incorporating systematic uncertainties into an upper limit. *Nucl. Instrum. Meth.*, A320:331–335, 1992.
- [70] Roger Barlow. A calculator for confidence intervals. *BaBar Analysis Document 340*, 2001.